NASA/TP-1998-206912

Static Thrust and Vectoring Performance of a Spherical Convergent Flap Nozzle With a Nonrectangular Divergent Duct

David J. Wing
Langley Research Center, Hampton, Virginia

February 1998

The NASA STI Program Office . . . in Profile

Since its founding, NASA has been dedicated to the advancement of aeronautics and space science. The NASA Scientific and Technical Information (STI) Program Office plays a key part in helping NASA maintain this important role.

The NASA STI Program Office is operated by Langley Research Center, the lead center for NASA's scientific and technical information. The NASA STI Program Office provides access to the NASA STI Database, the largest collection of aeronautical and space science STI in the world. The Program Office is also NASA's institutional mechanism for disseminating the results of its research and development activities. These results are published by NASA in the NASA STI Report Series, which includes the following report types:

- TECHNICAL PUBLICATION. Reports of completed research or a major significant phase of research that present the results of NASA programs and include extensive data or theoretical analysis. Includes compilations of significant scientific and technical data and information deemed to be of continuing reference value. NASA counter-part or peer-reviewed formal professional papers, but having less stringent limitations on manuscript length and extent of graphic presentations.

- TECHNICAL MEMORANDUM. Scientific and technical findings that are preliminary or of specialized interest, e.g., quick release reports, working papers, and bibliographies that contain minimal annotation. Does not contain extensive analysis.

- CONTRACTOR REPORT. Scientific and technical findings by NASA-sponsored contractors and grantees.

- CONFERENCE PUBLICATION. Collected papers from scientific and technical conferences, symposia, seminars, or other meetings sponsored or co-sponsored by NASA.

- SPECIAL PUBLICATION. Scientific, technical, or historical information from NASA programs, projects, and missions, often concerned with subjects having substantial public interest.

- TECHNICAL TRANSLATION. English-language translations of foreign scientific and technical material pertinent to NASA's mission.

Specialized services that help round out the STI Program Office's diverse offerings include creating custom thesauri, building customized databases, organizing and publishing research results . . . even providing videos.

For more information about the NASA STI Program Office, see the following:

- Access the NASA STI Program Home Page at ***http://www.sti.nasa.gov***

- Email your question via the Internet to help@sti.nasa.gov

- Fax your question to the NASA Access Help Desk at (301) 621-0134

- Phone the NASA Access Help Desk at (301) 621-0390

- Write to:
  NASA Access Help Desk
  NASA Center for AeroSpace Information
  800 Elkridge Landing Road
  Linthicum Heights, MD 21090-2934

NASA/TP-1998-206912

Static Thrust and Vectoring Performance of a Spherical Convergent Flap Nozzle With a Nonrectangular Divergent Duct

David J. Wing
Langley Research Center, Hampton, Virginia

National Aeronautics and
Space Administration

Langley Research Center
Hampton, Virginia 23681-2199

February 1998

Acknowledgments

The research presented in this report is the result of the cooperative effort of Pratt & Whitney, Government Engines & Space Propulsion, United Technologies Corporation and the Langley Research Center. The design and development of the nozzle concept and test hardware were provided by Pratt & Whitney. The test was conducted by the staff of the former Propulsion Aerodynamics Branch at the Langley Research Center.

Available from the following:

NASA Center for AeroSpace Information (CASI)
800 Elkridge Landing Road
Linthicum Heights, MD 21090-2934
(301) 621-0390

National Technical Information Service (NTIS)
5285 Port Royal Road
Springfield, VA 22161-2171
(703) 487-4650

Abstract

The static internal performance of a multiaxis-thrust-vectoring, spherical convergent flap (SCF) nozzle with a nonrectangular divergent duct was obtained in the model preparation area of the Langley 16-Foot Transonic Tunnel. Duct cross sections of hexagonal and bowtie shapes were tested. Additional geometric parameters included throat area (power setting), pitch flap deflection angle, and yaw gimbal angle. Nozzle pressure ratio was varied from 2 to 12 for dry power configurations and from 2 to 6 for afterburning power configurations. Approximately a 1-percent loss in thrust efficiency from SCF nozzles with a rectangular divergent duct was incurred as a result of internal oblique shocks in the flow field. The internal oblique shocks were the result of cross flow generated by the vee-shaped geometric throat. The hexagonal and bowtie nozzles had mirror-imaged flow fields and therefore similar thrust performance. Thrust vectoring was not hampered by the three-dimensional internal geometry of the nozzles. Flow visualization indicates pitch thrust-vector angles larger than 10° may be achievable with minimal adverse effect on or a possible gain in resultant thrust efficiency as compared with the performance at a pitch thrust-vector angle of 10°.

Introduction

An extensive effort has been underway to develop a database of convergent-divergent nozzle designs for advanced aircraft engines. The joint effort by industry and the Langley Research Center has generally been oriented toward providing multifunctional capabilities to advanced nozzle designs such as variable throat and exit areas, single or multiaxis thrust vectoring, and thrust reversing (refs. 1 and 2). Simultaneously, an attempt has been made to minimize the adverse impact on the overall aircraft by maintaining high cruise thrust efficiency, minimizing nozzle system weight, and providing suitable airframe integration characteristics by careful blending with the aerodynamic external lines while conforming to observability design guidelines.

The spherical convergent flap (SCF) nozzle design has been identified as having several desirable characteristics (ref. 3). The convergent section of an SCF nozzle, as its name suggests, is spherical and therefore provides structural efficiency for the containment of the high-pressure exhaust flow and allows for a lightweight nozzle design because no cross-section transition duct is required. An additional benefit of this shape is that a gimbal mechanism can be easily incorporated to provide a yaw thrust-vectoring capability to the nozzle. The divergent section is typically nonaxisymmetric to take advantage of the efficient pitch thrust-vectoring technique of deflecting the divergent flaps about hinges at the throat. The throat (the station of minimum duct cross-sectional area) is approximately located where the nonaxisymmetric divergent duct intersects the spherical convergent duct.

Several investigations have studied the isolated and installed performance of the SCF design (refs. 3, 4, and 5). In each case, a rectangular divergent duct was incorporated, and the thrust efficiency was generally found to be high. Gimbaled yaw thrust vectoring provided thrust-vector angles equal to the gimbal angle with minimal losses, and divergent flap pitch thrust vectoring was found to be efficient as well.

The current investigation focuses on two different options in divergent duct cross-sectional design. Specifically, hexagonal and bowtie divergent duct cross sections with scarfed trailing edges were investigated at static conditions in the model preparation area of the Langley 16-Foot Transonic Tunnel. Such geometric features can provide a reduced level of observability to the nozzle while improving the blending of the nozzle with the external aerodynamic lines. The nozzles were tested in dry power and afterburning power modes with a range of flap deflection angles for pitch thrust vectoring and gimbal angles for yaw thrust vectoring. Internal static pressure distributions and three components of force were measured. A surface flow visualization technique was used to aid in analyzing the flow field.

Symbols

A_e	nozzle exit area, in^2
A_t	nozzle throat area, in^2
d_t	equivalent throat diameter, $\sqrt{\frac{4A_t}{\pi}}$, in.
F_A	measured axial thrust component, lb
F_i	ideal isentropic thrust, $w_p\sqrt{\frac{R_j T_{t,j}}{g^2}\frac{2\gamma}{\gamma-1}\left[1-\left(\frac{p_a}{p_{t,j}}\right)^{(\gamma-1)/\gamma}\right]}$, lb
F_N	measured normal thrust component, lb
F_r	resultant gross thrust, $\sqrt{F_A^2+F_N^2+F_S^2}$, lb

F_S	measured side thrust component, lb
g	gravitational acceleration, 32.174 ft/sec^2
L	nozzle length (along nozzle axis) from spherical center to sidewall trailing-edge point, 6.046 in. (see figs. 4(a)–(c))
NPR	nozzle pressure ratio, $\frac{p_{t,j}}{p_a}$
p	internal local static pressure, psi
p_a	atmospheric pressure, psi
$p_{t,j}$	average jet total pressure, psi
R_j	gas constant for air (γ = 1.3997), 1716 ft^2/sec^2-°R
$T_{t,j}$	average jet total temperature, °R
w	width of flap, 2.700 in. (see figs. 4(a)–(c))
w_p	measured air (exhaust) weight-flow rate, lb/sec
x	distance downstream from center of spherical convergent flap, in. (see fig. 5)
y	lateral distance from flap centerline, in. (see figs. 5(a) and (b))
z	vertical distance from sidewall centerline, in. (see fig. 5(c))
γ	ratio of specific heats, 1.3997 for air
δ_p	resultant pitch thrust-vector angle, $\tan^{-1}\frac{F_N}{F_A}$, deg
$\delta_{v,p}$	pitch flap deflection angle, positive deflection downward, deg
$\delta_{v,y}$	divergent section yaw gimbal angle, positive gimbal angle to left, deg
δ_y	resultant yaw thrust-vector angle, $\tan^{-1}\frac{F_S}{F_A}$, deg
ε	expansion ratio, A_e/A_t

Abbreviations:

SCF	spherical convergent flap
Sta.	model station, in.

Apparatus and Procedures

Test Facility

The test was conducted in the model preparation area of the Langley 16-Foot Transonic Tunnel, a facility normally used for model setup and calibration before installation into the wind tunnel. The model preparation area has a high-pressure air supply and a data acquisition system and is therefore occasionally used to test the internal performance of nozzles at wind-off conditions. The air system uses the same supply of clean, dry air used in the wind tunnel propulsion simulations and the same valves, filters, and heat exchanger to provide air at a constant total temperature of about 530°R. The model was mounted on a sting-strut support system in a soundproof room with an air exhaust collector duct downstream of the jet. The control room is adjacent to the test area, and a window between the rooms allows for model observation during testing. Reference 6 provides further details of the facility.

Single-Engine Propulsion Simulation System

A sketch of the air-powered, single-engine propulsion simulation system on which the nozzle configurations were tested statically is presented in figure 1. The propulsion simulation system is shown with a typical nozzle configuration installed. As shown in figure 1, air is supplied through six lines in the support strut to an annular nonmetric (not supported by the force balance) high-pressure plenum. The air flows radially out the high-pressure plenum through eight equally spaced sonic nozzles into a metric low-pressure plenum. This nonmetric-to-metric flow transfer design (perpendicular to the nozzle axis) minimizes the tare force on the balance caused by axial momentum transfer of the flow across the force balance. Flexible bellows act as seals between the metric and nonmetric portions of the model and minimize forces caused by pressurization. The air then passes through a choke plate for flow straightening, through an instrumentation section, and into the nozzle; the air then exhausts to atmospheric pressure.

Nozzle Design

The nozzle tested in this investigation was a spherical convergent flap (SCF) nozzle. This type of nozzle has a circular entrance station, a spherical convergent duct, and a noncircular divergent duct. The current investigation studied hexagonal and bowtie cross-sectional shapes of the divergent duct. Photographs of some of the model hardware are shown in figures 2 and 3.

The geometry of the nozzles tested is presented in figure 4. In figures 4(a) and (b), four different geometric regions along the internal flow path are identified: a spherical convergent duct, a divergent plateau, a single convergent triangular ramp (bowtie) or a pair of convergent triangular ramps (hexagonal), and a divergent flap. Comparison of the photographs in figures 2(a) and (c) aids in the understanding of the geometric differences between the hexagonal and bowtie configurations. The plateau and triangular ramps were a consequence of incorporating pitch deflection into the divergent flap design. In order to deflect the divergent flaps for pitch vectoring of an operational nozzle (one with moving parts), a linear hinge is required across the width of the

duct. Therefore, a short, rectangular duct was intersected with the spherical convergent duct to provide a flat surface for the hinge; the upper and lower surfaces of this rectangular duct form the plateau regions. The linear hinge would be located at the juncture between the plateau and the triangular ramps, which form the transition from the rectangular duct to the hexagonal or bowtie duct. (See fig. 4(d).) It is evident that a complex internal geometry was required to satisfy the operational requirements of the nozzle. For the test, interchangeable fixed hardware was used to simulate all deflections and gimballing of hardware.

The minimum duct area, or geometric throat, occurs along the ridge formed between the triangular ramps and the divergent flap. These surfaces remain fixed with respect to each other during pitch-flap deflections and during transition to afterburning power. The transition to afterburning power would occur (in an operational nozzle) with an iris-type movement where the plateau regions move apart from each other about the spherical duct. The projected throat areas of the unvectored dry and afterburning power configurations as tested were 3.0 and 7.0 in^2, respectively. The divergent flaps of the unvectored dry and afterburning power configurations had divergence angles of 3.2° and 7.4°, respectively, which resulted in an average expansion ratio (based on the dimensions half-way between the centerline and the sidewall) of 1.30 for both configurations.

Yaw thrust vectoring would be achieved by gimballing the divergent duct in the horizontal plane about the spherical duct. Again, the gimballing mechanism was simulated by interchangeable fixed hardware as shown in figure 4(e).

Test Conditions

The test matrix of the hexagonal configurations consisted of two pitch flap deflection angles ($\delta_{v,p}$ = 0° and 10°), three yaw gimbal angles ($\delta_{v,y}$ = 0°, 10°, and 20°), and two throat areas (representing dry and afterburning power settings) for a total of 12 hexagonal configurations. The test matrix of the bowtie configurations consisted of one pitch flap deflection angle ($\delta_{v,p}$ = 0°), three yaw gimbal angles ($\delta_{v,y}$ = 0°, 10°, and 20°), and one throat area (dry power). The complete configuration matrix is presented in table 1. Nozzle pressure ratio (NPR) was varied from 2 to 12 for dry power configurations and from 2 to 6 for afterburning power configurations. Jet total temperature was maintained at approximately 530°R.

Instrumentation

A six-component strain-gauge balance was used to measure forces and moments on the model; the moment data are not included in this report but were used for balance-interactions corrections. Jet total pressure was calculated by averaging total pressure measurements from nine individual pitot probes located at a fixed station in the instrumentation section. (See fig. 1.) A thermocouple was also positioned in the instrumentation section to measure jet total temperature. The weight-flow rate w_p of the high-pressure air supplied to the nozzle was measured by a multiple critical venturi located in the air system upstream of the model.

The distribution of internal surface static pressure was obtained for each test configuration. One quadrant of the nozzle was instrumented with three primary rows of pressure orifices oriented longitudinally. A limited number of additional pressure orifices were located between the three primary rows in the general location of the geometric throat. For the pitch thrust-vectoring configurations, the lower (suction) surface was instrumented. Additionally, one sidewall was instrumented with three longitudinal rows of orifices positioned symmetrically about the centerline. Static pressure orifice locations are shown in figure 5. The x/L location of each pressure measurement on the flap is given in table 2 for five constant span rows $\left(y/(w/2) = 0.074, 0.296, 0.481, 0.704, \text{ and } 0.926\right)$ where $y/(w/2)$ is the span location normalized by the nozzle half width. Similar x/L locations for the sidewall pressure measurements are listed for three constant waterline rows $\left(z/(w/2) = -0.296, 0.000, \text{ and } 0.296\right)$.

Data Reduction

Every data point used in the computations was the average of 50 samples of data recorded at a rate of 10 samples/sec. With the exception of resultant gross thrust F_r, all thrust data in this report are referenced to the model centerline. Four basic performance parameters are used in the presentation of results: resultant thrust ratio F_r/F_i, axial thrust ratio F_A/F_i, resultant pitch thrust-vector angle δ_p, and resultant yaw thrust-vector angle δ_y. Reference 7 presents a detailed description of the data reduction procedures used for the current investigation.

The resultant thrust ratio F_r/F_i is the resultant gross thrust divided by the ideal thrust F_i. Ideal thrust is based on measured weight-flow rate w_p, jet total pressure $p_{t,j}$, and jet total temperature $T_{t,j}$ and assumes fully expanded isentropic flow. The resultant thrust ratio is used as a measure of nozzle thrust efficiency. The axial thrust ratio F_A/F_i is the ratio of the measured nozzle thrust along the model centerline to the ideal nozzle thrust. As can be seen from the definitions of F_A and F_r, the thrust F_A along the model centerline reflects the geometric loss that results from turning the thrust vector away from the axial direction; the resultant gross thrust F_r does not. The angles δ_p and δ_y are the calculated angles in the pitch and

yaw thrust-vector planes at which the resultant gross thrust is deflected from the nozzle axis. These angles increase with either an increase in normal or side force or a decrease in axial force.

Corrections were applied to all balance measurements before they entered in the calculation of performance parameters. Each balance component was initially corrected for model weight tares and isolated balance interactions. Because the bellows (fig. 1) create a restraint on the installed balance, the balance was recalibrated after installation in the model and corrections resulting from additional component interactions were computed. Besides providing a set of assembly interaction corrections, the recalibration also accounts for the effects of pressurization (nozzle pressure ratio) and momentum (weight flow). The bellows in the air pressurization system were designed to eliminate pressure and momentum interactions with the balance. However, residual tares still exist and result from a small pressure differential between the ends of the bellows when air system internal velocities are high and from small differences in the spring constants of the forward and aft bellows when pressurized. The residual tares were determined by testing a set of reference calibration nozzles with known performance over a range of expected internal pressures, weight-flow rates, and external forces and moments. The procedures for determining and computing the tares are discussed in references 6 and 7.

Uncertainty Analysis

An uncertainty analysis of the results presented was performed based on a propagation of bias uncertainties of actual measurements through the data reduction equations. The analysis assumes bias errors are dominant over precision errors and is based on the method presented in reference 8. This method uses the first-order terms in a Taylor series expansion of the data reduction equations to estimate the uncertainty contributions of each measurement. With this technique, the contribution of each measurement would be the measurement uncertainty multiplied by the derivative of the data reduction equation with respect to that measurement. The total uncertainty of the final calculated result is estimated as the root-sum-square of the individual contributions with 95 percent confidence.

The analysis accounted for the uncertainties of the following measurements: jet total pressure, jet total temperature, atmospheric pressure, venturi weight-flow rate, and three components of force. The analysis also accounted for the benefit of averaging the total pressure measurements of nine separate transducers, each connected to a separate probe on the total pressure rake.

The results of the analysis for the range of conditions tested indicate that the uncertainties in F_r/F_i, F_A/F_i, δ_p, and δ_y are essentially independent of nozzle pressure ratio. The uncertainties of the thrust ratios F_r/F_i and F_A/F_i are approximately ±0.006. The uncertainty of δ_p is approximately ±1.2 percent of measured value, and the uncertainty of δ_y is approximately ±1.1 percent of measured value.

Flow Visualization

Surface flow visualization was performed for various configurations at a limited number of test conditions by using a paint flow technique. In this technique, an oil-based paint with fluorescent dye is applied to the model surfaces in a pattern of dots. Operating the jet at a specified condition causes dye streaks to form and dry on the model, which indicate some flow features and directions. The model is then disassembled and photographed under ultraviolet light to show maximum detail.

Presentation of Results

The discussion of results are presented in two parts: first, an analysis of the force data and, second, an analysis of the flow field based on the pressure distribution and flow visualization data. The thrust and vectoring performance of each configuration are presented in figures 6 through 8 and tabulated in tables 3 through 17. Thrust ratios for the hexagonal nozzle and published data on other SCF-type nozzles are presented in figure 9. Typical internal pressure distributions of each configuration and flow visualization photographs of the configurations with no yaw thrust vectoring are presented in figures 10 through 19. A complete tabulation of pressure distributions is presented in tables 18 through 32.

Discussion of Results

Thrust Performance

The thrust performance data of the bowtie configurations are presented in figure 6. Figures 7 and 8, respectively, contain the performance data of the hexagonal configurations in dry power and afterburning power modes of operation. The performance of all configurations was similar in behavior and can therefore be discussed as a group. The resultant thrust performance curve, F_r/F_i as a function of NPR, is classical for a convergent-divergent nozzle despite the complex internal geometry. Large losses caused by flow overexpansion occurred at low values of NPR, and smaller losses caused by flow underexpansion occurred at higher values of NPR. Peak resultant thrust ratio, corresponding to the condition of fully expanded flow, occurred approximately at NPR = 5.5 to 6.0 for the configurations with no

pitch thrust vectoring ($\delta_{v,p}$ = 0°) and approximately at NPR = 3.5 to 4.0 for the pitch thrust-vectoring configurations ($\delta_{v,p}$ = 10°). The average geometric expansion ratio (nozzle exit area divided by throat area, calculated at $y/(w/2)$ = 0.5) for the unvectored nozzles in this investigation was 1.30, corresponding to a design pressure ratio (theoretical condition for peak thrust ratio) of 4.64. The fact that the measured NPR for peak thrust ratio was greater than the design value indicates (1) a higher effective expansion ratio, which could be caused by either a reduced aerodynamic throat area from excessive flow separation, (2) an increased effective exit area as a result of the ventilated corners at the exit plane, or (3) possibly a combination of the two conditions.

Resultant thrust ratios of the unvectored, dry power, hexagonal configuration and other SCF-type nozzles from two other references are presented in figure 9. References 4 and 5 contain thrust efficiency data of SCF-type nozzles with rectangular divergent-duct cross sections rather than the hexagonal or bowtie cross sections of the current investigation. The SCF nozzles of the current study attained a maximum static thrust efficiency of nearly 0.98. As shown in figure 9, the nozzles from reference 5 produced peak thrust ratios approximately 1 percent below those of the current study, and the nozzle from reference 4 was about 1 percent more efficient. The lower performance of the reference 5 nozzles may be the result of sharp corners at the throat station where the spherical and rectangular ducts joined. The nozzle in reference 4 had rounded corners at this location, possibly contributing to the more efficient thrust performance. The current nozzles had relatively sharp corners but also a more complex transition from the convergent duct to the divergent duct. Comparison of the data indicates, however, that the performance of the current SCF nozzle, despite its complex three-dimensional internal geometry, is similar to performance levels of SCF nozzles with rectangular geometry. Analysis of the flow field later sheds light on how the internal geometry of the current nozzles affects the internal thrust performance.

Vectoring Performance

The thrust-vectoring performance of the nozzles in the current investigation is also presented in figures 6 through 8. As shown in figures 6, 7(a), and 8(a) for $\delta_{v,p}$ = 0°, gimballing the nozzle in the yaw direction to produce pure yaw thrust vectoring resulted in a thrust-vector angle essentially equal to the gimbal angle across the NPR range with no loss in resultant thrust. This behavior is typical for gimballed nozzles (ref. 3). The spherical convergent duct acts as a plenum, and because the Mach number of the flow is low, the flow can efficiently exit in any direction from this plenum. The apparent increase in resultant thrust ratio at $\delta_{v,p}$ = 20° is questionable because there is no physical explanation for an increase in thrust from turning the flow. Considering the estimated bias uncertainty of the resultant thrust ratio of ±0.006 (see section "Uncertainty Analysis"), the differences noted are not numerically significant.

The vectoring performance at $\delta_{v,p}$ = 10° for the hexagonal configurations is shown in figures 7(b) and 8(b). The pitch thrust-vector angle was generally equal to or greater than $\delta_{v,p}$ at low NPR and decreased by up to 3° (fig. 7(b)) as NPR was increased through the test range. The effect of gimballing the nozzle in yaw ($\delta_{v,y} > 0°$) was to increase δ_p. However, the increase in δ_p with increasing $\delta_{v,y}$ would not necessarily indicate an increase in absolute pitch thrust-vector force (normal force) but could be a result of the decrease in axial force (as δ_p is inversely related to F_A). For example, the geometric effect of turning a jet with 10° pitch deflection by 20° in the yaw direction would be an approximate 0.6° apparent increase in the pitch thrust-vector angle. The data in figures 7(b) and 8(b) show a greater increase in δ_p than would be accounted for by this geometric effect; this indicates a small beneficial effect of yaw thrust vectoring on the pitch thrust-vector force. The yaw thrust-vector angle, however, was essentially unaffected by pitch vectoring.

For the hexagonal nozzle at dry power and $\delta_{v,p}$ = 10° (fig. 7(b)), the decrease in resultant thrust ratio as yaw thrust vectoring was increased is not understood. No other configuration exhibited this behavior, including the corresponding afterburning configuration at $\delta_{v,p}$ = 10° (fig. 8(b)). As discussed in the next section, no significant flow-field changes were observed which would explain the loss in resultant thrust.

Pressure Distributions and Flow Visualization

As evident in any of the pressure plots, a complex pressure distribution was created as the flow interacted with the three-dimensional geometry of the nozzle. The pressure distributions are best understood by comparing the data with flow visualization photographs showing both the nozzle geometry and some of the flow features. Pressure distributions with corresponding flow visualization photographs of all configurations (for $\delta_{v,y}$ = 0° only) are presented in figures 10 through 19 at operating conditions of either NPR = 4.5 or 5, depending on the configuration. Each page contains three data plots. In the upper plot, data from the three primary longitudinal rows of pressure orifices are presented to show major trends: one row near the nozzle centerline ($y/(w/2)$ = 0.074), one near midspan ($y/(w/2)$ = 0.481), and one near the sidewall ($y/(w/2)$ = 0.926). In the center plot, two additional rows ($y/(w/2)$ = 0.296 and 0.704) between the aforementioned rows are presented to provide further

detail in the throat region of the nozzle. In the bottom plot, the sidewall pressure distributions are plotted, including a full-length centerline row $(z/(w/2) = 0)$ and two shorter rows $(z/(w/2) = \pm 0.296)$ above and below the centerline, covering approximately the upstream third of the nozzle length.

As discussed in the section "Nozzle Design" and shown in figure 4, each nozzle has four distinct geometry regions: a spherical convergent duct, a slightly divergent plateau, one or two convergent triangular ramps, and a divergent flap. The juncture between the triangular ramps and the divergent flap is a vee formed by skewed ridges with the point facing aft for the bowtie configurations and forward for the hexagonal configurations. By comparing the longitudinal location (x/L) of sonic flow (first occurrence of $p/p_{t,j} = 0.528$) for each of the three primary rows of pressure orifices, one can determine the approximate orientation of the sonic line at the intersection of the throat with the nozzle surface. As seen in any of the plots for flap pressure distribution, the sonic line is oriented approximately along the skewed ridge for all configurations.

Upstream of this ridge, the pressure distributions indicate regions of subsonic expansion and compression (decreasing and increasing $p/p_{t,j}$) as the flow interacted with the changing geometry. (See, for example, fig. 10(a).) Because this region is upstream of the nozzle throat, the surface loadings caused by the expansions and compressions would not significantly affect the net generation of thrust by the nozzle. Possibly thrust efficiency would be slightly reduced as a result of local flow-turning losses. However, because the flow Mach number is still fairly low in these regions, this effect is also unlikely to be significant.

Downstream of the sonic line, the pressure distributions indicate a nonuniform flow field with regions of cross flow for both the bowtie and hexagonal configurations. These configurations are discussed separately.

Bowtie configuration at dry power and $\delta_{v,p} = 0°$. For the bowtie configurations (pressure distributions shown in fig. 10, flow visualization shown in fig. 11), a region of high pressure relative to the inboard regions of the nozzle existed near the sidewalls $(y/(w/2) = 0.926)$ between the sonic line and $x/L \approx 0.575$. The cause of this high-pressure region is indicated in the flow visualization photograph in figure 11(a). The patterns indicate that the flow on the triangular ramp accelerated in a direction perpendicular to the ridge line (i.e., outboard with respect to the nozzle centerline). The interaction of this outward-deflected flow with the sidewall resulted in the high-pressure region near the sidewall and the low-pressure region near the centerline. As a result of this lateral pressure gradient downstream of the skewed ridge, the flow field would be expected to have an inboard cross-flow component from high to low pressure; this is verified by the inward-directed streaklines in the flow visualization photograph.

Farther downstream, as these inboard flows intersected the nozzle symmetry plane at the centerline, an oblique shock system formed to redirect the flow in the axial direction (fig. 11(a)). The shocks emanated from the nozzle centerline at $x/L \approx 0.55$. The shocks are also indicated in the pressure distribution in figure 10(a) as a sudden increase in $p/p_{t,j}$. The pressure rise through the shock is evident near the centerline between $x/L \approx 0.55$ and 0.625. The shock is not seen, however, in either of the other rows of orifices. For the midspan row, the pressure orifices may have been too sparse to indicate the shock (furthermore, the shock appears to have weakened as it progressed outboard). For the row near the sidewall, the shock appears to have been downstream of the last orifice. Momentum losses through this shock system would result in a reduction in resultant thrust ratio. The reduced momentum of the flow downstream of the shock system is evident in the flow visualization photograph in figure 11 where the paint streaks were heavier than they were before the shock system. Higher velocity flow generally has the effect of thinning the paint streaks.

One additional feature indicated in the pressure distributions should be noted. The extreme low pressure immediately downstream of the sonic line (fig. 10: $y/(w/2) = 0.926$ at $x/L \approx 0.35$ and $y/(w/2) = 0.074$ at $x/L \approx 0.4$) followed by a significant increase in pressure suggest the presence of a separation region followed by an oblique shock. No such shock is indicated in the flow visualization photograph. (See fig. 11(a).) However further evidence of a shock in this location is presented in the discussion of the hexagonal configuration in the next section.

Hexagonal configuration at dry power and $\delta_{v,p} = 0°$. The pressure distributions and flow visualization photographs of the hexagonal configurations (figs. 12 and 13) depict a similar but mirror-imaged flow field downstream of the plateau region. The skewed ridges for the hexagonal configuration pointed forward directing flow toward the centerline and resulting in higher pressure in that region $(y/(w/2) = 0.074$ and $0.481)$ and lower pressure near the sidewalls (opposite from that of the bowtie configuration). The flow field generated by this pressure distribution (fig. 13(a)) generally had an outboard cross-flow component resulting in the formation of a pair of oblique shocks emanating in this case from the sidewall region. In the sidewall flow visualization photograph (fig. 13(b)), the emanation point is indicated by the region of pooled paint halfway

down the sidewall. The oblique shock is also indicated in the pressure distributions in figure 12(a) by pressure increases at $x/L = 0.6$ near the sidewall and $x/L = 0.8$ near the centerline. The shock strength appears to have decreased as it approached the centerline. Once again, the pressure taps in the midspan row may have been too sparse to indicate the shock.

The photograph of the flap (fig. 13(a)) may also indicate a pair of oblique shocks emanating from the midspan region of the skewed ridge vee. The pressure data in figure 12 indicate a strong compression just downstream of the aerodynamic throat ($p/p_{t,j} = 0.528$), which confirms the presence of these shocks. A similar pair of shocks emanating from the sidewall at the skewed ridge on the bowtie configuration was indicated by the pressure distributions, although the shocks were not visible in the flow visualization photographs. These shocks are expected to form as the flow crosses perpendicular to the skewed ridge and is redirected aft by interaction with the sidewall (bowtie geometry) or centerline (hexagonal geometry). The photograph of the bowtie configuration (fig. 11(a)) may not have indicated these shocks because, prior to operating the jet, the paint sources were not placed in the locations necessary for indicating the shocks. Because the flow fields of the bowtie and hexagonal configurations were mirror imaged but similar in internal shock structure, the associated thrust loss would be expected to be about the same, which was confirmed by the nozzle performance data in figures 6 and 7; the bowtie and hexagonal configurations had nearly equal levels of thrust efficiency.

Hexagonal configuration at dry power and $\delta_{v,p} = 10°$. The pressure distributions and flow visualization of the hexagonal nozzle at dry power and $\delta_{v,p} = 10°$ (figs. 14 and 15) depict a flow field with some similarities and differences with respect to the unvectored configuration. The pressure distribution on the lower (suction) flap at the midspan location $\left(y/(w/2) = 0.481\right)$ indicates a shock at $x/L \approx 0.4$. The shock can be seen in the flow visualization photograph in figure 15(a) emanating from the skewed ridge and is similar to the shock seen in figure 13(a). The shock is located somewhat farther downstream in the vectored case, and it terminates in a separated region near the sidewalls. Farther downstream, a weak oblique shock emanating from the nozzle centerline may be faintly visible in the flow visualization photograph. A corresponding small increase in pressure is indicated in figure 14(a) near the centerline at $x/L \approx 0.75$. However, unlike the configuration with $\delta_{v,p} = 0°$ which had an oblique shock emanating from the sidewall, the flow visualization of the configuration with $\delta_{v,p} = 10°$ indicates no other significant shocks on the lower flap. On the upper flap (fig. 15(b)), faint indications of a pair of shocks can be seen emanating from the sidewall region (indicated by darker paint marks) approximately halfway down the divergent flap. The sidewall photograph (fig. 15(c)) indicates that these shocks are probably the same shocks seen on the lower flap near the skewed ridge and that the shocks are inclined with respect to the flow-path centerline. The flow patterns upstream of this shock indicate that the flow angle (in the pitch direction) was greater than the lower flap angle (i.e., the flow had overturned). Therefore, the shock was formed to redirect the flow parallel to the lower flap and thereby a reduction was forced in the net turning angle of the flow. Likely, greater pitch thrust-vector angles may be achievable by increasing the lower flap deflection with minimal resulting adverse impact on resultant thrust efficiency (compared with the level at $\delta_{v,p} = 10°$), and even an improvement may be possible in resultant thrust efficiency because the shock and its associated losses would probably disappear.

Immediately upstream of this shock, as seen in the sidewall flow visualization photograph (fig. 15(c)), the streak lines indicate a smooth, continuous turning of the flow absent of any additional shocks near the sidewall. This behavior indicates subsonic turning, which suggests that the aerodynamic sonic line on the upper (pressure) side shifted downstream from the skewed ridge such that the flow was turned before it reached sonic conditions. Unfortunately no pressure data on the upper flap were available to confirm this throat reorientation, and the sidewall pressure data were inconclusive in this regard due to the spacing of the pressure taps. However, a change in the position of the aerodynamic throat of this kind is consistent with the patterns seen in the flow visualization photographs and is typical for nozzles using internal divergent duct deflections to produce thrust vectoring (ref. 9).

As mentioned in the discussion of thrust performance for the hexagonal configuration at dry power and $\delta_{v,p} = 10°$, a decrease in thrust ratio was noted as the yaw gimbal angle was increased from $\delta_{v,y} = 0°$ to $\delta_{v,y} = 10°$. No other configuration exhibited this behavior. Comparison of the lower (suction) flap distributions in figures 14(a) and (b) indicates no significant differences in the pressure field on that flap. Unfortunately, no upper surface pressure measurements were available to indicate any changes to the flow field in that vicinity. The reason for the performance decrease is therefore not understood.

Hexagonal configuration at afterburning power and $\delta_{v,p} = 0°$. The pressure distributions and flow visualization of the afterburning power hexagonal configurations with no pitch thrust vectoring are presented in figures 16 and 17. The data indicate that the flow field is generally similar to the flow field of the dry power

configurations. The subsonic expansion and compression upstream of the throat ridge are more pronounced yet probably still do not significantly affect the nozzle performance. The shocks which emanated from the skewed ridge of the dry power configuration are seen in the afterburning power configuration as well, although the shock angle is larger and the shock origin is clearly the vertex of the skewed ridges. The downstream shocks emanating from the sidewalls, however, are not evident here; this indicates that the existing oblique shocks properly aligned the flow with the divergent flap surfaces.

Hexagonal configuration at afterburning power and $\delta_{v,p}$ ***= 10°.*** The pressure distributions and flow visualization of the pitch thrust-vectored afterburning configuration are depicted in figures 18 and 19. The flow field is similar to the pitch thrust-vectored dry power configuration in that the flow appears to have overturned; this resulted in an oblique shock formation to redirect the flow along the lower flap surface. (See fig. 19(c).) However, the shock appears to have exited the nozzle because no impingement on the upper surface is evident.

Conclusions

The static internal performance of a spherical convergent flap nozzle with a nonrectangular divergent duct was obtained in the model preparation area of the Langley 16-Foot Transonic Tunnel. Duct cross sections of hexagonal and bowtie shapes were tested. Additional geometric parameters included throat area (power setting), pitch flap deflection angle, and yaw gimbal angle. Nozzle pressure ratio was varied from 2 to 12 for dry power configurations and from 2 to 6 for afterburning power configurations. Based on the discussion of results, the following conclusions were obtained:

1. Despite the complex internal geometry of the nozzles, pitch thrust-vector angles exceeding the flap deflection angle were obtained at nearly all afterburning power test conditions and at most dry power test conditions below the design pressure ratio. Flow visualization indicates that the nozzle may be capable of efficient pitch thrust vectoring at flap angles greater than the 10° deflection angles tested.

2. An approximate 1 percent loss in thrust efficiency was incurred for the nozzle with the hexagonal divergent duct relative to a similar nozzle with a rectangular divergent duct. The reduced efficiency was the result of internal oblique shocks in the flow field which formed to compensate for cross flow generated by the vee-shaped geometric throat of the hexagonal nozzle.

3. The hexagonal and bowtie nozzles had mirror-imaged internal flow fields. The similar internal shock structure resulted in similar thrust performance.

NASA Langley Research Center
Hampton, VA 23681-2199
December 2, 1997

References

1. Leavitt, L. D.: Summary of Nonaxisymmetric Nozzle Internal Performance From the NASA Langley Static Test Facility. AIAA-85-1347, July 1985.

2. Berrier, Bobby L.: *Results From NASA Langley Experimental Studies of Multiaxis Thrust Vectoring Nozzles*. SAE Paper 881481, Oct. 1988.

3. Berrier, Bobby L.; and Taylor, John G.: *Internal Performance of Two Nozzles Utilizing Gimbal Concepts for Thrust Vectoring*. NASA TP-2991, 1990.

4. Taylor, John G.: *Internal Performance of a Hybrid Axisymmetric/Nonaxisymmetric Convergent-Divergent Nozzle*. NASA TM-4230, 1991.

5. Wing, David J.; and Capone, Francis J.: *Performance Characteristics of Two Multiaxis Thrust-Vectoring Nozzles at Mach Numbers up to 1.28*. NASA TP-3313, 1993.

6. Capone, Francis J.; Bangert, Linda S.; Asbury, Scott C.; Mills, Charles T. L.; and Bare, E. Ann: *The NASA Langley 16-Foot Transonic Tunnel: Historical Overview, Facility Description, Calibration, Flow Characteristics, and Test Capabilities*. NASA TP-3521, 1995.

7. Mercer, Charles E.; Berrier, Bobby L.; Capone, Francis J.; and Grayston, Alan M.: *Data Reduction Formulas for the 16-Foot Transonic Tunnel: NASA Langley Research Center, Revision 2*. NASA TM-107646, 1992.

8. Coleman, Hugh W.; and Steele, W. Glenn, Jr.: *Experimentation and Uncertainty Analysis for Engineers*. John Wiley & Sons, 1989.

9. Carson, George T., Jr.; and Capone, Francis J.: *Static Internal Performance of an Axisymmetric Nozzle With Multiaxis Thrust-Vectoring Capability*. NASA TM-4237, 1991.

Table 1. Matrix of Configurations Tested

Configuration	Divergent duct cross section	Power setting	$\delta_{v,p}$, deg	$\delta_{v,y}$, deg
1	Bowtie	Dry	0	0
2	↓	↓	↓	10
3	↓	↓	↓	20
4	Hexagonal	↓	↓	0
5	↓	↓	↓	10
6	↓	↓	↓	20
7	↓	↓	10	0
8	↓	↓	↓	10
9	↓	↓	↓	20
10	↓	Afterburning	0	0
11	↓	↓	↓	10
12	↓	↓	↓	20
13	↓	↓	10	0
14	↓	↓	↓	10
15	↓	↓	↓	20

Table 2. Pressure Orifice Coordinates

(a) Hexagonal configurations at dry power

x/L at $y/(w/2)$ of—				
0.074	0.296	0.481	0.704	0.926
Hexagonal configurations at dry power and $\delta_{v,p} = 0°$				
0.143	0.317	0.143	0.284	0.143
0.193		0.193	0.317	0.209
0.242		0.242	0.358	0.251
0.276		0.276		0.276
0.292		0.292		0.292
0.317		0.317		0.317
0.342		0.342		0.342
0.408		0.375		0.375
0.491		0.408		0.408
0.573		0.573		0.491
0.656		0.838		0.573
0.739				0.656
0.838				0.739
0.937				
Hexagonal configurations at dry power and $\delta_{v,p} = 10°$				
0.143	0.325	0.143	0.284	0.143
0.193		0.193	0.325	0.209
0.242		0.242	0.358	0.251
0.276		0.276		0.276
0.292		0.292		0.292
0.325		0.325		0.325
0.350		0.342		0.342
0.424		0.391		0.375
0.491		0.424		0.424
0.573		0.573		0.491
0.656		0.838		0.573
0.739				0.656
0.838				0.739
0.937				

Table 2. Continued

(b) Hexagonal configurations at afterburning power

x/L at $y/(w/2)$ of—				
0.074	0.296	0.481	0.704	0.926
Hexagonal configurations at afterburning power and $\delta_{v,p} = 0°$				
0.143	0.193	0.143	0.209	0.143
0.193	0.242	0.209	0.242	0.185
0.234		0.234	0.276	0.209
0.259		0.259	0.309	0.242
0.276		0.276		0.276
0.300		0.300		0.300
0.325		0.325		0.325
0.408		0.408		0.358
0.491		0.573		0.408
0.573		0.739		0.491
0.656				0.573
0.739				0.656
0.854				
Hexagonal configurations at afterburning power and $\delta_{v,p} = 10°$				
0.143	0.329	0.143	0.284	0.143
0.193		0.193	0.329	0.193
0.242		0.242	0.358	0.242
0.276		0.284		0.267
0.304		0.304		0.292
0.329		0.329		0.329
0.350		0.350		0.358
0.424		0.391		0.375
0.491		0.424		0.424
0.573		0.573		0.491
0.656		0.739		0.557
0.739				0.623
0.838				

Table 2. Concluded

(c) Bowtie configurations at dry power

x/L at $y/(w/2)$ of—				
0.074	0.296	0.481	0.704	0.926
Bowtie configurations at dry power and $\delta_{v,p} = 0°$				
0.143	0.259	0.143	0.226	0.143
0.193	0.317	0.193	0.259	0.193
0.234	0.342	0.226	0.292	0.226
0.276	0.367	0.259	0.325	0.259
0.317	0.400	0.292	0.358	0.292
0.342		0.317		0.317
0.375		0.342		0.342
0.408		0.375		0.375
0.457		0.540		0.457
0.540		0.722		0.540
0.623		0.838		0.623
0.722				0.722
0.838				
0.954				

(d) Sidewall pressure orifices for all configurations

x/L at $z/(w/2)$ of—		
−0.296	0.000	0.296
Sidewall pressure orifices		
0.127	0.127	0.127
0.226	0.226	0.226
0.292	0.292	0.292
0.391	0.391	0.391
	0.474	
	0.573	
	0.755	
	0.937	

Table 3. Internal Static Performance of SCF Nozzle Configuration 1

[Bowtie geometry at dry power, $\delta_{v,p}$ = 0°, and $\delta_{v,y}$ = 0°]

NPR	F_r/F_i	F_A/F_i	δ_p, deg	δ_y, deg
2.002	0.905	0.905	0.9	-0.1
2.492	0.936	0.935	0.7	0.2
2.999	0.954	0.954	0.5	0.1
3.495	0.964	0.964	0.4	0.1
3.997	0.972	0.972	0.3	0.1
4.493	0.975	0.975	0.3	0.0
5.004	0.978	0.978	0.3	0.0
5.497	0.979	0.979	0.2	0.0
5.990	0.978	0.978	0.2	0.0
6.999	0.976	0.976	0.2	0.0
8.006	0.974	0.974	0.1	0.0
8.982	0.971	0.971	0.1	0.0
9.993	0.968	0.968	0.1	0.1
10.995	0.965	0.965	0.1	0.1
11.995	0.962	0.962	0.2	0.1

Table 4. Internal Static Performance of SCF Nozzle Configuration 2

[Bowtie geometry at dry power, $\delta_{v,p}$ = 0°, and $\delta_{v,y}$ = 10°]

NPR	F_r/F_i	F_A/F_i	δ_p, deg	δ_y, deg
1.998	0.911	0.897	0.3	9.9
2.495	0.940	0.925	0.6	10.1
2.993	0.955	0.941	0.3	10.0
3.503	0.966	0.952	0.2	9.8
4.008	0.972	0.958	0.2	9.8
4.495	0.975	0.961	0.1	9.8
5.001	0.976	0.962	0.0	9.8
5.498	0.978	0.963	0.0	9.7
5.985	0.978	0.963	0.0	9.8
6.998	0.975	0.961	0.0	9.8
8.007	0.974	0.959	-0.1	9.9
9.009	0.971	0.956	-0.1	10.0
10.012	0.967	0.953	-0.1	10.0
11.011	0.964	0.950	-0.1	10.1
12.007	0.962	0.947	-0.1	10.1

Table 5. Internal Static Performance of SCF Nozzle Configuration 3

[Bowtie geometry at dry power, $\delta_{v,p}$ = 0°, and $\delta_{v,y}$ = 20°]

NPR	F_r/F_i	F_A/F_i	δ_p, deg	δ_y, deg
2.007	0.910	0.855	0.9	20.1
2.514	0.942	0.884	0.6	20.1
3.000	0.956	0.898	0.3	20.1
3.507	0.967	0.909	0.1	20.0
3.997	0.973	0.915	0.1	19.9
4.489	0.977	0.918	0.0	19.9
4.992	0.979	0.921	0.0	19.9
5.501	0.980	0.922	-0.1	19.9
6.023	0.980	0.922	-0.1	19.9
6.996	0.979	0.920	-0.1	20.0
7.994	0.977	0.918	-0.2	20.1
8.998	0.975	0.915	-0.2	20.2
10.021	0.972	0.912	-0.3	20.3
10.405	0.971	0.911	-0.3	20.3

Table 6. Internal Static Performance of SCF Nozzle Configuration 4

[Hexagonal geometry at dry power, $\delta_{v,p}$ = 0°, and $\delta_{v,y}$ = 0°]

NPR	F_r/F_i	F_A/F_i	δ_p, deg	δ_y, deg
2.014	0.889	0.889	0.6	0.0
2.497	0.924	0.924	0.4	0.1
3.005	0.945	0.945	0.3	0.1
3.508	0.960	0.960	0.2	0.1
4.004	0.968	0.968	0.2	0.1
4.497	0.973	0.973	0.1	0.0
5.006	0.976	0.976	0.1	0.0
5.495	0.977	0.977	0.1	0.0
6.000	0.978	0.978	0.1	0.0
7.000	0.977	0.977	0.0	0.0
8.013	0.974	0.974	0.0	0.0
9.010	0.971	0.971	0.0	0.0
9.994	0.968	0.968	0.0	0.1
11.008	0.965	0.965	0.1	0.1
12.014	0.962	0.962	0.1	0.1

Table 7. Internal Static Performance of SCF Nozzle Configuration 5

[Hexagonal geometry at dry power, $\delta_{v,p}$ = 0°, and $\delta_{v,y}$ = 10°]

NPR	F_r/F_i	F_A/F_i	δ_p, deg	δ_y, deg
1.997	0.888	0.877	1.2	9.2
3.016	0.948	0.934	0.5	9.7
2.512	0.927	0.913	0.7	9.7
3.540	0.962	0.948	0.5	9.7
3.993	0.970	0.956	0.4	9.8
4.499	0.975	0.961	0.3	9.8
5.009	0.978	0.964	0.2	9.7
5.512	0.979	0.965	0.2	9.7
5.993	0.978	0.964	0.2	9.8
6.996	0.977	0.963	0.1	9.8
8.016	0.975	0.961	0.0	9.9
9.016	0.972	0.958	0.0	9.9
10.037	0.969	0.954	0.0	10.0
10.996	0.966	0.951	0.0	10.0
12.030	0.962	0.948	0.0	10.1

Table 8. Internal Static Performance of SCF Nozzle Configuration 6

[Hexagonal geometry at dry power, $\delta_{v,p}$ = 0°, and $\delta_{v,y}$ = 20°]

NPR	F_r/F_i	F_A/F_i	δ_p, deg	δ_y, deg
1.990	0.892	0.841	0.7	19.4
2.506	0.929	0.874	0.4	19.8
2.991	0.948	0.891	0.2	20.0
3.492	0.962	0.904	0.2	19.9
4.002	0.970	0.912	0.1	19.9
4.510	0.974	0.917	0.0	19.8
4.995	0.978	0.920	0.0	19.8
5.493	0.979	0.921	-0.1	19.8
5.981	0.979	0.921	-0.1	19.8
7.007	0.978	0.919	-0.2	20.0
8.008	0.977	0.918	-0.2	20.1
8.968	0.976	0.916	-0.2	20.1
10.012	0.972	0.912	-0.3	20.2
10.389	0.971	0.911	-0.3	20.2

Table 9. Internal Static Performance of SCF Nozzle Configuration 7

[Hexagonal geometry at dry power, $\delta_{v,p}$ = 10°, and $\delta_{v,y}$ = 0°]

NPR	F_r/F_i	F_A/F_i	δ_p, deg	δ_y, deg
1.985	0.945	0.930	10.1	-0.3
2.500	0.964	0.949	10.1	0.0
2.993	0.971	0.956	10.1	0.0
3.507	0.974	0.961	9.5	0.1
3.995	0.975	0.963	9.0	0.1
4.494	0.974	0.963	8.7	0.1
4.993	0.972	0.961	8.4	0.1
5.497	0.969	0.959	8.3	0.0
5.994	0.967	0.957	8.1	0.0
6.998	0.962	0.953	7.9	0.0
7.995	0.957	0.949	7.8	0.0
9.004	0.951	0.942	7.7	0.1
9.986	0.946	0.938	7.7	0.1
10.979	0.942	0.934	7.6	0.1
11.996	0.938	0.930	7.6	0.2

Table 10. Internal Static Performance of SCF Nozzle Configuration 8

[Hexagonal geometry at dry power, $\delta_{v,p}$ = 10°, and $\delta_{v,y}$ = 10°]

NPR	F_r/F_i	F_A/F_i	δ_p, deg	δ_y, deg
1.989	0.928	0.899	10.7	9.8
2.510	0.948	0.918	10.6	9.8
2.991	0.959	0.930	10.4	9.8
3.488	0.965	0.938	9.8	9.7
4.000	0.966	0.940	9.4	9.7
4.485	0.967	0.941	9.0	9.7
5.013	0.966	0.941	8.7	9.7
5.505	0.964	0.941	8.5	9.7
5.989	0.963	0.940	8.3	9.7
7.004	0.958	0.935	8.0	9.7
7.994	0.954	0.932	7.9	9.9
8.996	0.950	0.928	7.7	10.0
9.976	0.946	0.924	7.6	10.0
10.986	0.944	0.921	7.6	10.1
11.971	0.940	0.918	7.5	10.1

Table 11. Internal Static Performance of SCF Nozzle Configuration 9

[Hexagonal geometry at dry power, $\delta_{v,p}$ = 10°, and $\delta_{v,y}$ = 20°]

NPR	F_r/F_i	F_A/F_i	δ_p, deg	δ_y, deg
2.015	0.931	0.860	11.2	19.9
2.497	0.949	0.876	11.1	20.2
3.003	0.958	0.885	11.0	20.2
3.522	0.964	0.892	10.3	20.1
4.015	0.964	0.894	9.8	20.0
4.508	0.965	0.896	9.4	20.0
5.016	0.965	0.897	9.1	20.0
5.520	0.963	0.895	8.9	20.0
6.008	0.962	0.895	8.7	20.0
7.007	0.959	0.892	8.4	20.0
9.000	0.952	0.885	8.0	20.2
10.042	0.948	0.881	7.9	20.3
11.055	0.944	0.878	7.8	20.3
11.593	0.942	0.876	7.8	20.3

Table 12. Internal Static Performance of SCF Nozzle Configuration 10

[Hexagonal geometry at afterburning power, $\delta_{v,p}$ = 0°, and $\delta_{v,y}$ = 0°]

NPR	F_r/F_i	F_A/F_i	δ_p, deg	δ_y, deg
2.004	0.906	0.906	0.5	0.3
2.496	0.937	0.937	0.3	0.2
2.983	0.954	0.954	0.3	0.2
3.505	0.965	0.965	0.2	0.2
4.001	0.971	0.971	0.1	0.2
4.487	0.976	0.976	0.1	0.2
5.000	0.977	0.977	0.1	0.2
5.497	0.978	0.978	0.1	0.2
5.994	0.978	0.978	0.1	0.2
6.209	0.977	0.977	0.1	0.2

Table 13. Internal Static Performance of SCF Nozzle Configuration 11

[Hexagonal geometry at afterburning power, $\delta_{v,p} = 0°$, and $\delta_{v,y} = 10°$]

NPR	F_r/F_i	F_A/F_i	δ_p, deg	δ_y, deg
2.018	0.908	0.894	0.4	10.1
2.494	0.936	0.922	0.3	10.2
3.007	0.954	0.939	0.2	10.2
3.515	0.966	0.951	0.2	10.1
4.009	0.972	0.956	0.1	10.2
4.512	0.976	0.961	0.1	10.2
5.007	0.978	0.963	0.1	10.2
5.507	0.979	0.963	0.1	10.3
6.013	0.979	0.963	0.1	10.3
6.199	0.979	0.963	0.1	10.3

Table 14. Internal Static Performance of SCF Nozzle Configuration 12

[Hexagonal geometry at afterburning power, $\delta_{v,p} = 0°$, and $\delta_{v,y} = 20°$]

NPR	F_r/F_i	F_A/F_i	δ_p, deg	δ_y, deg
2.015	0.910	0.856	0.5	19.9
2.503	0.938	0.880	0.2	20.2
3.017	0.956	0.897	0.2	20.2
3.533	0.967	0.907	0.1	20.3
4.005	0.974	0.913	0.1	20.3
4.492	0.978	0.917	0.0	20.4
5.016	0.981	0.919	0.0	20.4

Table 15. Internal Static Performance of SCF Nozzle Configuration 13

[Hexagonal geometry at afterburning power, $\delta_{v,p} = 10°$, and $\delta_{v,y} = 0°$]

NPR	F_r/F_i	F_A/F_i	δ_p, deg	δ_y, deg
2.006	0.953	0.941	9.2	0.1
2.493	0.966	0.947	11.4	0.2
2.996	0.972	0.953	11.3	0.1
3.503	0.973	0.955	11.1	0.1
3.998	0.972	0.954	10.9	0.1
4.497	0.969	0.952	10.7	0.1
5.012	0.967	0.950	10.6	0.1
5.496	0.964	0.948	10.5	0.1
6.002	0.962	0.946	10.4	0.1
6.173	0.961	0.945	10.4	0.1

Table 16. Internal Static Performance of SCF Nozzle Configuration 14

[Hexagonal geometry at afterburning power, $\delta_{v,p}$ = 10°, and $\delta_{v,y}$ = 10°]

NPR	F_r/F_i	F_A/F_i	δ_p, deg	δ_y, deg
2.004	0.956	0.930	9.6	9.6
2.503	0.966	0.932	11.8	10.0
2.995	0.971	0.937	11.7	10.0
3.493	0.972	0.939	11.4	10.0
3.995	0.971	0.938	11.2	10.1
4.499	0.969	0.937	11.0	10.1
5.008	0.966	0.935	10.8	10.2
5.495	0.964	0.933	10.7	10.2
5.982	0.961	0.931	10.5	10.2
6.181	0.961	0.930	10.5	10.2

Table 17. Internal Static Performance of SCF Nozzle Configuration 15

[Hexagonal geometry at afterburning power, $\delta_{v,p}$ = 10°, and $\delta_{v,y}$ = 20°]

NPR	F_r/F_i	F_A/F_i	δ_p, deg	δ_y, deg
1.998	0.957	0.891	10.0	19.3
2.496	0.967	0.890	12.5	20.1
2.984	0.972	0.894	12.3	20.1
3.499	0.971	0.894	12.1	20.2
3.997	0.971	0.894	11.8	20.2
4.496	0.969	0.893	11.6	20.3
4.996	0.967	0.891	11.4	20.4
5.232	0.966	0.890	11.3	20.4

Table 18. Internal Static Pressure Ratios for SCF Nozzle Configuration 1

[Bowtie geometry at dry power, $\delta_{v,p} = 0°$, and $\delta_{v,y} = 0°$]

$y/(w/2) = 0.074$

	$p/p_{t,j}$ at x/L of—											
NPR	0.143	0.193	0.234	0.276	0.317	0.342	0.375	0.408	0.457	0.540	0.623	0.722
2.002	0.988	0.988	0.982	0.964	0.808	0.847	0.785	0.107	0.237	0.285	0.371	0.449
2.492	0.989	0.988	0.981	0.961	0.806	0.846	0.784	0.105	0.235	0.286	0.372	0.299
2.999	0.988	0.988	0.982	0.962	0.805	0.846	0.784	0.104	0.233	0.287	0.372	0.298
3.495	0.988	0.987	0.981	0.961	0.807	0.846	0.784	0.104	0.232	0.287	0.372	0.297
3.997	0.987	0.986	0.981	0.960	0.811	0.845	0.784	0.103	0.230	0.287	0.372	0.297
4.493	0.988	0.987	0.981	0.960	0.814	0.846	0.784	0.102	0.229	0.288	0.371	0.296
5.004	0.987	0.986	0.980	0.959	0.823	0.845	0.784	0.102	0.227	0.288	0.371	0.295
5.497	0.987	0.986	0.979	0.958	0.835	0.844	0.783	0.101	0.226	0.288	0.371	0.295
5.990	0.987	0.986	0.980	0.958	0.853	0.841	0.783	0.101	0.225	0.288	0.371	0.295
6.999	0.987	0.985	0.979	0.957	0.860	0.840	0.783	0.101	0.224	0.287	0.371	0.294
8.006	0.986	0.985	0.979	0.957	0.854	0.840	0.783	0.100	0.224	0.287	0.370	0.293
8.982	0.986	0.985	0.979	0.957	0.850	0.839	0.783	0.100	0.224	0.287	0.369	0.293
9.993	0.986	0.984	0.978	0.956	0.841	0.839	0.782	0.100	0.223	0.287	0.368	0.293
10.995	0.986	0.984	0.979	0.956	0.834	0.839	0.782	0.100	0.223	0.286	0.367	0.292
11.995	0.986	0.984	0.978	0.956	0.828	0.840	0.781	0.100	0.223	0.286	0.367	0.292

$y/(w/2) = 0.296$

	$p/p_{t,j}$ at x/L of—				
NPR	0.259	0.317	0.342	0.367	0.400
2.002	0.970	0.805	0.832	0.764	0.161
2.492	0.968	0.804	0.833	0.763	0.158
2.999	0.968	0.803	0.833	0.762	0.156
3.495	0.967	0.805	0.833	0.762	0.154
3.997	0.967	0.807	0.834	0.761	0.151
4.493	0.966	0.813	0.835	0.759	0.149
5.004	0.966	0.818	0.837	0.759	0.148
5.497	0.965	0.819	0.840	0.760	0.146
5.990	0.965	0.819	0.843	0.760	0.146
6.999	0.964	0.820	0.844	0.760	0.146
8.006	0.964	0.820	0.844	0.760	0.148
8.982	0.963	0.818	0.842	0.759	0.150
9.993	0.963	0.817	0.841	0.758	0.151
10.995	0.963	0.815	0.840	0.757	0.153
11.995	0.963	0.815	0.838	0.757	0.154

$y/(w/2) = 0.481$

	$p/p_{t,j}$ at x/L of—										
NPR	0.143	0.193	0.226	0.259	0.292	0.317	0.342	0.375	0.540	0.722	0.838
2.002	0.988	0.985	0.978	0.951	0.789	0.789	0.808	0.186	0.327	0.456	0.514
2.492	0.988	0.985	0.979	0.951	0.789	0.789	0.806	0.181	0.326	0.275	0.409
2.999	0.987	0.983	0.977	0.951	0.790	0.790	0.807	0.178	0.326	0.276	0.322
3.495	0.987	0.984	0.978	0.951	0.790	0.791	0.807	0.173	0.325	0.276	0.269
3.997	0.987	0.984	0.977	0.951	0.791	0.792	0.807	0.170	0.325	0.276	0.238
4.493	0.987	0.983	0.977	0.950	0.796	0.797	0.807	0.162	0.324	0.275	0.226
5.004	0.986	0.983	0.976	0.949	0.798	0.799	0.807	0.158	0.323	0.276	0.223
5.497	0.986	0.983	0.976	0.949	0.801	0.805	0.811	0.149	0.322	0.275	0.223
5.990	0.986	0.982	0.976	0.949	0.805	0.809	0.814	0.147	0.322	0.275	0.223
6.999	0.986	0.982	0.975	0.948	0.810	0.814	0.819	0.145	0.321	0.276	0.223
8.006	0.985	0.982	0.975	0.948	0.810	0.813	0.819	0.146	0.320	0.276	0.223
8.982	0.985	0.981	0.974	0.947	0.808	0.811	0.818	0.146	0.320	0.276	0.223
9.993	0.985	0.981	0.974	0.947	0.806	0.808	0.817	0.147	0.319	0.276	0.223
10.995	0.985	0.981	0.974	0.947	0.805	0.806	0.815	0.147	0.319	0.276	0.223
11.995	0.985	0.981	0.974	0.947	0.803	0.804	0.813	0.146	0.318	0.275	0.222

Table 18. Continued

$y/(w/2) = 0.704$

NPR	$p/p_{t,j}$ at x/L of— 0.226	0.259	0.292	0.325	0.358
2.002	0.966	0.732	0.763	0.901	0.376
2.492	0.967	0.732	0.761	0.898	0.377
2.999	0.965	0.733	0.765	0.897	0.378
3.495	0.965	0.734	0.766	0.895	0.378
3.997	0.964	0.733	0.770	0.894	0.377
4.493	0.964	0.734	0.777	0.891	0.375
5.004	0.964	0.735	0.787	0.887	0.370
5.497	0.964	0.735	0.799	0.882	0.359
5.990	0.963	0.736	0.814	0.882	0.349
6.999	0.963	0.731	0.837	0.882	0.324
8.006	0.962	0.723	0.848	0.881	0.297
8.982	0.962	0.719	0.850	0.881	0.293
9.993	0.962	0.720	0.843	0.882	0.290
10.995	0.962	0.724	0.834	0.885	0.292
11.995	0.962	0.727	0.824	0.887	0.294

$y/(w/2) = 0.926$

NPR	$p/p_{t,j}$ at x/L of— 0.143	0.193	0.226	0.259	0.292	0.317	0.342	0.375	0.457	0.540	0.623	0.722
2.002	0.986	0.972	0.762	0.859	0.894	0.869	0.369	0.607	0.490	0.373	0.271	0.489
2.492	0.986	0.969	0.768	0.855	0.891	0.867	0.370	0.606	0.490	0.374	0.271	0.395
2.999	0.985	0.969	0.780	0.856	0.891	0.865	0.369	0.603	0.490	0.373	0.271	0.318
3.495	0.986	0.968	0.784	0.854	0.891	0.864	0.366	0.603	0.490	0.373	0.272	0.269
3.997	0.984	0.968	0.794	0.855	0.891	0.864	0.364	0.602	0.489	0.373	0.271	0.235
4.493	0.984	0.967	0.802	0.854	0.890	0.862	0.362	0.601	0.489	0.372	0.271	0.207
5.004	0.984	0.967	0.806	0.854	0.891	0.862	0.365	0.601	0.488	0.372	0.271	0.194
5.497	0.984	0.967	0.809	0.855	0.891	0.863	0.368	0.600	0.488	0.371	0.270	0.187
5.990	0.984	0.966	0.810	0.857	0.891	0.862	0.365	0.599	0.487	0.371	0.270	0.183
6.999	0.983	0.966	0.812	0.859	0.892	0.862	0.366	0.595	0.487	0.371	0.270	0.178
8.006	0.983	0.966	0.812	0.860	0.893	0.862	0.369	0.591	0.487	0.370	0.270	0.176
8.982	0.983	0.965	0.811	0.860	0.893	0.862	0.375	0.592	0.487	0.370	0.270	0.174
9.993	0.983	0.966	0.809	0.859	0.892	0.860	0.378	0.591	0.486	0.370	0.270	0.173
10.995	0.983	0.965	0.805	0.858	0.891	0.860	0.382	0.590	0.486	0.369	0.271	0.173
11.995	0.983	0.965	0.800	0.858	0.890	0.859	0.383	0.591	0.485	0.368	0.271	0.172

Table 18. Concluded

Sidewall: $z/(w/2) = 0.296$

	$p/p_{t,j}$ at x/L of—			
NPR	0.127	0.226	0.292	0.391
2.002	0.986	0.720	0.826	0.579
2.492	0.985	0.718	0.825	0.579
2.999	0.984	0.716	0.826	0.579
3.495	0.984	0.710	0.825	0.576
3.997	0.983	0.704	0.825	0.576
4.493	0.982	0.699	0.825	0.575
5.004	0.982	0.700	0.825	0.575
5.497	0.982	0.700	0.826	0.573
5.990	0.982	0.699	0.827	0.573
6.999	0.981	0.700	0.828	0.571
8.006	0.981	0.701	0.829	0.570
8.982	0.981	0.701	0.828	0.570
9.993	0.980	0.702	0.827	0.570
10.995	0.981	0.702	0.827	0.569
11.995	0.981	0.702	0.826	0.570

Sidewall: $z/(w/2) = 0.000$

	$p/p_{t,j}$ at x/L of—							
NPR	0.127	0.226	0.292	0.391	0.474	0.573	0.755	0.937
2.002	0.986	0.902	0.820	0.611	0.458	0.336	0.456	0.502
2.492	0.985	0.899	0.818	0.609	0.457	0.336	0.369	0.404
2.999	0.984	0.898	0.819	0.608	0.457	0.336	0.191	0.339
3.495	0.983	0.897	0.818	0.607	0.457	0.336	0.191	0.280
3.997	0.983	0.896	0.818	0.607	0.457	0.336	0.191	0.225
4.493	0.983	0.894	0.816	0.606	0.456	0.336	0.190	0.202
5.004	0.982	0.892	0.816	0.605	0.455	0.336	0.190	0.189
5.497	0.982	0.891	0.816	0.605	0.454	0.336	0.190	0.182
5.990	0.982	0.890	0.817	0.605	0.453	0.335	0.189	0.177
6.999	0.982	0.890	0.818	0.604	0.452	0.335	0.189	0.172
8.006	0.982	0.889	0.818	0.603	0.451	0.334	0.188	0.171
8.982	0.981	0.889	0.817	0.603	0.451	0.334	0.188	0.170
9.993	0.981	0.889	0.817	0.602	0.450	0.333	0.187	0.170
10.995	0.981	0.889	0.817	0.602	0.450	0.333	0.187	0.170
11.995	0.981	0.889	0.817	0.602	0.449	0.332	0.187	0.170

Sidewall: $z/(w/2) = -0.296$

	$p/p_{t,j}$ at x/L of—			
NPR	0.127	0.226	0.292	0.391
2.002	0.985	0.713	0.825	0.581
2.492	0.985	0.707	0.824	0.581
2.999	0.983	0.701	0.824	0.580
3.495	0.984	0.697	0.824	0.579
3.997	0.984	0.696	0.824	0.578
4.493	0.983	0.695	0.824	0.576
5.004	0.983	0.696	0.825	0.574
5.497	0.982	0.698	0.826	0.573
5.990	0.983	0.699	0.827	0.573
6.999	0.982	0.702	0.828	0.572
8.006	0.982	0.704	0.828	0.572
8.982	0.982	0.705	0.828	0.571
9.993	0.982	0.704	0.826	0.572
10.995	0.982	0.704	0.826	0.571
11.995	0.982	0.703	0.825	0.571

Table 19. Internal Static Pressure Ratios for SCF Nozzle Configuration 2

[Bowtie geometry at dry power, $\delta_{v,p} = 0°$, and $\delta_{v,y} = 10°$]

$y/(w/2) = 0.074$

	$p/p_{t,j}$ at x/L of—											
NPR	0.143	0.193	0.234	0.276	0.317	0.342	0.375	0.408	0.457	0.540	0.623	0.722
1.998	0.989	0.989	0.982	0.962	0.807	0.845	0.783	0.106	0.242	0.285	0.371	0.476
2.495	0.990	0.990	0.982	0.961	0.805	0.845	0.783	0.105	0.239	0.286	0.372	0.300
2.993	0.990	0.989	0.982	0.961	0.807	0.845	0.783	0.103	0.236	0.287	0.372	0.299
3.503	0.988	0.988	0.982	0.961	0.810	0.845	0.783	0.103	0.234	0.287	0.372	0.299
4.008	0.988	0.988	0.982	0.960	0.820	0.843	0.783	0.102	0.231	0.287	0.372	0.298
4.495	0.989	0.988	0.981	0.960	0.828	0.841	0.783	0.102	0.229	0.287	0.372	0.298
5.001	0.988	0.988	0.981	0.959	0.824	0.844	0.783	0.102	0.228	0.288	0.371	0.297
5.498	0.988	0.987	0.981	0.958	0.830	0.844	0.783	0.101	0.226	0.288	0.370	0.296
5.985	0.988	0.987	0.980	0.958	0.843	0.842	0.784	0.101	0.223	0.288	0.370	0.296
6.998	0.988	0.986	0.980	0.958	0.857	0.840	0.783	0.100	0.221	0.288	0.369	0.295
8.007	0.987	0.986	0.980	0.957	0.852	0.840	0.783	0.100	0.220	0.288	0.369	0.294
9.009	0.987	0.985	0.980	0.957	0.842	0.840	0.783	0.100	0.220	0.287	0.368	0.293
10.012	0.987	0.985	0.979	0.957	0.835	0.840	0.782	0.100	0.221	0.287	0.368	0.291
11.011	0.986	0.985	0.979	0.956	0.829	0.840	0.781	0.100	0.221	0.286	0.367	0.289
12.007	0.986	0.985	0.979	0.956	0.826	0.840	0.781	0.100	0.221	0.285	0.367	0.288

$y/(w/2) = 0.296$

	$p/p_{t,j}$ at x/L of—				
NPR	0.259	0.317	0.342	0.367	0.400
1.998	0.968	0.803	0.833	0.763	0.164
2.495	0.968	0.803	0.834	0.763	0.160
2.993	0.969	0.804	0.835	0.762	0.158
3.503	0.967	0.806	0.834	0.762	0.156
4.008	0.967	0.808	0.834	0.761	0.155
4.495	0.967	0.812	0.833	0.759	0.154
5.001	0.967	0.822	0.835	0.758	0.150
5.498	0.966	0.823	0.838	0.759	0.148
5.985	0.965	0.822	0.840	0.759	0.146
6.998	0.965	0.822	0.843	0.760	0.146
8.007	0.964	0.821	0.842	0.759	0.148
9.009	0.964	0.820	0.841	0.759	0.150
10.012	0.964	0.818	0.839	0.758	0.152
11.011	0.963	0.817	0.838	0.757	0.153
12.007	0.963	0.816	0.837	0.756	0.155

$y/(w/2) = 0.481$

	$p/p_{t,j}$ at x/L of—										
NPR	0.143	0.193	0.226	0.259	0.292	0.317	0.342	0.375	0.540	0.722	0.838
1.998	0.990	0.986	0.980	0.951	0.789	0.789	0.808	0.197	0.326	0.480	0.516
2.495	0.989	0.986	0.980	0.951	0.789	0.789	0.808	0.196	0.326	0.278	0.416
2.993	0.989	0.986	0.979	0.951	0.789	0.790	0.808	0.191	0.326	0.277	0.323
3.503	0.989	0.985	0.979	0.951	0.789	0.791	0.808	0.187	0.325	0.278	0.271
4.008	0.989	0.985	0.978	0.951	0.790	0.791	0.808	0.183	0.325	0.277	0.240
4.495	0.989	0.984	0.978	0.951	0.791	0.793	0.808	0.178	0.324	0.277	0.226
5.001	0.988	0.985	0.977	0.950	0.794	0.797	0.808	0.172	0.324	0.277	0.224
5.498	0.988	0.984	0.977	0.950	0.798	0.802	0.809	0.162	0.323	0.277	0.223
5.985	0.988	0.984	0.977	0.949	0.802	0.807	0.812	0.154	0.323	0.276	0.223
6.998	0.987	0.983	0.977	0.949	0.810	0.815	0.819	0.148	0.322	0.276	0.222
8.007	0.987	0.983	0.976	0.948	0.808	0.814	0.820	0.149	0.321	0.277	0.222
9.009	0.987	0.983	0.976	0.948	0.806	0.811	0.820	0.152	0.320	0.277	0.222
10.012	0.987	0.983	0.975	0.948	0.804	0.808	0.818	0.153	0.319	0.277	0.222
11.011	0.986	0.983	0.975	0.947	0.802	0.805	0.816	0.153	0.318	0.278	0.221
12.007	0.986	0.982	0.975	0.947	0.801	0.803	0.814	0.152	0.318	0.277	0.221

Table 19. Continued

$y/(w/2) = 0.704$

NPR	$p/p_{t,j}$ at x/L of— 0.226	0.259	0.292	0.325	0.358
1.998	0.975	0.728	0.770	0.907	0.373
2.495	0.974	0.728	0.769	0.905	0.376
2.993	0.972	0.728	0.772	0.905	0.377
3.503	0.972	0.727	0.774	0.905	0.377
4.008	0.971	0.725	0.778	0.903	0.377
4.495	0.970	0.725	0.783	0.900	0.375
5.001	0.970	0.727	0.794	0.897	0.373
5.498	0.970	0.727	0.807	0.892	0.366
5.985	0.969	0.730	0.820	0.887	0.359
6.998	0.968	0.728	0.848	0.882	0.339
8.007	0.967	0.716	0.861	0.879	0.311
9.009	0.966	0.711	0.866	0.877	0.302
10.012	0.966	0.713	0.863	0.878	0.305
11.011	0.965	0.714	0.856	0.879	0.305
12.007	0.965	0.720	0.847	0.882	0.304

$y/(w/2) = 0.926$

NPR	$p/p_{t,j}$ at x/L of— 0.143	0.193	0.226	0.259	0.292	0.317	0.342	0.375	0.457	0.540	0.623	0.722
1.998	0.994	0.979	0.765	0.866	0.901	0.877	0.371	0.613	0.490	0.374	0.262	0.495
2.495	0.994	0.979	0.775	0.864	0.899	0.875	0.372	0.612	0.491	0.374	0.262	0.399
2.993	0.992	0.977	0.785	0.864	0.899	0.874	0.369	0.611	0.490	0.374	0.264	0.322
3.503	0.992	0.976	0.791	0.862	0.899	0.872	0.368	0.609	0.490	0.374	0.265	0.270
4.008	0.991	0.975	0.798	0.862	0.898	0.871	0.368	0.608	0.490	0.374	0.266	0.236
4.495	0.989	0.974	0.803	0.861	0.897	0.869	0.365	0.606	0.490	0.374	0.266	0.207
5.001	0.989	0.974	0.810	0.861	0.897	0.869	0.365	0.606	0.490	0.374	0.267	0.195
5.498	0.989	0.973	0.814	0.861	0.896	0.869	0.364	0.605	0.489	0.374	0.268	0.188
5.985	0.988	0.972	0.817	0.862	0.896	0.868	0.363	0.603	0.489	0.374	0.268	0.184
6.998	0.988	0.971	0.820	0.864	0.897	0.868	0.365	0.602	0.489	0.374	0.269	0.180
8.007	0.987	0.970	0.820	0.864	0.896	0.867	0.367	0.599	0.488	0.373	0.270	0.178
9.009	0.986	0.970	0.819	0.863	0.895	0.866	0.375	0.596	0.488	0.373	0.271	0.177
10.012	0.986	0.970	0.819	0.863	0.895	0.865	0.378	0.596	0.487	0.372	0.275	0.177
11.011	0.985	0.969	0.817	0.862	0.894	0.864	0.380	0.593	0.486	0.371	0.277	0.176
12.007	0.985	0.969	0.812	0.861	0.893	0.863	0.381	0.592	0.486	0.370	0.277	0.176

Table 19. Concluded

Sidewall: $z/(w/2) = 0.296$

NPR	$p/p_{t,j}$ at x/L of— 0.127	0.226	0.292	0.391
1.998	0.995	0.733	0.834	0.587
2.495	0.994	0.730	0.833	0.587
2.993	0.992	0.726	0.834	0.585
3.503	0.990	0.721	0.833	0.584
4.008	0.990	0.717	0.831	0.583
4.495	0.989	0.714	0.831	0.581
5.001	0.989	0.711	0.832	0.581
5.498	0.988	0.710	0.832	0.580
5.985	0.987	0.710	0.832	0.579
6.998	0.987	0.711	0.833	0.577
8.007	0.986	0.710	0.833	0.575
9.009	0.985	0.711	0.832	0.574
10.012	0.985	0.712	0.832	0.574
11.011	0.985	0.712	0.831	0.573
12.007	0.984	0.712	0.830	0.573

Sidewall: $z/(w/2) = 0.000$

NPR	$p/p_{t,j}$ at x/L of— 0.127	0.226	0.292	0.391	0.474	0.573	0.755	0.937
1.998	0.993	0.911	0.827	0.619	0.459	0.336	0.474	0.506
2.495	0.992	0.910	0.826	0.616	0.459	0.337	0.385	0.406
2.993	0.991	0.908	0.827	0.615	0.459	0.337	0.194	0.341
3.503	0.990	0.907	0.826	0.614	0.458	0.337	0.193	0.279
4.008	0.989	0.906	0.825	0.614	0.458	0.337	0.193	0.226
4.495	0.989	0.904	0.824	0.612	0.458	0.336	0.193	0.203
5.001	0.989	0.903	0.824	0.612	0.457	0.336	0.192	0.191
5.498	0.988	0.901	0.823	0.612	0.456	0.336	0.192	0.182
5.985	0.987	0.899	0.823	0.611	0.455	0.335	0.191	0.178
6.998	0.987	0.898	0.824	0.610	0.454	0.335	0.191	0.173
8.007	0.986	0.897	0.823	0.609	0.454	0.334	0.190	0.172
9.009	0.986	0.896	0.823	0.608	0.453	0.333	0.190	0.171
10.012	0.985	0.896	0.823	0.607	0.451	0.332	0.189	0.171
11.011	0.985	0.896	0.822	0.606	0.451	0.331	0.189	0.171
12.007	0.985	0.896	0.822	0.605	0.450	0.331	0.188	0.171

Sidewall: $z/(w/2) = -0.296$

NPR	$p/p_{t,j}$ at x/L of— 0.127	0.226	0.292	0.391
1.998	0.990	0.729	0.830	0.587
2.495	0.990	0.722	0.830	0.587
2.993	0.990	0.717	0.830	0.585
3.503	0.989	0.713	0.830	0.584
4.008	0.989	0.711	0.830	0.584
4.495	0.988	0.710	0.829	0.583
5.001	0.989	0.710	0.830	0.582
5.498	0.988	0.711	0.831	0.583
5.985	0.988	0.711	0.830	0.582
6.998	0.988	0.714	0.831	0.582
8.007	0.987	0.715	0.831	0.580
9.009	0.986	0.715	0.831	0.578
10.012	0.986	0.716	0.831	0.577
11.011	0.985	0.716	0.830	0.575
12.007	0.985	0.715	0.830	0.575

Table 20. Internal Static Pressure Ratios for SCF Nozzle Configuration 3

[Bowtie geometry at dry power, $\delta_{v,p} = 0°$, and $\delta_{v,y} = 20°$]

$y/(w/2) = 0.074$

	$p/p_{t,j}$ at x/L of—											
NPR	0.143	0.193	0.234	0.276	0.317	0.342	0.375	0.408	0.457	0.540	0.623	0.722
2.007	0.992	0.992	0.985	0.967	0.810	0.849	0.786	0.108	0.252	0.285	0.371	0.453
2.514	0.993	0.992	0.985	0.966	0.811	0.847	0.786	0.107	0.249	0.286	0.371	0.297
3.000	0.992	0.991	0.986	0.965	0.824	0.842	0.784	0.104	0.246	0.287	0.371	0.297
3.507	0.991	0.991	0.985	0.965	0.827	0.841	0.785	0.104	0.242	0.287	0.371	0.297
3.997	0.991	0.990	0.985	0.965	0.831	0.841	0.784	0.103	0.240	0.287	0.370	0.296
4.489	0.991	0.990	0.984	0.964	0.829	0.844	0.783	0.103	0.239	0.287	0.370	0.295
4.992	0.990	0.989	0.983	0.963	0.833	0.844	0.784	0.102	0.228	0.288	0.370	0.295
5.501	0.990	0.989	0.983	0.963	0.838	0.844	0.783	0.102	0.224	0.287	0.370	0.295
6.023	0.989	0.988	0.983	0.962	0.841	0.844	0.783	0.101	0.221	0.287	0.369	0.295
6.996	0.989	0.988	0.983	0.961	0.844	0.843	0.783	0.101	0.219	0.287	0.368	0.294
7.994	0.988	0.987	0.982	0.960	0.843	0.843	0.783	0.101	0.219	0.287	0.367	0.293
8.998	0.989	0.987	0.982	0.960	0.836	0.843	0.782	0.101	0.220	0.286	0.367	0.291
10.021	0.988	0.987	0.982	0.960	0.831	0.843	0.781	0.101	0.220	0.286	0.366	0.289
10.405	0.988	0.987	0.982	0.960	0.830	0.843	0.781	0.101	0.221	0.285	0.366	0.288

$y/(w/2) = 0.296$

	$p/p_{t,j}$ at x/L of—				
NPR	0.259	0.317	0.342	0.367	0.400
2.007	0.973	0.808	0.837	0.763	0.173
2.514	0.971	0.808	0.836	0.762	0.169
3.000	0.971	0.809	0.834	0.761	0.168
3.507	0.970	0.810	0.835	0.761	0.165
3.997	0.970	0.813	0.834	0.760	0.160
4.489	0.969	0.819	0.834	0.758	0.154
4.992	0.968	0.823	0.836	0.758	0.151
5.501	0.967	0.825	0.840	0.758	0.152
6.023	0.967	0.823	0.842	0.759	0.152
6.996	0.966	0.823	0.843	0.759	0.149
7.994	0.965	0.823	0.843	0.758	0.148
8.998	0.965	0.823	0.842	0.757	0.149
10.021	0.965	0.823	0.840	0.757	0.150
10.405	0.964	0.822	0.840	0.757	0.152

$y/(w/2) = 0.481$

	$p/p_{t,j}$ at x/L of—										
NPR	0.143	0.193	0.226	0.259	0.292	0.317	0.342	0.375	0.540	0.722	0.838
2.007	0.992	0.989	0.983	0.956	0.790	0.791	0.811	0.227	0.325	0.453	0.513
2.514	0.992	0.988	0.981	0.955	0.790	0.792	0.811	0.228	0.325	0.277	0.402
3.000	0.991	0.987	0.982	0.955	0.790	0.792	0.811	0.227	0.325	0.278	0.326
3.507	0.991	0.987	0.981	0.954	0.790	0.793	0.812	0.224	0.324	0.278	0.271
3.997	0.990	0.987	0.980	0.953	0.789	0.796	0.812	0.219	0.324	0.277	0.240
4.489	0.990	0.986	0.980	0.953	0.792	0.797	0.810	0.221	0.324	0.277	0.227
4.992	0.989	0.986	0.979	0.952	0.794	0.802	0.812	0.179	0.324	0.276	0.224
5.501	0.988	0.985	0.978	0.952	0.799	0.806	0.812	0.161	0.324	0.276	0.223
6.023	0.988	0.985	0.978	0.951	0.804	0.811	0.816	0.151	0.324	0.276	0.222
6.996	0.988	0.985	0.978	0.950	0.808	0.816	0.821	0.148	0.323	0.276	0.221
7.994	0.987	0.984	0.977	0.948	0.805	0.814	0.822	0.152	0.322	0.276	0.221
8.998	0.987	0.984	0.977	0.948	0.803	0.812	0.822	0.156	0.321	0.276	0.221
10.021	0.987	0.984	0.977	0.948	0.801	0.809	0.822	0.159	0.320	0.276	0.220
10.405	0.987	0.984	0.977	0.948	0.801	0.808	0.821	0.165	0.319	0.276	0.221

Table 20. Continued

$y/(w/2) = 0.704$

NPR	$p/p_{t,j}$ at x/L of— 0.226	0.259	0.292	0.325	0.358
2.007	0.972	0.723	0.790	0.908	0.361
2.514	0.971	0.721	0.790	0.906	0.364
3.000	0.969	0.720	0.793	0.905	0.364
3.507	0.968	0.721	0.796	0.902	0.365
3.997	0.967	0.723	0.801	0.898	0.365
4.489	0.967	0.713	0.822	0.895	0.357
4.992	0.966	0.722	0.820	0.892	0.369
5.501	0.966	0.723	0.834	0.889	0.366
6.023	0.965	0.725	0.848	0.884	0.360
6.996	0.964	0.716	0.867	0.879	0.354
7.994	0.963	0.708	0.877	0.875	0.341
8.998	0.963	0.708	0.880	0.872	0.324
10.021	0.963	0.710	0.879	0.872	0.324
10.405	0.963	0.711	0.877	0.872	0.326

$y/(w/2) = 0.926$

NPR	$p/p_{t,j}$ at x/L of— 0.143	0.193	0.226	0.259	0.292	0.317	0.342	0.375	0.457	0.540	0.623	0.722
2.007	0.991	0.978	0.786	0.867	0.899	0.876	0.375	0.611	0.492	0.376	0.274	0.489
2.514	0.992	0.976	0.793	0.865	0.897	0.874	0.374	0.610	0.492	0.376	0.274	0.392
3.000	0.990	0.975	0.800	0.864	0.897	0.873	0.373	0.608	0.492	0.376	0.273	0.316
3.507	0.989	0.974	0.807	0.863	0.896	0.870	0.370	0.608	0.492	0.376	0.272	0.269
3.997	0.988	0.973	0.812	0.863	0.895	0.869	0.368	0.606	0.491	0.376	0.272	0.234
4.489	0.988	0.973	0.818	0.862	0.894	0.869	0.369	0.605	0.491	0.375	0.272	0.207
4.992	0.986	0.972	0.821	0.861	0.896	0.871	0.384	0.604	0.490	0.375	0.272	0.194
5.501	0.987	0.971	0.823	0.862	0.895	0.868	0.369	0.602	0.490	0.375	0.272	0.187
6.023	0.986	0.971	0.824	0.862	0.895	0.868	0.370	0.600	0.490	0.375	0.272	0.182
6.996	0.986	0.971	0.825	0.864	0.895	0.868	0.370	0.597	0.490	0.375	0.272	0.177
7.994	0.985	0.970	0.825	0.864	0.895	0.867	0.372	0.595	0.489	0.374	0.271	0.174
8.998	0.984	0.969	0.824	0.864	0.895	0.866	0.374	0.594	0.488	0.373	0.271	0.173
10.021	0.984	0.969	0.823	0.863	0.894	0.865	0.375	0.594	0.487	0.372	0.271	0.172
10.405	0.984	0.969	0.822	0.863	0.894	0.865	0.376	0.594	0.487	0.372	0.271	0.171

Table 20. Concluded

Sidewall: $z/(w/2) = 0.296$

	$p/p_{t,j}$ at x/L of—			
NPR	0.127	0.226	0.292	0.391
2.007	0.991	0.736	0.836	0.588
2.514	0.990	0.731	0.835	0.587
3.000	0.989	0.728	0.834	0.585
3.507	0.989	0.723	0.834	0.584
3.997	0.988	0.721	0.832	0.583
4.489	0.987	0.719	0.833	0.582
4.992	0.987	0.718	0.833	0.581
5.501	0.986	0.717	0.833	0.580
6.023	0.986	0.717	0.834	0.579
6.996	0.986	0.717	0.833	0.576
7.994	0.985	0.717	0.833	0.575
8.998	0.985	0.717	0.833	0.574
10.021	0.985	0.718	0.833	0.574
10.405	0.985	0.718	0.833	0.574

Sidewall: $z/(w/2) = 0.000$

	$p/p_{t,j}$ at x/L of—							
NPR	0.127	0.226	0.292	0.391	0.474	0.573	0.755	0.937
2.007	0.991	0.914	0.828	0.618	0.462	0.337	0.452	0.503
2.514	0.991	0.911	0.828	0.616	0.461	0.337	0.368	0.405
3.000	0.990	0.909	0.826	0.615	0.461	0.337	0.192	0.340
3.507	0.989	0.908	0.825	0.613	0.461	0.337	0.192	0.277
3.997	0.989	0.906	0.824	0.613	0.460	0.336	0.192	0.226
4.489	0.989	0.904	0.825	0.613	0.459	0.336	0.191	0.205
4.992	0.987	0.903	0.824	0.611	0.459	0.336	0.191	0.191
5.501	0.987	0.902	0.824	0.611	0.458	0.335	0.191	0.183
6.023	0.987	0.901	0.824	0.610	0.458	0.335	0.191	0.178
6.996	0.986	0.900	0.824	0.610	0.457	0.334	0.190	0.173
7.994	0.986	0.899	0.824	0.609	0.455	0.333	0.190	0.172
8.998	0.985	0.898	0.824	0.608	0.454	0.333	0.189	0.171
10.021	0.985	0.898	0.823	0.608	0.453	0.332	0.188	0.171
10.405	0.985	0.898	0.823	0.608	0.453	0.332	0.188	0.171

Sidewall: $z/(w/2) = -0.296$

	$p/p_{t,j}$ at x/L of—			
NPR	0.127	0.226	0.292	0.391
2.007	0.991	0.736	0.833	0.591
2.514	0.991	0.728	0.833	0.589
3.000	0.990	0.723	0.832	0.588
3.507	0.989	0.719	0.832	0.588
3.997	0.988	0.717	0.832	0.586
4.489	0.988	0.718	0.832	0.587
4.992	0.987	0.718	0.832	0.586
5.501	0.987	0.718	0.832	0.586
6.023	0.986	0.719	0.831	0.586
6.996	0.986	0.720	0.832	0.587
7.994	0.985	0.721	0.832	0.584
8.998	0.985	0.722	0.832	0.584
10.021	0.985	0.722	0.832	0.583
10.405	0.985	0.722	0.832	0.583

Table 21. Internal Static Pressure Ratios for SCF Nozzle Configuration 4

[Hexagonal geometry at dry power, $\delta_{v,p} = 0°$, and $\delta_{v,y} = 0°$]

$y/(w/2) = 0.074$

	$p/p_{t,j}$ at x/L of—											
NPR	0.143	0.193	0.242	0.276	0.292	0.317	0.342	0.408	0.491	0.573	0.656	0.739
2.014	0.990	0.986	0.978	0.949	0.860	0.699	0.391	0.526	0.422	0.318	0.246	0.381
2.497	0.989	0.986	0.978	0.949	0.858	0.702	0.387	0.526	0.422	0.319	0.246	0.193
3.005	0.989	0.985	0.978	0.949	0.857	0.703	0.381	0.526	0.423	0.320	0.246	0.193
3.508	0.989	0.986	0.978	0.950	0.855	0.708	0.365	0.526	0.423	0.320	0.247	0.193
4.004	0.988	0.986	0.978	0.950	0.850	0.732	0.358	0.527	0.423	0.321	0.247	0.194
4.497	0.988	0.986	0.978	0.949	0.845	0.757	0.361	0.527	0.423	0.321	0.247	0.194
5.006	0.989	0.985	0.978	0.949	0.843	0.764	0.361	0.527	0.423	0.321	0.247	0.194
5.495	0.988	0.985	0.978	0.949	0.842	0.764	0.360	0.528	0.424	0.321	0.247	0.194
6.000	0.988	0.985	0.978	0.949	0.842	0.760	0.358	0.528	0.423	0.321	0.247	0.194
7.000	0.988	0.985	0.978	0.948	0.840	0.763	0.354	0.527	0.423	0.320	0.246	0.193
8.013	0.988	0.985	0.977	0.949	0.841	0.757	0.348	0.527	0.422	0.320	0.246	0.193
9.010	0.988	0.985	0.977	0.949	0.842	0.749	0.345	0.526	0.422	0.319	0.245	0.193
9.994	0.988	0.985	0.978	0.949	0.843	0.741	0.345	0.525	0.421	0.318	0.245	0.192
11.008	0.988	0.985	0.977	0.949	0.844	0.734	0.347	0.524	0.421	0.318	0.244	0.192
12.014	0.987	0.985	0.977	0.949	0.845	0.730	0.352	0.523	0.420	0.318	0.244	0.192

$y/(w/2) = 0.296$

	$p/p_{t,j}$ at x/L of—
NPR	0.317
2.014	0.774
2.497	0.775
3.005	0.774
3.508	0.769
4.004	0.769
4.497	0.775
5.006	0.781
5.495	0.786
6.000	0.790
7.000	0.793
8.013	0.793
9.010	0.790
9.994	0.788
11.008	0.786
12.014	0.784

$y/(w/2) = 0.481$

	$p/p_{t,j}$ at x/L of—										
NPR	0.143	0.193	0.242	0.276	0.292	0.317	0.342	0.375	0.408	0.573	0.838
2.014	0.985	0.984	0.968	0.783	0.823	0.756	0.801	0.160	0.486	0.296	0.485
2.497	0.984	0.983	0.967	0.779	0.824	0.760	0.803	0.157	0.485	0.296	0.378
3.005	0.985	0.983	0.967	0.773	0.821	0.767	0.809	0.154	0.481	0.297	0.284
3.508	0.985	0.983	0.968	0.765	0.816	0.773	0.817	0.154	0.475	0.297	0.223
4.004	0.986	0.983	0.969	0.762	0.814	0.774	0.824	0.150	0.474	0.297	0.216
4.497	0.986	0.983	0.968	0.762	0.809	0.775	0.829	0.148	0.472	0.297	0.216
5.006	0.986	0.982	0.968	0.752	0.800	0.781	0.834	0.146	0.467	0.297	0.216
5.495	0.986	0.983	0.968	0.737	0.792	0.789	0.838	0.143	0.464	0.296	0.216
6.000	0.986	0.982	0.968	0.730	0.791	0.790	0.842	0.141	0.460	0.296	0.216
7.000	0.986	0.982	0.967	0.731	0.796	0.785	0.843	0.140	0.456	0.296	0.216
8.013	0.986	0.982	0.968	0.737	0.802	0.780	0.843	0.139	0.454	0.295	0.216
9.010	0.986	0.982	0.967	0.741	0.804	0.776	0.842	0.139	0.454	0.295	0.216
9.994	0.986	0.982	0.967	0.745	0.806	0.773	0.840	0.139	0.454	0.294	0.216
11.008	0.986	0.982	0.967	0.747	0.807	0.772	0.838	0.140	0.454	0.293	0.216
12.014	0.986	0.982	0.967	0.750	0.808	0.771	0.836	0.141	0.455	0.293	0.215

Table 21. Continued

$y/(w/2) = 0.704$

NPR	$p/p_{t,j}$ at x/L of— 0.284	0.317	0.358
2.014	0.767	0.949	0.833
2.497	0.779	0.948	0.834
3.005	0.795	0.947	0.834
3.508	0.820	0.942	0.834
4.004	0.831	0.940	0.833
4.497	0.821	0.944	0.832
5.006	0.817	0.947	0.832
5.495	0.818	0.948	0.832
6.000	0.816	0.948	0.831
7.000	0.813	0.949	0.831
8.013	0.809	0.949	0.831
9.010	0.806	0.949	0.831
9.994	0.802	0.949	0.831
11.008	0.799	0.948	0.830
12.014	0.795	0.948	0.830

$y/(w/2) = 0.926$

NPR	$p/p_{t,j}$ at x/L of— 0.143	0.209	0.251	0.276	0.292	0.317	0.342	0.375	0.408	0.491	0.573	0.656
2.014	0.984	0.930	0.876	0.905	0.925	0.940	0.884	0.806	0.090	0.321	0.229	0.323
2.497	0.982	0.928	0.875	0.904	0.925	0.939	0.883	0.805	0.088	0.326	0.229	0.323
3.005	0.984	0.929	0.877	0.904	0.925	0.939	0.883	0.806	0.087	0.326	0.229	0.324
3.508	0.982	0.929	0.877	0.904	0.926	0.939	0.883	0.805	0.086	0.325	0.230	0.325
4.004	0.983	0.929	0.879	0.905	0.927	0.938	0.883	0.806	0.086	0.325	0.230	0.325
4.497	0.983	0.928	0.880	0.906	0.927	0.938	0.883	0.805	0.086	0.323	0.230	0.325
5.006	0.983	0.928	0.880	0.906	0.928	0.938	0.883	0.806	0.086	0.323	0.230	0.326
5.495	0.983	0.928	0.881	0.907	0.928	0.938	0.883	0.805	0.085	0.323	0.229	0.326
6.000	0.983	0.928	0.881	0.907	0.929	0.938	0.883	0.805	0.085	0.322	0.229	0.326
7.000	0.983	0.928	0.882	0.907	0.929	0.937	0.883	0.805	0.085	0.321	0.229	0.326
8.013	0.983	0.928	0.882	0.907	0.929	0.937	0.883	0.805	0.084	0.321	0.228	0.326
9.010	0.983	0.927	0.881	0.907	0.929	0.937	0.883	0.804	0.085	0.320	0.228	0.326
9.994	0.982	0.927	0.880	0.906	0.929	0.937	0.883	0.804	0.085	0.320	0.227	0.326
11.008	0.982	0.927	0.880	0.906	0.929	0.937	0.883	0.804	0.084	0.319	0.227	0.325
12.014	0.982	0.926	0.879	0.905	0.929	0.937	0.883	0.803	0.084	0.315	0.227	0.325

Table 21. Concluded

Sidewall: $z/(w/2) = 0.296$

NPR	$p/p_{t,j}$ at x/L of— 0.127	0.226	0.292	0.391
2.014	0.981	0.756	0.873	0.702
2.497	0.980	0.754	0.873	0.701
3.005	0.981	0.748	0.874	0.701
3.508	0.981	0.743	0.875	0.701
4.004	0.981	0.742	0.875	0.701
4.497	0.981	0.742	0.876	0.701
5.006	0.981	0.741	0.876	0.702
5.495	0.982	0.742	0.877	0.701
6.000	0.982	0.743	0.877	0.701
7.000	0.981	0.744	0.877	0.701
8.013	0.981	0.745	0.877	0.701
9.010	0.981	0.745	0.877	0.701
9.994	0.981	0.745	0.876	0.701
11.008	0.981	0.745	0.876	0.700
12.014	0.981	0.744	0.876	0.699

Sidewall: $z/(w/2) = 0.000$

NPR	$p/p_{t,j}$ at x/L of— 0.127	0.226	0.292	0.391	0.474	0.573	0.755	0.937
2.014	0.981	0.908	0.853	0.681	0.235	0.354	0.481	0.497
2.497	0.981	0.907	0.855	0.683	0.237	0.348	0.276	0.404
3.005	0.982	0.907	0.856	0.683	0.238	0.346	0.274	0.345
3.508	0.982	0.905	0.857	0.682	0.238	0.344	0.274	0.303
4.004	0.982	0.904	0.857	0.682	0.239	0.344	0.274	0.255
4.497	0.982	0.902	0.858	0.682	0.239	0.343	0.274	0.194
5.006	0.981	0.901	0.858	0.682	0.239	0.341	0.275	0.156
5.495	0.982	0.900	0.858	0.682	0.239	0.339	0.275	0.141
6.000	0.982	0.898	0.858	0.682	0.240	0.338	0.275	0.135
7.000	0.982	0.898	0.858	0.682	0.240	0.336	0.275	0.128
8.013	0.981	0.898	0.858	0.682	0.240	0.335	0.275	0.125
9.010	0.981	0.898	0.858	0.681	0.241	0.335	0.274	0.123
9.994	0.981	0.898	0.858	0.681	0.241	0.334	0.274	0.122
11.008	0.981	0.899	0.858	0.681	0.243	0.334	0.274	0.121
12.014	0.981	0.899	0.858	0.681	0.244	0.333	0.273	0.121

Sidewall: $z/(w/2) = -0.296$

NPR	$p/p_{t,j}$ at x/L of— 0.127	0.226	0.292	0.391
2.014	0.980	0.757	0.874	0.707
2.497	0.980	0.750	0.873	0.707
3.005	0.981	0.745	0.874	0.707
3.508	0.981	0.741	0.875	0.707
4.004	0.981	0.739	0.876	0.708
4.497	0.981	0.740	0.876	0.708
5.006	0.980	0.741	0.876	0.707
5.495	0.981	0.742	0.878	0.707
6.000	0.981	0.744	0.878	0.708
7.000	0.981	0.745	0.877	0.707
8.013	0.981	0.747	0.878	0.706
9.010	0.981	0.748	0.878	0.706
9.994	0.981	0.748	0.877	0.706
11.008	0.980	0.749	0.877	0.705
12.014	0.981	0.749	0.877	0.705

Table 22. Internal Static Pressure Ratios for SCF Nozzle Configuration 5

[Hexagonal geometry at dry power, $\delta_{v,p}$ = 0°, and $\delta_{v,y}$ = 10°]

$y/(w/2)$ = 0.074

	$p/p_{t,j}$ at x/L of—											
NPR	0.143	0.193	0.242	0.276	0.292	0.317	0.342	0.408	0.491	0.573	0.656	0.739
1.997	0.989	0.985	0.977	0.947	0.857	0.703	0.392	0.528	0.422	0.318	0.245	0.390
3.016	0.988	0.985	0.979	0.950	0.857	0.705	0.378	0.528	0.424	0.320	0.247	0.194
2.512	0.990	0.987	0.979	0.950	0.859	0.706	0.391	0.529	0.423	0.320	0.247	0.194
3.540	0.990	0.986	0.978	0.950	0.854	0.714	0.364	0.530	0.424	0.320	0.248	0.195
3.993	0.989	0.986	0.979	0.950	0.850	0.732	0.364	0.530	0.424	0.321	0.247	0.195
4.499	0.989	0.986	0.979	0.950	0.846	0.756	0.365	0.531	0.425	0.321	0.247	0.195
5.009	0.989	0.986	0.978	0.950	0.844	0.765	0.364	0.531	0.425	0.321	0.247	0.195
5.512	0.988	0.985	0.978	0.949	0.843	0.764	0.361	0.531	0.425	0.321	0.247	0.195
5.993	0.989	0.985	0.978	0.949	0.842	0.763	0.359	0.531	0.425	0.321	0.247	0.195
6.996	0.988	0.985	0.978	0.949	0.841	0.765	0.357	0.529	0.424	0.321	0.247	0.195
8.016	0.988	0.985	0.978	0.949	0.841	0.761	0.352	0.529	0.424	0.320	0.246	0.194
9.016	0.988	0.985	0.977	0.949	0.842	0.752	0.349	0.528	0.423	0.319	0.246	0.194
10.037	0.988	0.985	0.978	0.949	0.844	0.743	0.349	0.527	0.423	0.319	0.245	0.195
10.996	0.988	0.985	0.978	0.949	0.845	0.736	0.350	0.527	0.422	0.319	0.245	0.194
12.030	0.988	0.985	0.978	0.949	0.846	0.733	0.355	0.526	0.421	0.318	0.245	0.195

$y/(w/2)$ = 0.296

	$p/p_{t,j}$ at x/L of—
NPR	0.317
1.997	0.775
3.016	0.776
2.512	0.780
3.540	0.771
3.993	0.774
4.499	0.777
5.009	0.783
5.512	0.783
5.993	0.786
6.996	0.792
8.016	0.790
9.016	0.787
10.037	0.785
10.996	0.783
12.030	0.782

$y/(w/2)$ = 0.481

	$p/p_{t,j}$ at x/L of—										
NPR	0.143	0.193	0.242	0.276	0.292	0.317	0.342	0.375	0.408	0.573	0.838
1.997	0.984	0.983	0.968	0.781	0.825	0.759	0.807	0.161	0.489	0.295	0.492
3.016	0.986	0.983	0.968	0.770	0.820	0.769	0.822	0.155	0.480	0.297	0.282
2.512	0.986	0.984	0.969	0.777	0.825	0.766	0.810	0.159	0.483	0.296	0.376
3.540	0.987	0.983	0.969	0.760	0.812	0.775	0.836	0.150	0.477	0.297	0.223
3.993	0.986	0.983	0.969	0.754	0.807	0.777	0.843	0.148	0.474	0.297	0.216
4.499	0.986	0.984	0.968	0.742	0.795	0.787	0.846	0.146	0.470	0.297	0.215
5.009	0.986	0.983	0.968	0.725	0.788	0.797	0.848	0.143	0.467	0.297	0.215
5.512	0.987	0.983	0.968	0.713	0.784	0.803	0.849	0.140	0.465	0.297	0.215
5.993	0.987	0.983	0.968	0.714	0.786	0.800	0.852	0.139	0.462	0.297	0.215
6.996	0.986	0.983	0.968	0.722	0.794	0.794	0.851	0.139	0.460	0.296	0.215
8.016	0.986	0.983	0.968	0.729	0.797	0.789	0.850	0.139	0.458	0.296	0.215
9.016	0.986	0.982	0.968	0.734	0.800	0.785	0.848	0.138	0.458	0.295	0.215
10.037	0.986	0.983	0.968	0.739	0.803	0.781	0.847	0.138	0.458	0.295	0.215
10.996	0.986	0.983	0.968	0.743	0.804	0.778	0.845	0.139	0.458	0.295	0.215
12.030	0.986	0.983	0.968	0.746	0.806	0.777	0.842	0.140	0.459	0.294	0.214

Table 22. Continued

$y/(w/2) = 0.704$

NPR	$p/p_{t,j}$ at x/L of— 0.284	0.317	0.358
1.997	0.790	0.946	0.833
3.016	0.837	0.941	0.834
2.512	0.805	0.946	0.834
3.540	0.859	0.939	0.833
3.993	0.864	0.939	0.833
4.499	0.855	0.941	0.832
5.009	0.851	0.941	0.832
5.512	0.849	0.943	0.832
5.993	0.850	0.942	0.832
6.996	0.848	0.943	0.831
8.016	0.842	0.944	0.831
9.016	0.835	0.944	0.831
10.037	0.828	0.944	0.831
10.996	0.824	0.945	0.831
12.030	0.820	0.945	0.831

$y/(w/2) = 0.926$

NPR	$p/p_{t,j}$ at x/L of— 0.143	0.209	0.251	0.276	0.292	0.317	0.342	0.375	0.408	0.491	0.573	0.656
1.997	0.985	0.934	0.879	0.907	0.927	0.940	0.885	0.807	0.085	0.336	0.229	0.325
3.016	0.985	0.934	0.881	0.907	0.927	0.940	0.886	0.809	0.082	0.337	0.230	0.324
2.512	0.984	0.934	0.880	0.907	0.928	0.940	0.886	0.809	0.084	0.338	0.230	0.323
3.540	0.985	0.935	0.882	0.908	0.928	0.940	0.886	0.809	0.082	0.337	0.231	0.324
3.993	0.985	0.934	0.883	0.909	0.929	0.939	0.886	0.808	0.082	0.336	0.231	0.324
4.499	0.985	0.934	0.883	0.909	0.929	0.939	0.886	0.808	0.082	0.336	0.231	0.325
5.009	0.985	0.934	0.884	0.909	0.929	0.939	0.886	0.809	0.082	0.335	0.231	0.323
5.512	0.985	0.933	0.885	0.909	0.929	0.939	0.886	0.808	0.082	0.334	0.230	0.325
5.993	0.984	0.933	0.885	0.909	0.930	0.939	0.886	0.808	0.081	0.333	0.230	0.325
6.996	0.984	0.933	0.885	0.909	0.930	0.938	0.886	0.808	0.082	0.330	0.230	0.324
8.016	0.984	0.932	0.884	0.909	0.930	0.938	0.886	0.808	0.084	0.328	0.230	0.324
9.016	0.984	0.932	0.884	0.909	0.930	0.938	0.886	0.807	0.085	0.326	0.230	0.324
10.037	0.984	0.931	0.883	0.908	0.930	0.938	0.885	0.807	0.084	0.325	0.230	0.326
10.996	0.983	0.931	0.883	0.908	0.930	0.938	0.885	0.807	0.084	0.325	0.231	0.325
12.030	0.983	0.931	0.882	0.908	0.930	0.937	0.885	0.807	0.084	0.323	0.231	0.324

Table 22. Concluded

Sidewall: $z/(w/2) = 0.296$

NPR	$p/p_{t,j}$ at x/L of— 0.127	0.226	0.292	0.391
1.997	0.981	0.764	0.876	0.704
3.016	0.983	0.764	0.877	0.705
2.512	0.983	0.766	0.877	0.704
3.540	0.984	0.761	0.878	0.706
3.993	0.984	0.758	0.878	0.706
4.499	0.984	0.754	0.879	0.706
5.009	0.984	0.752	0.879	0.706
5.512	0.984	0.751	0.879	0.706
5.993	0.983	0.750	0.879	0.706
6.996	0.984	0.749	0.880	0.706
8.016	0.983	0.749	0.879	0.706
9.016	0.983	0.749	0.879	0.706
10.037	0.983	0.750	0.879	0.700
10.996	0.983	0.750	0.878	0.700
12.030	0.983	0.750	0.878	0.700

Sidewall: $z/(w/2) = 0.000$

NPR	$p/p_{t,j}$ at x/L of— 0.127	0.226	0.292	0.391	0.474	0.573	0.755	0.937
1.997	0.983	0.913	0.856	0.681	0.238	0.355	0.487	0.499
3.016	0.984	0.911	0.859	0.681	0.241	0.349	0.273	0.343
2.512	0.983	0.912	0.858	0.682	0.240	0.350	0.281	0.402
3.540	0.985	0.911	0.860	0.681	0.241	0.348	0.273	0.300
3.993	0.985	0.910	0.860	0.682	0.242	0.347	0.273	0.257
4.499	0.984	0.909	0.860	0.682	0.242	0.346	0.273	0.194
5.009	0.984	0.907	0.860	0.681	0.243	0.345	0.273	0.155
5.512	0.984	0.905	0.860	0.681	0.243	0.343	0.273	0.141
5.993	0.984	0.904	0.860	0.682	0.243	0.342	0.273	0.135
6.996	0.984	0.903	0.860	0.682	0.243	0.340	0.273	0.128
8.016	0.983	0.902	0.860	0.681	0.243	0.338	0.272	0.125
9.016	0.983	0.902	0.860	0.681	0.243	0.337	0.272	0.123
10.037	0.983	0.902	0.860	0.682	0.243	0.336	0.272	0.122
10.996	0.983	0.902	0.860	0.681	0.244	0.336	0.271	0.121
12.030	0.983	0.903	0.860	0.682	0.244	0.335	0.271	0.121

Sidewall: $z/(w/2) = -0.296$

NPR	$p/p_{t,j}$ at x/L of— 0.127	0.226	0.292	0.391
1.997	0.982	0.761	0.874	0.704
3.016	0.983	0.751	0.877	0.704
2.512	0.983	0.756	0.876	0.705
3.540	0.984	0.749	0.878	0.705
3.993	0.984	0.747	0.878	0.705
4.499	0.984	0.747	0.878	0.705
5.009	0.983	0.747	0.878	0.704
5.512	0.984	0.747	0.879	0.692
5.993	0.983	0.749	0.879	0.692
6.996	0.983	0.749	0.880	0.702
8.016	0.983	0.750	0.879	0.703
9.016	0.983	0.751	0.879	0.703
10.037	0.983	0.751	0.879	0.710
10.996	0.983	0.752	0.879	0.710
12.030	0.983	0.752	0.878	0.709

Table 23. Internal Static Pressure Ratios for SCF Nozzle Configuration 6

[Hexagonal geometry at dry power, $\delta_{v,p} = 0°$, and $\delta_{v,y} = 20°$]

$y/(w/2) = 0.074$

	$p/p_{t,j}$ at x/L of—											
NPR	0.143	0.193	0.242	0.276	0.292	0.317	0.342	0.408	0.491	0.573	0.656	0.739
1.990	0.993	0.991	0.983	0.954	0.865	0.712	0.394	0.531	0.425	0.323	0.249	0.396
2.506	0.993	0.991	0.983	0.955	0.862	0.716	0.392	0.529	0.425	0.323	0.249	0.196
2.991	0.991	0.989	0.982	0.953	0.859	0.736	0.383	0.528	0.424	0.322	0.248	0.196
3.492	0.992	0.989	0.981	0.952	0.853	0.764	0.373	0.527	0.424	0.322	0.248	0.196
4.002	0.990	0.988	0.981	0.952	0.847	0.788	0.368	0.528	0.424	0.322	0.248	0.196
4.510	0.990	0.988	0.980	0.951	0.844	0.787	0.364	0.529	0.424	0.322	0.248	0.195
4.995	0.990	0.987	0.979	0.950	0.843	0.783	0.359	0.529	0.424	0.322	0.247	0.195
5.493	0.989	0.987	0.979	0.950	0.842	0.771	0.355	0.529	0.424	0.322	0.247	0.195
5.981	0.989	0.986	0.978	0.949	0.842	0.767	0.356	0.529	0.424	0.322	0.247	0.195
7.007	0.989	0.986	0.978	0.950	0.841	0.769	0.357	0.528	0.423	0.321	0.247	0.194
8.008	0.988	0.985	0.978	0.949	0.841	0.763	0.352	0.527	0.422	0.320	0.247	0.193
8.968	0.988	0.985	0.978	0.949	0.842	0.756	0.351	0.526	0.422	0.320	0.246	0.193
10.012	0.988	0.986	0.978	0.949	0.843	0.748	0.353	0.525	0.421	0.319	0.246	0.193
10.389	0.988	0.985	0.978	0.949	0.843	0.744	0.354	0.525	0.421	0.319	0.246	0.193

$y/(w/2) = 0.296$

	$p/p_{t,j}$ at x/L of—
NPR	0.317
1.990	0.780
2.506	0.784
2.991	0.773
3.492	0.771
4.002	0.772
4.510	0.778
4.995	0.783
5.493	0.784
5.981	0.787
7.007	0.790
8.008	0.787
8.968	0.783
10.012	0.781
10.389	0.780

$y/(w/2) = 0.481$

	$p/p_{t,j}$ at x/L of—										
NPR	0.143	0.193	0.242	0.276	0.292	0.317	0.342	0.375	0.408	0.573	0.838
1.990	0.991	0.989	0.973	0.785	0.829	0.762	0.827	0.164	0.484	0.300	0.496
2.506	0.990	0.988	0.973	0.778	0.823	0.774	0.829	0.163	0.471	0.300	0.378
2.991	0.989	0.987	0.970	0.768	0.817	0.776	0.842	0.156	0.473	0.300	0.291
3.492	0.989	0.986	0.971	0.759	0.812	0.780	0.851	0.150	0.472	0.300	0.227
4.002	0.989	0.986	0.971	0.746	0.802	0.788	0.855	0.147	0.466	0.299	0.217
4.510	0.989	0.985	0.970	0.732	0.791	0.800	0.856	0.144	0.461	0.299	0.216
4.995	0.988	0.985	0.969	0.720	0.783	0.809	0.856	0.141	0.458	0.299	0.216
5.493	0.988	0.985	0.970	0.714	0.780	0.811	0.858	0.136	0.458	0.299	0.216
5.981	0.987	0.984	0.969	0.713	0.782	0.809	0.859	0.134	0.457	0.298	0.216
7.007	0.987	0.984	0.969	0.718	0.791	0.798	0.859	0.132	0.456	0.298	0.216
8.008	0.987	0.984	0.968	0.725	0.797	0.792	0.855	0.131	0.457	0.296	0.215
8.968	0.987	0.983	0.968	0.731	0.800	0.787	0.854	0.132	0.457	0.296	0.215
10.012	0.987	0.984	0.969	0.736	0.803	0.784	0.851	0.133	0.457	0.295	0.214
10.389	0.987	0.983	0.968	0.738	0.804	0.783	0.850	0.134	0.457	0.295	0.214

Table 23. Continued

$y/(w/2) = 0.704$

NPR	$p/p_{t,j}$ at x/L of— 0.284	0.317	0.358
1.990	0.827	0.947	0.837
2.506	0.847	0.941	0.837
2.991	0.886	0.936	0.836
3.492	0.894	0.935	0.834
4.002	0.887	0.937	0.834
4.510	0.877	0.938	0.833
4.995	0.871	0.939	0.833
5.493	0.871	0.940	0.832
5.981	0.870	0.940	0.832
7.007	0.866	0.941	0.832
8.008	0.860	0.941	0.832
8.968	0.857	0.941	0.831
10.012	0.854	0.941	0.831
10.389	0.854	0.941	0.831

$y/(w/2) = 0.926$

NPR	$p/p_{t,j}$ at x/L of— 0.143	0.209	0.251	0.276	0.292	0.317	0.342	0.375	0.408	0.491	0.573	0.656
1.990	0.990	0.944	0.886	0.914	0.934	0.949	0.892	0.817	0.088	0.337	0.239	0.329
2.506	0.989	0.942	0.886	0.912	0.933	0.948	0.891	0.817	0.085	0.337	0.238	0.328
2.991	0.988	0.941	0.887	0.912	0.932	0.947	0.890	0.815	0.084	0.335	0.238	0.328
3.492	0.988	0.941	0.887	0.912	0.932	0.945	0.889	0.814	0.084	0.334	0.238	0.328
4.002	0.987	0.939	0.887	0.912	0.932	0.944	0.889	0.814	0.084	0.332	0.238	0.328
4.510	0.987	0.939	0.887	0.912	0.932	0.944	0.888	0.812	0.083	0.331	0.238	0.328
4.995	0.986	0.937	0.887	0.912	0.932	0.942	0.888	0.812	0.083	0.330	0.238	0.328
5.493	0.986	0.937	0.888	0.912	0.932	0.943	0.888	0.812	0.083	0.329	0.238	0.328
5.981	0.986	0.937	0.888	0.912	0.932	0.942	0.888	0.812	0.083	0.328	0.238	0.328
7.007	0.986	0.936	0.887	0.912	0.932	0.942	0.888	0.812	0.082	0.328	0.236	0.328
8.008	0.985	0.936	0.887	0.911	0.932	0.941	0.887	0.810	0.082	0.327	0.235	0.327
8.968	0.985	0.935	0.886	0.911	0.932	0.941	0.888	0.811	0.082	0.326	0.234	0.327
10.012	0.985	0.935	0.886	0.910	0.932	0.941	0.888	0.811	0.082	0.325	0.234	0.327
10.389	0.985	0.935	0.886	0.910	0.932	0.941	0.888	0.810	0.082	0.325	0.234	0.327

Table 23. Concluded

Sidewall: $z/(w/2) = 0.296$

NPR	$p/p_{t,j}$ at x/L of— 0.127	0.226	0.292	0.391
1.990	0.990	0.775	0.882	0.694
2.506	0.989	0.773	0.883	0.693
2.991	0.988	0.772	0.882	0.693
3.492	0.987	0.768	0.882	0.689
4.002	0.987	0.766	0.883	0.688
4.510	0.986	0.762	0.882	0.685
4.995	0.986	0.759	0.882	0.686
5.493	0.986	0.758	0.882	0.685
5.981	0.986	0.758	0.882	0.685
7.007	0.985	0.757	0.882	0.686
8.008	0.985	0.756	0.882	0.686
8.968	0.985	0.757	0.881	0.689
10.012	0.985	0.757	0.881	0.688
10.389	0.985	0.757	0.881	0.689

Sidewall: $z/(w/2) = 0.000$

NPR	$p/p_{t,j}$ at x/L of— 0.127	0.226	0.292	0.391	0.474	0.573	0.755	0.937
1.990	0.991	0.919	0.865	0.684	0.242	0.361	0.486	0.505
2.506	0.990	0.918	0.865	0.685	0.243	0.356	0.276	0.405
2.991	0.990	0.917	0.865	0.683	0.244	0.353	0.275	0.347
3.492	0.989	0.916	0.865	0.683	0.244	0.351	0.275	0.304
4.002	0.989	0.914	0.865	0.683	0.244	0.350	0.275	0.255
4.510	0.988	0.913	0.864	0.683	0.244	0.348	0.274	0.192
4.995	0.987	0.912	0.864	0.683	0.244	0.347	0.274	0.156
5.493	0.987	0.910	0.864	0.682	0.244	0.346	0.274	0.142
5.981	0.986	0.909	0.863	0.682	0.244	0.345	0.274	0.135
7.007	0.986	0.908	0.864	0.682	0.245	0.343	0.274	0.128
8.008	0.986	0.907	0.863	0.681	0.246	0.342	0.273	0.126
8.968	0.985	0.907	0.863	0.681	0.246	0.341	0.273	0.124
10.012	0.985	0.907	0.863	0.681	0.246	0.340	0.272	0.122
10.389	0.985	0.907	0.863	0.681	0.246	0.339	0.272	0.122

Sidewall: $z/(w/2) = -0.296$

NPR	$p/p_{t,j}$ at x/L of— 0.127	0.226	0.292	0.391
1.990	0.988	0.771	0.884	0.713
2.506	0.988	0.765	0.882	0.711
2.991	0.986	0.761	0.882	0.711
3.492	0.986	0.758	0.881	0.710
4.002	0.987	0.756	0.882	0.711
4.510	0.985	0.757	0.882	0.710
4.995	0.985	0.756	0.882	0.710
5.493	0.985	0.757	0.882	0.710
5.981	0.985	0.757	0.882	0.710
7.007	0.985	0.758	0.882	0.710
8.008	0.984	0.759	0.882	0.709
8.968	0.985	0.759	0.882	0.708
10.012	0.985	0.760	0.882	0.708
10.389	0.984	0.760	0.882	0.708

Table 24. Internal Static Pressure Ratios for SCF Nozzle Configuration 7

[Hexagonal geometry at dry power, $\delta_{v,p}$ = 10°, and $\delta_{v,y}$ = 0°]

$y/(w/2)$ = 0.074

	$p/p_{t,j}$ at x/L of—											
NPR	0.143	0.193	0.242	0.276	0.292	0.325	0.350	0.424	0.491	0.573	0.656	0.739
1.985	0.986	0.986	0.976	0.950	0.855	0.649	0.393	0.496	0.447	0.379	0.320	0.489
2.500	0.986	0.986	0.976	0.949	0.854	0.643	0.392	0.494	0.444	0.377	0.319	0.329
2.993	0.987	0.986	0.976	0.949	0.854	0.641	0.391	0.493	0.442	0.375	0.319	0.322
3.507	0.986	0.985	0.976	0.949	0.850	0.670	0.396	0.492	0.439	0.366	0.323	0.315
3.995	0.986	0.986	0.976	0.948	0.849	0.673	0.386	0.491	0.437	0.366	0.322	0.308
4.494	0.986	0.986	0.975	0.949	0.847	0.681	0.379	0.491	0.436	0.365	0.321	0.305
4.993	0.986	0.985	0.976	0.948	0.846	0.690	0.378	0.492	0.436	0.364	0.320	0.300
5.497	0.986	0.985	0.975	0.947	0.845	0.692	0.379	0.492	0.437	0.370	0.316	0.296
5.994	0.986	0.984	0.975	0.947	0.845	0.693	0.375	0.492	0.435	0.370	0.316	0.291
6.998	0.986	0.985	0.975	0.947	0.845	0.678	0.374	0.489	0.432	0.369	0.318	0.286
7.995	0.986	0.984	0.975	0.946	0.844	0.683	0.365	0.490	0.432	0.367	0.317	0.283
9.004	0.986	0.984	0.974	0.945	0.843	0.686	0.367	0.488	0.431	0.367	0.313	0.282
9.986	0.986	0.984	0.974	0.945	0.843	0.684	0.369	0.488	0.431	0.366	0.312	0.280
10.979	0.986	0.983	0.974	0.945	0.843	0.679	0.368	0.487	0.430	0.366	0.311	0.278
11.996	0.986	0.984	0.974	0.945	0.844	0.670	0.371	0.487	0.429	0.365	0.310	0.275

$y/(w/2)$ = 0.296

	$p/p_{t,j}$ at x/L of—
NPR	0.325
1.985	0.754
2.500	0.758
2.993	0.761
3.507	0.755
3.995	0.747
4.494	0.745
4.993	0.757
5.497	0.764
5.994	0.764
6.998	0.759
7.995	0.757
9.004	0.758
9.986	0.761
10.979	0.761
11.996	0.759

$y/(w/2)$ = 0.481

	$p/p_{t,j}$ at x/L of—										
NPR	0.143	0.193	0.242	0.276	0.292	0.325	0.342	0.391	0.424	0.573	0.838
1.985	0.986	0.983	0.968	0.771	0.787	0.771	0.814	0.186	0.474	0.388	0.789
2.500	0.985	0.982	0.968	0.769	0.789	0.769	0.811	0.187	0.471	0.388	0.627
2.993	0.985	0.983	0.966	0.758	0.781	0.789	0.811	0.193	0.463	0.387	0.523
3.507	0.985	0.982	0.967	0.745	0.765	0.821	0.819	0.193	0.457	0.384	0.446
3.995	0.985	0.983	0.967	0.736	0.761	0.831	0.821	0.189	0.456	0.382	0.391
4.494	0.987	0.982	0.966	0.731	0.760	0.833	0.820	0.187	0.456	0.380	0.348
4.993	0.986	0.982	0.967	0.728	0.760	0.833	0.820	0.184	0.456	0.380	0.313
5.497	0.985	0.982	0.967	0.724	0.756	0.838	0.822	0.180	0.457	0.380	0.284
5.994	0.985	0.982	0.966	0.720	0.749	0.846	0.826	0.177	0.455	0.380	0.260
6.998	0.985	0.982	0.966	0.714	0.743	0.855	0.836	0.173	0.450	0.381	0.223
7.995	0.985	0.982	0.966	0.705	0.736	0.869	0.835	0.174	0.440	0.381	0.195
9.004	0.985	0.982	0.965	0.703	0.733	0.870	0.833	0.176	0.432	0.377	0.173
9.986	0.985	0.982	0.965	0.708	0.736	0.861	0.833	0.178	0.432	0.377	0.155
10.979	0.985	0.982	0.965	0.715	0.741	0.849	0.832	0.181	0.435	0.376	0.141
11.996	0.985	0.982	0.965	0.720	0.746	0.839	0.830	0.183	0.437	0.374	0.129

Table 24. Continued

$y/(w/2) = 0.704$

NPR	$p/p_{t,j}$ at x/L of— 0.284	0.325	0.358
1.985	0.844	0.898	0.803
2.500	0.840	0.898	0.803
2.993	0.845	0.897	0.801
3.507	0.832	0.895	0.802
3.995	0.832	0.892	0.801
4.494	0.839	0.890	0.800
4.993	0.842	0.890	0.799
5.497	0.849	0.891	0.797
5.994	0.854	0.891	0.796
6.998	0.871	0.891	0.793
7.995	0.874	0.890	0.791
9.004	0.875	0.888	0.790
9.986	0.874	0.888	0.790
10.979	0.868	0.891	0.790
11.996	0.858	0.894	0.791

$y/(w/2) = 0.926$

NPR	$p/p_{t,j}$ at x/L of— 0.143	0.209	0.251	0.276	0.292	0.325	0.342	0.375	0.424	0.491	0.573	0.656
1.985	0.985	0.936	0.873	0.891	0.913	0.904	0.867	0.794	0.147	0.291	0.417	0.421
2.500	0.985	0.936	0.872	0.892	0.912	0.905	0.867	0.793	0.145	0.292	0.413	0.398
2.993	0.985	0.936	0.872	0.891	0.912	0.905	0.866	0.792	0.144	0.294	0.410	0.393
3.507	0.984	0.935	0.871	0.888	0.910	0.904	0.867	0.791	0.144	0.292	0.410	0.390
3.995	0.984	0.935	0.871	0.888	0.909	0.904	0.866	0.790	0.137	0.289	0.409	0.393
4.494	0.984	0.935	0.870	0.888	0.909	0.903	0.865	0.789	0.133	0.284	0.411	0.390
4.993	0.984	0.934	0.871	0.888	0.910	0.904	0.866	0.789	0.132	0.283	0.410	0.389
5.497	0.984	0.934	0.871	0.889	0.910	0.904	0.865	0.788	0.134	0.283	0.408	0.391
5.994	0.984	0.934	0.871	0.889	0.910	0.903	0.865	0.786	0.121	0.290	0.406	0.390
6.998	0.984	0.933	0.872	0.890	0.911	0.903	0.864	0.785	0.116	0.297	0.403	0.385
7.995	0.984	0.933	0.873	0.890	0.912	0.903	0.863	0.785	0.111	0.296	0.400	0.383
9.004	0.983	0.932	0.871	0.890	0.910	0.902	0.862	0.784	0.107	0.288	0.400	0.379
9.986	0.983	0.932	0.870	0.890	0.910	0.902	0.862	0.783	0.107	0.289	0.399	0.378
10.979	0.983	0.931	0.870	0.889	0.909	0.902	0.862	0.783	0.107	0.289	0.398	0.375
11.996	0.983	0.931	0.869	0.888	0.909	0.901	0.862	0.784	0.107	0.281	0.395	0.373

Table 24. Concluded

Sidewall: $z/(w/2) = 0.296$

NPR	$p/p_{t,j}$ at x/L of— 0.127	0.226	0.292	0.391
1.985	0.984	0.773	0.872	0.713
2.500	0.983	0.762	0.874	0.712
2.993	0.983	0.758	0.873	0.713
3.507	0.983	0.755	0.873	0.713
3.995	0.983	0.754	0.873	0.713
4.494	0.983	0.753	0.872	0.712
4.993	0.983	0.753	0.873	0.713
5.497	0.983	0.753	0.873	0.712
5.994	0.983	0.753	0.873	0.711
6.998	0.983	0.754	0.874	0.711
7.995	0.983	0.755	0.874	0.711
9.004	0.982	0.755	0.873	0.709
9.986	0.982	0.756	0.873	0.709
10.979	0.982	0.756	0.872	0.709
11.996	0.982	0.756	0.872	0.711

Sidewall: $z/(w/2) = 0.000$

NPR	$p/p_{t,j}$ at x/L of— 0.127	0.226	0.292	0.391	0.474	0.573	0.755	0.937
1.985	0.986	0.919	0.872	0.680	0.432	0.395	0.504	0.504
2.500	0.984	0.918	0.873	0.680	0.431	0.392	0.400	0.400
2.993	0.984	0.916	0.873	0.681	0.431	0.390	0.335	0.332
3.507	0.984	0.916	0.872	0.680	0.430	0.389	0.289	0.284
3.995	0.984	0.915	0.872	0.680	0.430	0.388	0.257	0.249
4.494	0.984	0.913	0.871	0.681	0.429	0.383	0.233	0.224
4.993	0.983	0.912	0.872	0.680	0.429	0.378	0.215	0.204
5.497	0.984	0.910	0.871	0.680	0.429	0.375	0.200	0.185
5.994	0.983	0.909	0.872	0.680	0.428	0.375	0.189	0.170
6.998	0.984	0.909	0.872	0.679	0.427	0.364	0.172	0.146
7.995	0.983	0.909	0.872	0.680	0.425	0.363	0.161	0.130
9.004	0.982	0.908	0.871	0.679	0.424	0.369	0.152	0.118
9.986	0.982	0.908	0.871	0.679	0.423	0.350	0.148	0.110
10.979	0.982	0.909	0.871	0.679	0.421	0.353	0.143	0.104
11.996	0.982	0.910	0.871	0.680	0.421	0.341	0.139	0.099

Sidewall: $z/(w/2) = -0.296$

NPR	$p/p_{t,j}$ at x/L of— 0.127	0.226	0.292	0.391
1.985	0.984	0.813	0.907	0.702
2.500	0.984	0.809	0.907	0.715
2.993	0.983	0.805	0.907	0.681
3.507	0.983	0.800	0.907	0.653
3.995	0.984	0.799	0.907	0.717
4.494	0.983	0.798	0.907	0.755
4.993	0.984	0.797	0.907	0.752
5.497	0.983	0.797	0.908	0.750
5.994	0.983	0.797	0.907	0.714
6.998	0.983	0.798	0.907	0.767
7.995	0.983	0.799	0.907	0.648
9.004	0.982	0.799	0.906	0.675
9.986	0.982	0.800	0.906	0.659
10.979	0.982	0.800	0.906	0.634
11.996	0.982	0.800	0.906	0.756

Table 25. Internal Static Pressure Ratios for SCF Nozzle Configuration 8

[Hexagonal geometry at dry power, $\delta_{v,p}$ = 10°, and $\delta_{v,y}$ = 10°]

$y/(w/2)$ = 0.074

	$p/p_{t,j}$ at x/L of—											
NPR	0.143	0.193	0.242	0.276	0.292	0.325	0.350	0.424	0.491	0.573	0.656	0.739
1.989	0.990	0.988	0.977	0.952	0.856	0.659	0.395	0.498	0.449	0.378	0.323	0.478
2.510	0.989	0.988	0.977	0.952	0.857	0.656	0.395	0.496	0.447	0.376	0.322	0.333
2.991	0.989	0.987	0.977	0.951	0.857	0.652	0.394	0.494	0.445	0.374	0.322	0.325
3.488	0.989	0.987	0.977	0.951	0.855	0.651	0.392	0.492	0.443	0.372	0.322	0.319
4.000	0.988	0.987	0.977	0.951	0.855	0.645	0.381	0.491	0.441	0.372	0.321	0.313
4.485	0.988	0.987	0.977	0.950	0.853	0.644	0.379	0.490	0.439	0.372	0.321	0.307
5.013	0.988	0.986	0.977	0.950	0.851	0.649	0.386	0.490	0.437	0.371	0.321	0.302
5.505	0.988	0.986	0.976	0.949	0.850	0.657	0.392	0.489	0.436	0.370	0.320	0.298
5.989	0.988	0.986	0.976	0.949	0.849	0.670	0.396	0.489	0.437	0.371	0.316	0.295
7.004	0.987	0.985	0.976	0.948	0.847	0.680	0.386	0.489	0.436	0.370	0.314	0.289
7.994	0.987	0.985	0.975	0.947	0.845	0.680	0.369	0.489	0.435	0.370	0.312	0.284
8.996	0.987	0.985	0.975	0.947	0.844	0.683	0.371	0.489	0.434	0.368	0.314	0.281
9.976	0.987	0.985	0.975	0.947	0.844	0.679	0.373	0.489	0.434	0.368	0.313	0.279
10.986	0.987	0.985	0.975	0.947	0.845	0.675	0.373	0.488	0.433	0.366	0.313	0.277
11.971	0.987	0.984	0.975	0.947	0.845	0.668	0.374	0.487	0.432	0.365	0.313	0.276

$y/(w/2)$ = 0.296

	$p/p_{t,j}$ at x/L of—
NPR	0.325
1.989	0.749
2.510	0.757
2.991	0.763
3.488	0.763
4.000	0.758
4.485	0.753
5.013	0.758
5.505	0.762
5.989	0.763
7.004	0.760
7.994	0.760
8.996	0.762
9.976	0.764
10.986	0.763
11.971	0.761

$y/(w/2)$ = 0.481

	$p/p_{t,j}$ at x/L of—										
NPR	0.143	0.193	0.242	0.276	0.292	0.325	0.342	0.391	0.424	0.573	0.838
1.989	0.987	0.986	0.969	0.769	0.785	0.763	0.815	0.186	0.473	0.392	0.789
2.510	0.986	0.986	0.969	0.767	0.789	0.761	0.806	0.187	0.471	0.393	0.626
2.991	0.986	0.984	0.968	0.765	0.792	0.762	0.800	0.189	0.470	0.393	0.525
3.488	0.986	0.984	0.969	0.761	0.793	0.764	0.800	0.188	0.470	0.393	0.450
4.000	0.986	0.984	0.969	0.757	0.791	0.768	0.798	0.189	0.468	0.392	0.392
4.485	0.986	0.984	0.968	0.747	0.782	0.791	0.799	0.198	0.460	0.391	0.350
5.013	0.986	0.983	0.968	0.736	0.775	0.811	0.807	0.195	0.455	0.389	0.313
5.505	0.986	0.983	0.967	0.728	0.765	0.823	0.814	0.186	0.455	0.388	0.285
5.989	0.985	0.982	0.967	0.721	0.754	0.836	0.822	0.180	0.455	0.387	0.262
7.004	0.985	0.983	0.967	0.718	0.748	0.839	0.832	0.176	0.452	0.384	0.224
7.994	0.985	0.982	0.966	0.711	0.743	0.850	0.836	0.176	0.441	0.381	0.196
8.996	0.985	0.982	0.966	0.709	0.741	0.855	0.835	0.177	0.432	0.383	0.174
9.976	0.985	0.982	0.966	0.713	0.744	0.849	0.834	0.179	0.431	0.382	0.157
10.986	0.985	0.982	0.966	0.721	0.748	0.837	0.832	0.182	0.433	0.382	0.142
11.971	0.985	0.982	0.966	0.726	0.751	0.829	0.829	0.185	0.434	0.381	0.130

Table 25. Continued

$y/(w/2) = 0.704$

NPR	$p/p_{t,j}$ at x/L of— 0.284	0.325	0.358
1.989	0.824	0.903	0.804
2.510	0.826	0.902	0.804
2.991	0.827	0.902	0.802
3.488	0.833	0.901	0.801
4.000	0.831	0.901	0.799
4.485	0.816	0.902	0.801
5.013	0.822	0.896	0.801
5.505	0.834	0.891	0.799
5.989	0.841	0.890	0.797
7.004	0.861	0.892	0.794
7.994	0.869	0.891	0.791
8.996	0.871	0.890	0.791
9.976	0.870	0.890	0.790
10.986	0.860	0.893	0.791
11.971	0.846	0.896	0.791

$y/(w/2) = 0.926$

NPR	$p/p_{t,j}$ at x/L of— 0.143	0.209	0.251	0.276	0.292	0.325	0.342	0.375	0.424	0.491	0.573	0.656
1.989	0.985	0.934	0.872	0.893	0.915	0.908	0.865	0.792	0.147	0.288	0.415	0.411
2.510	0.984	0.933	0.872	0.894	0.914	0.908	0.865	0.791	0.145	0.290	0.414	0.408
2.991	0.985	0.933	0.872	0.893	0.914	0.906	0.864	0.789	0.144	0.290	0.413	0.406
3.488	0.984	0.932	0.871	0.892	0.913	0.905	0.863	0.789	0.143	0.290	0.412	0.405
4.000	0.984	0.932	0.870	0.891	0.913	0.905	0.863	0.788	0.144	0.290	0.411	0.404
4.485	0.984	0.932	0.870	0.891	0.911	0.904	0.863	0.788	0.144	0.288	0.410	0.403
5.013	0.983	0.932	0.869	0.890	0.910	0.903	0.863	0.787	0.144	0.284	0.409	0.402
5.505	0.983	0.931	0.871	0.890	0.911	0.904	0.863	0.787	0.142	0.280	0.409	0.401
5.989	0.983	0.931	0.870	0.890	0.910	0.903	0.862	0.786	0.140	0.275	0.408	0.401
7.004	0.983	0.930	0.872	0.891	0.911	0.903	0.861	0.785	0.138	0.270	0.405	0.399
7.994	0.982	0.930	0.872	0.892	0.912	0.902	0.861	0.783	0.135	0.265	0.403	0.398
8.996	0.982	0.929	0.872	0.892	0.912	0.902	0.860	0.782	0.138	0.271	0.399	0.394
9.976	0.982	0.929	0.872	0.891	0.912	0.901	0.860	0.782	0.138	0.272	0.398	0.391
10.986	0.982	0.928	0.871	0.891	0.911	0.901	0.860	0.782	0.146	0.277	0.396	0.390
11.971	0.982	0.928	0.870	0.890	0.911	0.900	0.859	0.781	0.141	0.276	0.396	0.394

Table 25. Concluded

Sidewall: $z/(w/2) = 0.296$

NPR	$p/p_{t,j}$ at x/L of— 0.127	0.226	0.292	0.391
1.989	0.982	0.763	0.872	0.713
2.510	0.982	0.759	0.872	0.712
2.991	0.982	0.757	0.872	0.713
3.488	0.981	0.754	0.872	0.712
4.000	0.982	0.749	0.871	0.712
4.485	0.981	0.745	0.871	0.712
5.013	0.981	0.743	0.871	0.712
5.505	0.981	0.742	0.871	0.712
5.989	0.981	0.742	0.871	0.711
7.004	0.981	0.743	0.872	0.711
7.994	0.980	0.744	0.872	0.711
8.996	0.980	0.745	0.872	0.710
9.976	0.980	0.746	0.871	0.711
10.986	0.980	0.746	0.871	0.711
11.971	0.980	0.745	0.870	0.711

Sidewall: $z/(w/2) = 0.000$

NPR	$p/p_{t,j}$ at x/L of— 0.127	0.226	0.292	0.391	0.474	0.573	0.755	0.937
1.989	0.982	0.915	0.871	0.678	0.431	0.397	0.502	0.502
2.510	0.982	0.915	0.872	0.680	0.430	0.390	0.399	0.399
2.991	0.982	0.913	0.872	0.680	0.430	0.383	0.335	0.333
3.488	0.982	0.912	0.871	0.680	0.429	0.379	0.290	0.286
4.000	0.982	0.911	0.871	0.679	0.428	0.373	0.257	0.249
4.485	0.982	0.909	0.870	0.679	0.428	0.369	0.232	0.227
5.013	0.981	0.908	0.870	0.679	0.428	0.365	0.213	0.205
5.505	0.982	0.906	0.870	0.678	0.428	0.360	0.199	0.186
5.989	0.981	0.904	0.869	0.678	0.427	0.350	0.188	0.170
7.004	0.981	0.904	0.870	0.678	0.427	0.328	0.170	0.146
7.994	0.980	0.903	0.870	0.677	0.427	0.311	0.158	0.130
8.996	0.980	0.903	0.869	0.677	0.426	0.299	0.150	0.119
9.976	0.980	0.904	0.870	0.677	0.427	0.287	0.143	0.110
10.986	0.980	0.905	0.870	0.676	0.426	0.278	0.139	0.104
11.971	0.980	0.905	0.869	0.676	0.425	0.269	0.136	0.099

Sidewall: $z/(w/2) = -0.296$

NPR	$p/p_{t,j}$ at x/L of— 0.127	0.226	0.292	0.391
1.989	0.983	0.808	0.906	0.680
2.510	0.983	0.805	0.907	0.680
2.991	0.982	0.799	0.906	0.679
3.488	0.982	0.791	0.906	0.678
4.000	0.982	0.789	0.906	0.677
4.485	0.981	0.788	0.906	0.679
5.013	0.982	0.788	0.906	0.680
5.505	0.982	0.788	0.905	0.682
5.989	0.981	0.788	0.905	0.682
7.004	0.981	0.790	0.905	0.683
7.994	0.981	0.791	0.904	0.680
8.996	0.980	0.792	0.904	0.679
9.976	0.980	0.793	0.904	0.674
10.986	0.980	0.793	0.904	0.647
11.971	0.980	0.794	0.903	0.643

Table 26. Internal Static Pressure Ratios for SCF Nozzle Configuration 9

[Hexagonal geometry at dry power, $\delta_{v,p}$ = 10°, and $\delta_{v,y}$ = 20°]

$y/(w/2)$ = 0.074

	$p/p_{t,j}$ at x/L of—											
NPR	0.143	0.193	0.242	0.276	0.292	0.325	0.350	0.424	0.491	0.573	0.656	0.739
2.015	0.990	0.988	0.979	0.952	0.858	0.648	0.397	0.496	0.450	0.373	0.321	0.465
2.497	0.989	0.988	0.978	0.952	0.859	0.645	0.399	0.494	0.446	0.374	0.318	0.328
3.003	0.989	0.987	0.978	0.952	0.858	0.645	0.398	0.493	0.445	0.373	0.317	0.322
3.522	0.988	0.987	0.978	0.952	0.858	0.635	0.399	0.492	0.444	0.372	0.316	0.316
4.015	0.989	0.988	0.978	0.952	0.858	0.636	0.398	0.491	0.442	0.372	0.315	0.312
4.508	0.989	0.987	0.977	0.951	0.856	0.650	0.400	0.489	0.442	0.372	0.314	0.306
5.016	0.988	0.987	0.977	0.950	0.853	0.670	0.403	0.490	0.441	0.372	0.314	0.301
5.520	0.988	0.987	0.976	0.950	0.852	0.676	0.401	0.490	0.440	0.371	0.314	0.298
6.008	0.989	0.987	0.977	0.949	0.850	0.683	0.391	0.490	0.438	0.369	0.313	0.295
7.007	0.988	0.986	0.977	0.949	0.848	0.688	0.371	0.489	0.436	0.369	0.312	0.289
9.000	0.988	0.986	0.976	0.948	0.845	0.686	0.367	0.490	0.433	0.367	0.309	0.282
10.042	0.988	0.985	0.976	0.948	0.844	0.687	0.366	0.489	0.432	0.367	0.308	0.280
11.055	0.988	0.985	0.976	0.948	0.844	0.683	0.368	0.488	0.432	0.366	0.308	0.278
11.593	0.988	0.986	0.976	0.948	0.844	0.680	0.371	0.488	0.432	0.366	0.308	0.277

$y/(w/2)$ = 0.296

	$p/p_{t,j}$ at x/L of—
NPR	0.325
2.015	0.749
2.497	0.752
3.003	0.757
3.522	0.762
4.015	0.763
4.508	0.769
5.016	0.774
5.520	0.774
6.008	0.772
7.007	0.763
9.000	0.765
10.042	0.765
11.055	0.769
11.593	0.768

$y/(w/2)$ = 0.481

	$p/p_{t,j}$ at x/L of—										
NPR	0.143	0.193	0.242	0.276	0.292	0.325	0.342	0.391	0.424	0.573	0.838
2.015	0.986	0.985	0.968	0.770	0.781	0.762	0.818	0.209	0.498	0.510	0.508
2.497	0.986	0.986	0.969	0.767	0.786	0.763	0.810	0.218	0.501	0.411	0.411
3.003	0.985	0.985	0.968	0.766	0.789	0.764	0.803	0.228	0.475	0.342	0.339
3.522	0.986	0.984	0.968	0.763	0.791	0.766	0.802	0.235	0.473	0.388	0.317
4.015	0.986	0.985	0.969	0.759	0.789	0.770	0.805	0.237	0.472	0.385	0.313
4.508	0.985	0.983	0.968	0.755	0.790	0.772	0.806	0.241	0.472	0.387	0.312
5.016	0.986	0.983	0.968	0.750	0.789	0.776	0.801	0.247	0.469	0.386	0.311
5.520	0.986	0.983	0.967	0.743	0.782	0.791	0.805	0.250	0.460	0.385	0.310
6.008	0.986	0.983	0.967	0.739	0.780	0.793	0.808	0.248	0.463	0.384	0.310
7.007	0.985	0.983	0.967	0.727	0.758	0.816	0.830	0.243	0.461	0.382	0.309
9.000	0.985	0.982	0.966	0.706	0.738	0.860	0.834	0.238	0.445	0.379	0.302
10.042	0.986	0.983	0.966	0.708	0.742	0.853	0.832	0.238	0.443	0.377	0.297
11.055	0.986	0.982	0.966	0.715	0.747	0.839	0.831	0.183	0.420	0.377	0.288
11.593	0.986	0.982	0.966	0.718	0.749	0.833	0.830	0.184	0.421	0.376	0.282

Table 26. Continued

$y/(w/2) = 0.704$

NPR	$p/p_{t,j}$ at x/L of— 0.284	0.325	0.358
2.015	0.816	0.896	0.799
2.497	0.824	0.895	0.800
3.003	0.827	0.832	0.800
3.522	0.844	0.857	0.802
4.015	0.864	0.833	0.802
4.508	0.879	0.868	0.802
5.016	0.867	0.885	0.802
5.520	0.847	0.876	0.801
6.008	0.851	0.891	0.800
7.007	0.866	0.892	0.799
9.000	0.868	0.890	0.797
10.042	0.864	0.890	0.797
11.055	0.856	0.892	0.797
11.593	0.849	0.894	0.798

$y/(w/2) = 0.926$

NPR	$p/p_{t,j}$ at x/L of— 0.143	0.209	0.251	0.276	0.292	0.325	0.342	0.375	0.424	0.491	0.573	0.656
2.015	0.984	0.932	0.865	0.899	0.525	0.903	0.863	0.792	0.182	0.291	0.418	0.417
2.497	0.983	0.930	0.865	0.898	0.727	0.903	0.864	0.792	0.177	0.287	0.418	0.409
3.003	0.982	0.929	0.864	0.896	0.740	0.902	0.863	0.791	0.173	0.284	0.417	0.407
3.522	0.983	0.930	0.864	0.894	0.804	0.900	0.863	0.789	0.172	0.282	0.418	0.403
4.015	0.983	0.930	0.864	0.893	0.796	0.900	0.862	0.789	0.170	0.280	0.416	0.401
4.508	0.983	0.929	0.864	0.892	0.838	0.900	0.861	0.788	0.167	0.278	0.415	0.402
5.016	0.982	0.928	0.864	0.892	0.871	0.899	0.862	0.787	0.165	0.277	0.413	0.402
5.520	0.982	0.928	0.864	0.891	0.873	0.900	0.861	0.787	0.162	0.277	0.412	0.401
6.008	0.982	0.928	0.865	0.891	0.900	0.900	0.861	0.786	0.157	0.275	0.410	0.384
7.007	0.981	0.927	0.865	0.891	0.860	0.900	0.860	0.785	0.150	0.274	0.408	0.388
9.000	0.981	0.927	0.866	0.891	0.913	0.898	0.859	0.784	0.135	0.273	0.404	0.374
10.042	0.981	0.926	0.866	0.890	0.907	0.898	0.859	0.783	0.129	0.271	0.402	0.373
11.055	0.981	0.926	0.865	0.889	0.896	0.897	0.859	0.783	0.118	0.273	0.400	0.371
11.593	0.980	0.926	0.864	0.888	0.895	0.898	0.859	0.783	0.118	0.273	0.399	0.370

Table 26. Concluded

Sidewall: $z/(w/2) = 0.296$

NPR	$p/p_{t,j}$ at x/L of— 0.127	0.226	0.292	0.391
2.015	0.978	0.755	0.870	0.711
2.497	0.979	0.751	0.870	0.711
3.003	0.979	0.745	0.869	0.711
3.522	0.978	0.738	0.869	0.710
4.015	0.978	0.732	0.869	0.710
4.508	0.977	0.730	0.869	0.710
5.016	0.978	0.729	0.869	0.710
5.520	0.978	0.729	0.870	0.710
6.008	0.978	0.729	0.869	0.709
7.007	0.977	0.730	0.869	0.709
9.000	0.977	0.732	0.870	0.709
10.042	0.977	0.733	0.870	0.709
11.055	0.977	0.734	0.869	0.709
11.593	0.976	0.733	0.869	0.709

Sidewall: $z/(w/2) = 0.000$

NPR	$p/p_{t,j}$ at x/L of— 0.127	0.226	0.292	0.391	0.474	0.573	0.755	0.937
2.015	0.981	0.911	0.867	0.679	0.427	0.394	0.494	0.494
2.497	0.979	0.909	0.870	0.680	0.427	0.387	0.400	0.399
3.003	0.979	0.909	0.871	0.680	0.427	0.382	0.334	0.331
3.522	0.979	0.908	0.870	0.678	0.426	0.378	0.288	0.282
4.015	0.979	0.907	0.870	0.679	0.426	0.373	0.256	0.248
4.508	0.979	0.905	0.869	0.678	0.426	0.367	0.232	0.225
5.016	0.978	0.903	0.868	0.679	0.425	0.361	0.214	0.203
5.520	0.978	0.901	0.868	0.678	0.425	0.359	0.200	0.183
6.008	0.978	0.900	0.868	0.678	0.425	0.352	0.189	0.168
7.007	0.977	0.898	0.868	0.677	0.426	0.336	0.172	0.146
9.000	0.977	0.897	0.868	0.676	0.424	0.321	0.154	0.118
10.042	0.976	0.897	0.868	0.676	0.422	0.313	0.148	0.109
11.055	0.976	0.898	0.868	0.675	0.422	0.296	0.145	0.103
11.593	0.976	0.899	0.868	0.675	0.421	0.294	0.143	0.100

Sidewall: $z/(w/2) = -0.296$

NPR	$p/p_{t,j}$ at x/L of— 0.127	0.226	0.292	0.391
2.015	0.979	0.793	0.905	0.523
2.497	0.979	0.789	0.904	0.424
3.003	0.979	0.786	0.904	0.352
3.522	0.979	0.782	0.904	0.300
4.015	0.980	0.780	0.904	0.263
4.508	0.978	0.778	0.904	0.236
5.016	0.978	0.777	0.904	0.211
5.520	0.978	0.777	0.904	0.192
6.008	0.978	0.777	0.904	0.176
7.007	0.978	0.778	0.902	0.151
9.000	0.977	0.782	0.903	0.118
10.042	0.977	0.784	0.903	0.106
11.055	0.977	0.785	0.903	0.096
11.593	0.977	0.785	0.903	0.092

Table 27. Internal Static Pressure Ratios for SCF Nozzle Configuration 10

[Hexagonal geometry at afterburning power, $\delta_{v,p} = 0°$, and $\delta_{v,y} = 0°$]

$y/(w/2) = 0.074$

	$p/p_{t,j}$ at x/L of—											
NPR	0.143	0.193	0.234	0.259	0.276	0.300	0.325	0.408	0.491	0.573	0.656	0.739
2.004	0.920	0.875	0.630	0.228	0.319	0.387	0.426	0.430	0.310	0.256	0.473	0.524
2.496	0.919	0.875	0.633	0.227	0.319	0.384	0.428	0.389	0.311	0.257	0.257	0.405
2.983	0.918	0.876	0.639	0.225	0.324	0.382	0.430	0.352	0.312	0.257	0.258	0.232
3.505	0.918	0.876	0.655	0.223	0.329	0.381	0.434	0.342	0.313	0.258	0.258	0.231
4.001	0.918	0.875	0.664	0.222	0.329	0.381	0.435	0.338	0.313	0.258	0.258	0.231
4.487	0.917	0.874	0.666	0.227	0.329	0.380	0.437	0.339	0.314	0.259	0.258	0.231
5.000	0.917	0.875	0.668	0.227	0.326	0.381	0.437	0.336	0.314	0.258	0.258	0.231
5.497	0.917	0.874	0.668	0.229	0.324	0.379	0.436	0.336	0.314	0.258	0.258	0.231
5.994	0.917	0.874	0.669	0.233	0.322	0.377	0.435	0.336	0.314	0.258	0.257	0.231
6.209	0.916	0.873	0.670	0.232	0.321	0.377	0.435	0.336	0.314	0.258	0.257	0.231

$y/(w/2) = 0.296$

	$p/p_{t,j}$ at x/L of—	
NPR	0.193	0.242
2.004	0.861	0.681
2.496	0.861	0.682
2.983	0.862	0.687
3.505	0.861	0.693
4.001	0.861	0.691
4.487	0.860	0.681
5.000	0.860	0.684
5.497	0.860	0.684
5.994	0.859	0.682
6.209	0.859	0.683

$y/(w/2) = 0.481$

	$p/p_{t,j}$ at x/L of—									
NPR	0.143	0.209	0.234	0.259	0.276	0.300	0.325	0.408	0.573	0.739
2.004	0.906	0.711	0.666	0.623	0.577	0.207	0.249	0.380	0.315	0.509
2.496	0.907	0.712	0.667	0.628	0.578	0.208	0.249	0.380	0.310	0.386
2.983	0.906	0.712	0.669	0.628	0.578	0.208	0.248	0.381	0.311	0.277
3.505	0.907	0.713	0.670	0.630	0.578	0.208	0.247	0.381	0.311	0.215
4.001	0.907	0.714	0.671	0.632	0.579	0.209	0.247	0.381	0.311	0.204
4.487	0.906	0.709	0.683	0.646	0.577	0.205	0.242	0.382	0.311	0.200
5.000	0.906	0.716	0.675	0.639	0.581	0.207	0.245	0.382	0.311	0.198
5.497	0.906	0.716	0.677	0.642	0.582	0.207	0.244	0.382	0.311	0.197
5.994	0.905	0.715	0.682	0.648	0.582	0.205	0.242	0.381	0.311	0.196
6.209	0.905	0.715	0.682	0.649	0.583	0.205	0.242	0.381	0.311	0.196

Table 27. Continued

$y/(w/2) = 0.704$

NPR	$p/p_{t,j}$ at x/L of— 0.209	0.242	0.276	0.309
2.004	0.630	0.859	0.808	0.105
2.496	0.633	0.853	0.808	0.104
2.983	0.635	0.849	0.809	0.105
3.505	0.637	0.847	0.809	0.105
4.001	0.640	0.847	0.809	0.104
4.487	0.646	0.810	0.813	0.106
5.000	0.645	0.841	0.808	0.104
5.497	0.648	0.836	0.808	0.104
5.994	0.650	0.818	0.810	0.105
6.209	0.651	0.817	0.810	0.105

$y/(w/2) = 0.926$

NPR	$p/p_{t,j}$ at x/L of— 0.143	0.185	0.209	0.242	0.276	0.300	0.325	0.358	0.408	0.491	0.573	0.656
2.004	0.608	0.780	0.807	0.882	0.799	0.711	0.088	0.111	0.197	0.396	0.479	0.482
2.496	0.609	0.782	0.808	0.878	0.799	0.711	0.088	0.110	0.197	0.395	0.387	0.390
2.983	0.610	0.783	0.807	0.877	0.799	0.711	0.087	0.110	0.196	0.395	0.328	0.318
3.505	0.612	0.783	0.807	0.877	0.800	0.712	0.086	0.110	0.195	0.396	0.303	0.267
4.001	0.612	0.783	0.807	0.875	0.800	0.711	0.085	0.110	0.195	0.397	0.292	0.240
4.487	0.608	0.771	0.805	0.884	0.806	0.713	0.085	0.110	0.195	0.398	0.286	0.221
5.000	0.600	0.789	0.806	0.872	0.801	0.711	0.085	0.110	0.193	0.397	0.282	0.206
5.497	0.600	0.789	0.805	0.872	0.801	0.711	0.085	0.110	0.193	0.397	0.280	0.195
5.994	0.615	0.786	0.808	0.871	0.802	0.711	0.085	0.110	0.192	0.398	0.278	0.188
6.209	0.614	0.786	0.808	0.871	0.802	0.711	0.085	0.110	0.192	0.399	0.278	0.185

Table 27. Concluded

Sidewall: $z/(w/2) = 0.296$

NPR	$p/p_{t,j}$ at x/L of— 0.127	0.226	0.292	0.391
2.004	0.920	0.369	0.587	0.430
2.496	0.921	0.357	0.598	0.430
2.983	0.921	0.355	0.595	0.430
3.505	0.920	0.358	0.578	0.431
4.001	0.920	0.341	0.601	0.429
4.487	0.920	0.332	0.607	0.429
5.000	0.920	0.329	0.603	0.428
5.497	0.919	0.323	0.599	0.428
5.994	0.920	0.314	0.595	0.428
6.209	0.919	0.311	0.597	0.427

Sidewall: $z/(w/2) = 0.000$

NPR	$p/p_{t,j}$ at x/L of— 0.127	0.226	0.292	0.391	0.474	0.573	0.755	0.937
2.004	0.922	0.752	0.484	0.468	0.319	0.359	0.508	0.510
2.496	0.921	0.750	0.480	0.469	0.318	0.192	0.429	0.407
2.983	0.922	0.749	0.479	0.471	0.318	0.193	0.274	0.373
3.505	0.922	0.750	0.480	0.471	0.317	0.193	0.242	0.301
4.001	0.922	0.749	0.479	0.470	0.317	0.193	0.241	0.267
4.487	0.921	0.748	0.479	0.470	0.317	0.194	0.241	0.228
5.000	0.921	0.748	0.482	0.470	0.316	0.194	0.241	0.176
5.497	0.921	0.747	0.483	0.469	0.315	0.194	0.241	0.144
5.994	0.921	0.748	0.483	0.469	0.315	0.194	0.241	0.131
6.209	0.921	0.747	0.483	0.469	0.315	0.193	0.241	0.128

Sidewall: $z/(w/2) = -0.296$

NPR	$p/p_{t,j}$ at x/L of— 0.127	0.226	0.292	0.391
2.004	0.918	0.381	0.564	0.435
2.496	0.919	0.344	0.589	0.431
2.983	0.919	0.325	0.596	0.430
3.505	0.920	0.310	0.600	0.429
4.001	0.919	0.305	0.603	0.430
4.487	0.919	0.307	0.603	0.431
5.000	0.919	0.308	0.603	0.431
5.497	0.919	0.309	0.601	0.431
5.994	0.919	0.312	0.596	0.432
6.209	0.918	0.314	0.591	0.432

Table 28. Internal Static Pressure Ratios for SCF Nozzle Configuration 11

[Hexagonal geometry at afterburning power, $\delta_{v,p} = 0°$, and $\delta_{v,y} = 10°$]

$y/(w/2) = 0.074$

	$p/p_{t,j}$ at x/L of—											
NPR	0.143	0.193	0.234	0.259	0.276	0.300	0.325	0.408	0.491	0.573	0.656	0.739
2.018	0.921	0.876	0.630	0.220	0.322	0.387	0.424	0.425	0.310	0.257	0.468	0.523
2.494	0.920	0.876	0.631	0.214	0.323	0.386	0.425	0.389	0.311	0.257	0.255	0.405
3.007	0.919	0.876	0.644	0.217	0.325	0.385	0.427	0.352	0.312	0.258	0.256	0.233
3.515	0.919	0.876	0.662	0.215	0.329	0.387	0.429	0.342	0.311	0.259	0.256	0.231
4.009	0.919	0.876	0.670	0.219	0.326	0.387	0.432	0.339	0.311	0.259	0.256	0.231
4.512	0.919	0.876	0.672	0.220	0.324	0.386	0.433	0.337	0.312	0.259	0.255	0.231
5.007	0.918	0.876	0.670	0.221	0.323	0.385	0.433	0.337	0.313	0.259	0.255	0.231
5.507	0.918	0.875	0.676	0.222	0.321	0.383	0.433	0.336	0.313	0.259	0.255	0.231
6.013	0.917	0.875	0.676	0.220	0.319	0.381	0.432	0.336	0.313	0.259	0.255	0.231
6.199	0.918	0.875	0.676	0.219	0.319	0.380	0.431	0.336	0.313	0.259	0.254	0.231

$y/(w/2) = 0.296$

	$p/p_{t,j}$ at x/L of—	
NPR	0.193	0.242
2.018	0.863	0.684
2.494	0.864	0.686
3.007	0.864	0.686
3.515	0.864	0.692
4.009	0.864	0.686
4.512	0.864	0.682
5.007	0.863	0.683
5.507	0.863	0.686
6.013	0.863	0.687
6.199	0.862	0.688

$y/(w/2) = 0.481$

	$p/p_{t,j}$ at x/L of—									
NPR	0.143	0.209	0.234	0.259	0.276	0.300	0.325	0.408	0.573	0.739
2.018	0.909	0.710	0.662	0.638	0.605	0.199	0.248	0.387	0.310	0.508
2.494	0.910	0.711	0.663	0.638	0.605	0.201	0.249	0.388	0.309	0.384
3.007	0.909	0.711	0.665	0.641	0.608	0.200	0.249	0.390	0.309	0.274
3.515	0.910	0.719	0.672	0.637	0.592	0.203	0.249	0.389	0.310	0.212
4.009	0.910	0.719	0.674	0.642	0.593	0.203	0.248	0.390	0.310	0.200
4.512	0.910	0.719	0.677	0.645	0.594	0.203	0.247	0.390	0.310	0.196
5.007	0.911	0.720	0.678	0.648	0.594	0.202	0.246	0.391	0.311	0.193
5.507	0.910	0.723	0.678	0.648	0.595	0.201	0.245	0.391	0.311	0.192
6.013	0.910	0.723	0.680	0.650	0.595	0.201	0.245	0.391	0.311	0.191
6.199	0.909	0.723	0.681	0.651	0.595	0.200	0.245	0.391	0.310	0.191

Table 28. Continued

$y/(w/2) = 0.704$

NPR	$p/p_{t,j}$ at x/L of— 0.209	0.242	0.276	0.309
2.018	0.683	0.896	0.801	0.105
2.494	0.686	0.898	0.800	0.105
3.007	0.694	0.896	0.799	0.105
3.515	0.677	0.889	0.801	0.103
4.009	0.680	0.888	0.800	0.103
4.512	0.682	0.888	0.800	0.102
5.007	0.682	0.887	0.800	0.102
5.507	0.683	0.887	0.800	0.102
6.013	0.684	0.885	0.800	0.103
6.199	0.684	0.884	0.800	0.102

$y/(w/2) = 0.926$

NPR	$p/p_{t,j}$ at x/L of— 0.143	0.185	0.209	0.242	0.276	0.300	0.325	0.358	0.408	0.491	0.573	0.656
2.018	0.648	0.794	0.815	0.869	0.806	0.722	0.090	0.115	0.202	0.401	0.473	0.479
2.494	0.645	0.794	0.816	0.877	0.807	0.721	0.088	0.115	0.202	0.402	0.386	0.390
3.007	0.644	0.794	0.814	0.883	0.810	0.722	0.088	0.114	0.202	0.403	0.326	0.312
3.515	0.669	0.793	0.818	0.889	0.812	0.724	0.088	0.114	0.201	0.405	0.303	0.266
4.009	0.670	0.793	0.819	0.888	0.812	0.724	0.088	0.115	0.200	0.406	0.293	0.239
4.512	0.670	0.794	0.816	0.885	0.812	0.724	0.088	0.115	0.200	0.406	0.287	0.220
5.007	0.670	0.795	0.816	0.882	0.812	0.723	0.087	0.115	0.199	0.406	0.283	0.206
5.507	0.670	0.796	0.816	0.878	0.812	0.724	0.087	0.115	0.198	0.407	0.281	0.196
6.013	0.671	0.796	0.816	0.876	0.812	0.724	0.087	0.115	0.197	0.408	0.279	0.188
6.199	0.673	0.795	0.816	0.876	0.812	0.723	0.087	0.115	0.197	0.408	0.279	0.185

Table 28. Concluded

Sidewall: $z/(w/2) = 0.296$

NPR	$p/p_{t,j}$ at x/L of— 0.127	0.226	0.292	0.391
2.018	0.930	0.391	0.605	0.437
2.494	0.931	0.387	0.607	0.437
3.007	0.931	0.386	0.607	0.436
3.515	0.930	0.388	0.603	0.437
4.009	0.930	0.393	0.595	0.437
4.512	0.931	0.395	0.591	0.437
5.007	0.931	0.385	0.594	0.436
5.507	0.931	0.372	0.600	0.436
6.013	0.930	0.364	0.602	0.435
6.199	0.930	0.361	0.603	0.435

Sidewall: $z/(w/2) = 0.000$

NPR	$p/p_{t,j}$ at x/L of— 0.127	0.226	0.292	0.391	0.474	0.573	0.755	0.937
2.018	0.932	0.762	0.500	0.474	0.321	0.352	0.502	0.505
2.494	0.932	0.762	0.499	0.473	0.320	0.194	0.425	0.407
3.007	0.933	0.762	0.501	0.474	0.319	0.195	0.259	0.368
3.515	0.932	0.760	0.503	0.473	0.318	0.195	0.242	0.301
4.009	0.932	0.760	0.506	0.473	0.318	0.195	0.241	0.268
4.512	0.932	0.759	0.507	0.472	0.318	0.196	0.241	0.230
5.007	0.933	0.760	0.508	0.473	0.317	0.196	0.241	0.178
5.507	0.932	0.759	0.507	0.473	0.317	0.196	0.242	0.144
6.013	0.932	0.758	0.508	0.473	0.317	0.196	0.242	0.130
6.199	0.932	0.759	0.507	0.473	0.316	0.196	0.242	0.128

Sidewall: $z/(w/2) = -0.296$

NPR	$p/p_{t,j}$ at x/L of— 0.127	0.226	0.292	0.391
2.018	0.930	0.406	0.578	0.442
2.494	0.930	0.406	0.576	0.444
3.007	0.930	0.411	0.575	0.444
3.515	0.930	0.423	0.571	0.444
4.009	0.930	0.424	0.572	0.444
4.512	0.930	0.373	0.582	0.443
5.007	0.930	0.327	0.584	0.441
5.507	0.929	0.315	0.589	0.440
6.013	0.929	0.312	0.588	0.440
6.199	0.929	0.313	0.587	0.440

Table 29. Internal Static Pressure Ratios for SCF Nozzle Configuration 12

[Hexagonal geometry at afterburning power, $\delta_{v,p} = 0°$, and $\delta_{v,y} = 20°$]

$y/(w/2) = 0.074$

	$p/p_{t,j}$ at x/L of—											
NPR	0.143	0.193	0.234	0.259	0.276	0.300	0.325	0.408	0.491	0.573	0.656	0.739
2.015	0.922	0.875	0.627	0.203	0.334	0.396	0.424	0.373	0.308	0.257	0.461	0.521
2.503	0.923	0.878	0.628	0.204	0.334	0.397	0.426	0.375	0.310	0.258	0.246	0.399
3.017	0.921	0.878	0.627	0.207	0.332	0.396	0.428	0.376	0.311	0.258	0.247	0.232
3.533	0.920	0.877	0.628	0.209	0.331	0.393	0.429	0.377	0.310	0.258	0.246	0.231
4.005	0.921	0.877	0.631	0.209	0.331	0.387	0.430	0.377	0.311	0.258	0.246	0.230
4.492	0.920	0.875	0.637	0.209	0.329	0.385	0.430	0.377	0.311	0.258	0.246	0.230
5.016	0.919	0.876	0.641	0.209	0.322	0.386	0.431	0.377	0.310	0.257	0.247	0.230

$y/(w/2) = 0.296$

	$p/p_{t,j}$ at x/L of—	
NPR	0.193	0.242
2.015	0.865	0.686
2.503	0.865	0.683
3.017	0.865	0.680
3.533	0.864	0.679
4.005	0.864	0.679
4.492	0.864	0.683
5.016	0.863	0.685

$y/(w/2) = 0.481$

	$p/p_{t,j}$ at x/L of—									
NPR	0.143	0.209	0.234	0.259	0.276	0.300	0.325	0.408	0.573	0.739
2.015	0.912	0.717	0.668	0.650	0.626	0.188	0.244	0.392	0.309	0.510
2.503	0.914	0.721	0.670	0.652	0.626	0.186	0.246	0.393	0.308	0.374
3.017	0.913	0.721	0.674	0.653	0.625	0.187	0.246	0.394	0.308	0.274
3.533	0.913	0.722	0.677	0.656	0.626	0.187	0.246	0.395	0.308	0.208
4.005	0.913	0.723	0.679	0.659	0.625	0.188	0.245	0.395	0.308	0.196
4.492	0.912	0.723	0.681	0.660	0.623	0.188	0.245	0.395	0.308	0.191
5.016	0.913	0.725	0.683	0.662	0.622	0.188	0.244	0.396	0.308	0.189

Table 29. Continued

$y/(w/2) = 0.704$

NPR	$p/p_{t,j}$ at x/L of— 0.209	0.242	0.276	0.309
2.015	0.746	0.908	0.794	0.102
2.503	0.753	0.906	0.795	0.103
3.017	0.755	0.905	0.794	0.103
3.533	0.758	0.904	0.792	0.102
4.005	0.759	0.902	0.792	0.102
4.492	0.757	0.900	0.791	0.103
5.016	0.754	0.899	0.791	0.103

$y/(w/2) = 0.926$

NPR	$p/p_{t,j}$ at x/L of— 0.143	0.185	0.209	0.242	0.276	0.300	0.325	0.358	0.408	0.491	0.573	0.656
2.015	0.670	0.806	0.824	0.873	0.818	0.735	0.093	0.117	0.202	0.405	0.472	0.481
2.503	0.673	0.809	0.826	0.876	0.821	0.736	0.091	0.116	0.202	0.406	0.383	0.388
3.017	0.672	0.810	0.827	0.880	0.823	0.736	0.091	0.116	0.201	0.408	0.324	0.308
3.533	0.673	0.810	0.829	0.882	0.823	0.736	0.090	0.115	0.201	0.409	0.301	0.264
4.005	0.671	0.810	0.829	0.886	0.824	0.736	0.089	0.115	0.201	0.410	0.291	0.239
4.492	0.671	0.810	0.829	0.887	0.824	0.736	0.089	0.115	0.200	0.410	0.285	0.222
5.016	0.670	0.811	0.829	0.889	0.824	0.735	0.089	0.115	0.199	0.411	0.282	0.207

Table 29. Concluded

Sidewall: $z/(w/2) = 0.296$

NPR	$p/p_{t,j}$ at x/L of— 0.127	0.226	0.292	0.391
2.015	0.938	0.406	0.620	0.442
2.503	0.938	0.402	0.623	0.443
3.017	0.938	0.400	0.623	0.442
3.533	0.940	0.405	0.617	0.442
4.005	0.939	0.409	0.611	0.442
4.492	0.939	0.404	0.610	0.441
5.016	0.938	0.389	0.613	0.440

Sidewall: $z/(w/2) = 0.000$

NPR	$p/p_{t,j}$ at x/L of— 0.127	0.226	0.292	0.391	0.474	0.573	0.755	0.937
2.015	0.940	0.772	0.517	0.479	0.322	0.350	0.501	0.505
2.503	0.942	0.773	0.515	0.478	0.322	0.196	0.419	0.406
3.017	0.940	0.772	0.515	0.479	0.322	0.197	0.253	0.362
3.533	0.940	0.770	0.519	0.478	0.321	0.197	0.241	0.299
4.005	0.940	0.770	0.521	0.478	0.320	0.197	0.241	0.269
4.492	0.940	0.768	0.524	0.477	0.320	0.197	0.241	0.231
5.016	0.940	0.768	0.526	0.477	0.319	0.197	0.242	0.175

Sidewall: $z/(w/2) = -0.296$

NPR	$p/p_{t,j}$ at x/L of— 0.127	0.226	0.292	0.391
2.015	0.938	0.420	0.594	0.448
2.503	0.938	0.410	0.596	0.446
3.017	0.939	0.333	0.610	0.442
3.533	0.938	0.319	0.613	0.442
4.005	0.938	0.320	0.615	0.443
4.492	0.937	0.334	0.617	0.444
5.016	0.938	0.358	0.620	0.445

Table 30. Internal Static Pressure Ratios for SCF Nozzle Configuration 13

[Hexagonal geometry at afterburning power, $\delta_{v,p}$ = 10°, and $\delta_{v,y}$ = 0°]

$y/(w/2)$ = 0.074

	$p/p_{t,j}$ at x/L of—										
NPR	0.143	0.193	0.242	0.276	0.304	0.329	0.350	0.424	0.491	0.573	0.656
2.006	0.901	0.798	0.170	0.375	0.444	0.455	0.437	0.404	0.455	0.495	0.507
2.493	0.901	0.797	0.165	0.340	0.408	0.429	0.412	0.358	0.321	0.405	0.417
2.996	0.900	0.796	0.167	0.335	0.408	0.433	0.415	0.359	0.322	0.396	0.388
3.503	0.900	0.795	0.169	0.333	0.407	0.435	0.417	0.359	0.323	0.394	0.378
3.998	0.900	0.794	0.172	0.330	0.405	0.437	0.419	0.360	0.323	0.394	0.374
4.497	0.900	0.793	0.173	0.330	0.402	0.438	0.420	0.360	0.323	0.392	0.372
5.012	0.899	0.791	0.170	0.329	0.398	0.438	0.420	0.360	0.323	0.391	0.371
5.496	0.899	0.790	0.165	0.330	0.394	0.438	0.421	0.360	0.323	0.390	0.371
6.002	0.898	0.788	0.161	0.331	0.391	0.437	0.422	0.361	0.323	0.389	0.371
6.173	0.898	0.788	0.160	0.330	0.391	0.437	0.422	0.361	0.324	0.388	0.371

$y/(w/2)$ = 0.296

	$p/p_{t,j}$ at x/L of—
NPR	0.329
2.006	0.412
2.493	0.384
2.996	0.384
3.503	0.385
3.998	0.386
4.497	0.386
5.012	0.387
5.496	0.386
6.002	0.386
6.173	0.385

$y/(w/2)$ = 0.481

	$p/p_{t,j}$ at x/L of—										
NPR	0.143	0.193	0.242	0.284	0.304	0.329	0.350	0.391	0.424	0.573	0.739
2.006	0.887	0.732	0.622	0.214	0.289	0.331	0.373	0.416	0.421	0.504	0.503
2.493	0.887	0.732	0.627	0.178	0.227	0.264	0.389	0.389	0.361	0.381	0.401
2.996	0.886	0.731	0.632	0.178	0.227	0.263	0.387	0.390	0.362	0.371	0.351
3.503	0.886	0.731	0.638	0.178	0.226	0.261	0.385	0.389	0.362	0.369	0.331
3.998	0.886	0.731	0.643	0.177	0.225	0.259	0.383	0.390	0.363	0.368	0.319
4.497	0.885	0.731	0.648	0.177	0.224	0.258	0.381	0.390	0.363	0.368	0.313
5.012	0.885	0.733	0.653	0.176	0.222	0.257	0.379	0.389	0.364	0.368	0.308
5.496	0.885	0.735	0.656	0.175	0.221	0.256	0.376	0.389	0.364	0.368	0.306
6.002	0.885	0.738	0.658	0.173	0.219	0.256	0.375	0.389	0.364	0.368	0.304
6.173	0.884	0.739	0.659	0.174	0.219	0.255	0.374	0.389	0.364	0.368	0.304

Table 30. Continued

$y/(w/2) = 0.704$

NPR	$p/p_{t,j}$ at x/L of— 0.284	0.329	0.358
2.006	0.659	0.294	0.301
2.493	0.657	0.168	0.213
2.996	0.657	0.170	0.213
3.503	0.657	0.171	0.212
3.998	0.657	0.172	0.212
4.497	0.657	0.172	0.211
5.012	0.656	0.172	0.210
5.496	0.656	0.172	0.210
6.002	0.656	0.172	0.210
6.173	0.655	0.172	0.209

$y/(w/2) = 0.926$

NPR	$p/p_{t,j}$ at x/L of— 0.143	0.193	0.242	0.267	0.292	0.329/	0.358	0.375	0.424	0.491	0.557	0.623
2.006	0.602	0.831	0.871	0.795	0.684	0.330	0.316	0.321	0.354	0.426	0.475	0.487
2.493	0.607	0.833	0.872	0.795	0.684	0.103	0.119	0.141	0.323	0.432	0.390	0.398
2.996	0.614	0.834	0.872	0.795	0.684	0.101	0.119	0.141	0.321	0.420	0.348	0.347
3.503	0.619	0.835	0.871	0.794	0.683	0.100	0.119	0.141	0.319	0.417	0.322	0.313
3.998	0.625	0.835	0.872	0.794	0.683	0.100	0.120	0.141	0.323	0.417	0.307	0.292
4.497	0.629	0.836	0.872	0.794	0.683	0.099	0.121	0.141	0.333	0.417	0.296	0.278
5.012	0.632	0.836	0.872	0.794	0.682	0.098	0.121	0.141	0.320	0.417	0.289	0.267
5.496	0.635	0.836	0.871	0.793	0.682	0.098	0.121	0.140	0.312	0.416	0.284	0.259
6.002	0.636	0.836	0.871	0.793	0.681	0.098	0.120	0.140	0.309	0.416	0.281	0.253
6.173	0.637	0.836	0.871	0.793	0.682	0.098	0.120	0.140	0.309	0.416	0.280	0.251

Table 30. Concluded

Sidewall: $z/(w/2) = 0.296$

	$p/p_{t,j}$ at x/L of—			
NPR	0.127	0.226	0.292	0.391
2.006	0.919	0.385	0.630	0.560
2.493	0.921	0.377	0.630	0.559
2.996	0.920	0.376	0.623	0.561
3.503	0.920	0.360	0.609	0.561
3.998	0.921	0.337	0.604	0.561
4.497	0.921	0.322	0.603	0.561
5.012	0.921	0.316	0.604	0.561
5.496	0.920	0.311	0.605	0.560
6.002	0.921	0.305	0.606	0.559
6.173	0.920	0.304	0.606	0.560

Sidewall: $z/(w/2) = 0.000$

	$p/p_{t,j}$ at x/L of—							
NPR	0.127	0.226	0.292	0.391	0.474	0.573	0.755	0.937
2.006	0.921	0.755	0.494	0.537	0.467	0.443	0.508	0.492
2.493	0.922	0.753	0.492	0.535	0.453	0.368	0.383	0.395
2.996	0.922	0.753	0.495	0.536	0.452	0.369	0.331	0.365
3.503	0.921	0.752	0.495	0.535	0.451	0.368	0.308	0.278
3.998	0.921	0.751	0.494	0.538	0.451	0.368	0.298	0.221
4.497	0.921	0.750	0.496	0.538	0.450	0.368	0.293	0.197
5.012	0.921	0.750	0.498	0.536	0.449	0.368	0.290	0.183
5.496	0.921	0.750	0.499	0.537	0.449	0.368	0.288	0.173
6.002	0.920	0.749	0.499	0.536	0.448	0.368	0.287	0.167
6.173	0.920	0.749	0.499	0.536	0.448	0.368	0.287	0.166

Sidewall: $z/(w/2) = -0.296$

	$p/p_{t,j}$ at x/L of—			
NPR	0.127	0.226	0.292	0.391
2.006	0.915	0.400	0.514	0.505
2.493	0.916	0.385	0.529	0.496
2.996	0.917	0.394	0.522	0.498
3.503	0.916	0.389	0.523	0.498
3.998	0.917	0.389	0.526	0.499
4.497	0.916	0.388	0.529	0.499
5.012	0.917	0.383	0.530	0.498
5.496	0.916	0.380	0.533	0.498
6.002	0.916	0.375	0.536	0.497
6.173	0.916	0.374	0.536	0.497

Table 31. Internal Static Pressure Ratios for SCF Nozzle Configuration 14

[Hexagonal geometry at afterburning power, $\delta_{v,p}$ = 10°, and $\delta_{v,y}$ = 10°]

$y/(w/2)$ = 0.074

	$p/p_{t,j}$ at x/L of—										
NPR	0.143	0.193	0.242	0.276	0.304	0.329	0.350	0.424	0.491	0.573	0.656
2.004	0.900	0.796	0.181	0.377	0.449	0.458	0.442	0.410	0.459	0.496	0.507
2.503	0.899	0.796	0.176	0.335	0.411	0.432	0.415	0.359	0.323	0.402	0.413
2.995	0.900	0.796	0.171	0.335	0.410	0.434	0.416	0.359	0.324	0.393	0.386
3.493	0.898	0.794	0.166	0.336	0.409	0.436	0.418	0.359	0.323	0.392	0.376
3.995	0.899	0.793	0.164	0.336	0.405	0.437	0.420	0.359	0.324	0.391	0.372
4.499	0.899	0.792	0.163	0.334	0.401	0.438	0.421	0.359	0.324	0.390	0.371
5.008	0.898	0.791	0.166	0.331	0.401	0.439	0.422	0.360	0.324	0.388	0.369
5.495	0.898	0.789	0.168	0.330	0.397	0.439	0.423	0.360	0.323	0.386	0.370
5.982	0.897	0.788	0.168	0.328	0.392	0.439	0.423	0.361	0.323	0.385	0.369
6.181	0.897	0.788	0.168	0.328	0.391	0.439	0.423	0.361	0.323	0.384	0.369

$y/(w/2)$ = 0.296

	$p/p_{t,j}$ at x/L of—
NPR	0.329
2.004	0.416
2.503	0.388
2.995	0.390
3.493	0.391
3.995	0.391
4.499	0.391
5.008	0.393
5.495	0.393
5.982	0.392
6.181	0.392

$y/(w/2)$ = 0.481

	$p/p_{t,j}$ at x/L of—										
NPR	0.143	0.193	0.242	0.284	0.304	0.329	0.350	0.391	0.424	0.573	0.739
2.004	0.884	0.722	0.620	0.223	0.292	0.336	0.375	0.412	0.419	0.504	0.503
2.503	0.884	0.722	0.625	0.184	0.227	0.259	0.379	0.380	0.355	0.387	0.401
2.995	0.883	0.722	0.632	0.184	0.227	0.257	0.377	0.380	0.356	0.376	0.349
3.493	0.882	0.718	0.640	0.183	0.226	0.255	0.374	0.379	0.355	0.373	0.328
3.995	0.883	0.715	0.647	0.182	0.224	0.253	0.371	0.379	0.355	0.372	0.317
4.499	0.882	0.717	0.651	0.181	0.223	0.251	0.368	0.378	0.355	0.371	0.310
5.008	0.881	0.721	0.653	0.179	0.221	0.250	0.367	0.378	0.355	0.371	0.306
5.495	0.881	0.724	0.655	0.178	0.221	0.250	0.365	0.378	0.354	0.371	0.304
5.982	0.880	0.727	0.657	0.176	0.220	0.249	0.363	0.378	0.354	0.370	0.302
6.181	0.880	0.728	0.657	0.176	0.220	0.249	0.363	0.378	0.355	0.370	0.302

Table 31. Continued

$y/(w/2) = 0.704$

NPR	$p/p_{t,j}$ at x/L of— 0.284	0.329	0.358
2.004	0.662	0.305	0.307
2.503	0.659	0.170	0.208
2.995	0.661	0.172	0.208
3.493	0.661	0.173	0.208
3.995	0.662	0.174	0.207
4.499	0.662	0.174	0.207
5.008	0.662	0.174	0.207
5.495	0.661	0.175	0.208
5.982	0.661	0.175	0.207
6.181	0.661	0.175	0.207

$y/(w/2) = 0.926$

NPR	$p/p_{t,j}$ at x/L of— 0.143	0.193	0.242	0.267	0.292	0.329/	0.358	0.375	0.424	0.491	0.557	0.623
2.004	0.571	0.809	0.861	0.786	0.674	0.332	0.322	0.327	0.349	0.427	0.473	0.486
2.503	0.578	0.812	0.862	0.786	0.673	0.099	0.116	0.143	0.298	0.424	0.390	0.397
2.995	0.585	0.813	0.862	0.786	0.673	0.098	0.117	0.143	0.299	0.410	0.348	0.347
3.493	0.591	0.815	0.863	0.786	0.673	0.098	0.117	0.142	0.299	0.407	0.323	0.314
3.995	0.596	0.816	0.863	0.785	0.672	0.097	0.117	0.142	0.299	0.406	0.309	0.293
4.499	0.600	0.816	0.863	0.786	0.672	0.096	0.117	0.141	0.299	0.406	0.299	0.279
5.008	0.605	0.817	0.864	0.785	0.672	0.098	0.118	0.141	0.301	0.405	0.292	0.268
5.495	0.608	0.817	0.863	0.783	0.677	0.093	0.114	0.139	0.298	0.399	0.287	0.261
5.982	0.610	0.817	0.863	0.783	0.677	0.093	0.114	0.139	0.295	0.399	0.284	0.256
6.181	0.610	0.817	0.863	0.783	0.677	0.093	0.112	0.139	0.296	0.398	0.282	0.254

Table 31. Concluded

Sidewall: $z/(w/2) = 0.296$

NPR	$p/p_{t,j}$ at x/L of— 0.127	0.226	0.292	0.391
2.004	0.901	0.374	0.500	0.501
2.503	0.902	0.369	0.502	0.491
2.995	0.902	0.368	0.504	0.490
3.493	0.902	0.369	0.506	0.490
3.995	0.902	0.370	0.508	0.490
4.499	0.902	0.364	0.508	0.490
5.008	0.902	0.361	0.511	0.489
5.495	0.901	0.358	0.511	0.489
5.982	0.901	0.360	0.512	0.488
6.181	0.900	0.360	0.513	0.488

Sidewall: $z/(w/2) = 0.000$

NPR	$p/p_{t,j}$ at x/L of— 0.127	0.226	0.292	0.391	0.474	0.573	0.755	0.937
2.004	0.908	0.742	0.482	0.529	0.478	0.442	0.509	0.493
2.503	0.908	0.741	0.480	0.524	0.451	0.368	0.382	0.394
2.995	0.908	0.740	0.481	0.525	0.451	0.368	0.328	0.354
3.493	0.907	0.740	0.480	0.527	0.450	0.368	0.306	0.309
3.995	0.907	0.739	0.479	0.528	0.450	0.368	0.296	0.233
4.499	0.907	0.738	0.480	0.529	0.450	0.368	0.291	0.203
5.008	0.907	0.738	0.480	0.528	0.450	0.368	0.288	0.186
5.495	0.907	0.738	0.481	0.527	0.449	0.368	0.286	0.175
5.982	0.906	0.737	0.480	0.528	0.449	0.368	0.285	0.169
6.181	0.906	0.737	0.480	0.527	0.448	0.367	0.284	0.167

Sidewall: $z/(w/2) = -0.296$

NPR	$p/p_{t,j}$ at x/L of— 0.127	0.226	0.292	0.391
2.004	0.907	0.370	0.606	0.558
2.503	0.907	0.369	0.603	0.557
2.995	0.907	0.364	0.605	0.557
3.493	0.907	0.353	0.608	0.557
3.995	0.907	0.343	0.608	0.557
4.499	0.907	0.334	0.606	0.556
5.008	0.907	0.324	0.606	0.555
5.495	0.907	0.325	0.607	0.555
5.982	0.906	0.324	0.607	0.555
6.181	0.906	0.323	0.607	0.555

Table 32. Internal Static Pressure Ratios for SCF Nozzle Configuration 15

[Hexagonal geometry at afterburning power, $\delta_{v,p}$ = 10°, and $\delta_{v,y}$ = 20°]

$y/(w/2)$ = 0.074

	$p/p_{t,j}$ at x/L of—										
NPR	0.143	0.193	0.242	0.276	0.304	0.329	0.350	0.424	0.491	0.573	0.656
1.998	0.898	0.794	0.198	0.376	0.449	0.460	0.445	0.412	0.461	0.498	0.507
2.496	0.898	0.795	0.196	0.334	0.411	0.431	0.416	0.358	0.321	0.397	0.414
2.984	0.899	0.794	0.196	0.333	0.411	0.433	0.417	0.359	0.321	0.387	0.385
3.499	0.899	0.794	0.196	0.333	0.409	0.434	0.418	0.359	0.321	0.386	0.376
3.997	0.899	0.792	0.192	0.331	0.406	0.435	0.420	0.359	0.322	0.384	0.373
4.496	0.898	0.791	0.188	0.329	0.403	0.436	0.421	0.360	0.322	0.382	0.371
4.996	0.897	0.789	0.185	0.328	0.398	0.436	0.422	0.360	0.322	0.380	0.370
5.232	0.897	0.788	0.183	0.326	0.395	0.436	0.422	0.360	0.322	0.380	0.369

$y/(w/2)$ = 0.296

	$p/p_{t,j}$ at x/L of—
NPR	0.329
1.998	0.419
2.496	0.390
2.984	0.392
3.499	0.393
3.997	0.396
4.496	0.397
4.996	0.396
5.232	0.396

$y/(w/2)$ = 0.481

	$p/p_{t,j}$ at x/L of—										
NPR	0.143	0.193	0.242	0.284	0.304	0.329	0.350	0.391	0.424	0.573	0.739
1.998	0.879	0.710	0.620	0.231	0.299	0.340	0.374	0.406	0.417	0.503	0.503
2.496	0.880	0.709	0.622	0.188	0.225	0.253	0.367	0.368	0.346	0.392	0.402
2.984	0.879	0.709	0.627	0.187	0.225	0.252	0.366	0.369	0.346	0.382	0.347
3.499	0.879	0.705	0.634	0.187	0.225	0.250	0.363	0.368	0.346	0.378	0.325
3.997	0.879	0.704	0.642	0.185	0.224	0.248	0.361	0.368	0.346	0.376	0.315
4.496	0.878	0.705	0.647	0.184	0.223	0.246	0.358	0.367	0.345	0.375	0.308
4.996	0.877	0.707	0.650	0.181	0.222	0.245	0.355	0.366	0.345	0.374	0.304
5.232	0.876	0.709	0.651	0.180	0.222	0.244	0.354	0.366	0.345	0.374	0.303

Table 32. Continued

$y/(w/2) = 0.704$

NPR	$p/p_{t,j}$ at x/L of— 0.284	0.329	0.358
1.998	0.665	0.316	0.315
2.496	0.666	0.172	0.204
2.984	0.667	0.173	0.204
3.499	0.667	0.174	0.204
3.997	0.667	0.175	0.204
4.496	0.667	0.176	0.204
4.996	0.666	0.176	0.204
5.232	0.664	0.176	0.203

$y/(w/2) = 0.926$

NPR	$p/p_{t,j}$ at x/L of— 0.143	0.193	0.242	0.267	0.292	0.329/	0.358	0.375	0.424	0.491	0.557	0.623
1.998	0.521	0.786	0.853	0.778	0.665	0.343	0.333	0.335	0.362	0.423	0.469	0.486
2.496	0.525	0.789	0.855	0.777	0.667	0.098	0.110	0.138	0.306	0.421	0.391	0.398
2.984	0.530	0.791	0.855	0.777	0.667	0.097	0.110	0.138	0.298	0.404	0.349	0.348
3.499	0.536	0.792	0.857	0.777	0.667	0.095	0.110	0.138	0.294	0.398	0.325	0.315
3.997	0.543	0.793	0.857	0.778	0.667	0.096	0.110	0.137	0.291	0.396	0.311	0.295
4.496	0.547	0.794	0.858	0.778	0.667	0.094	0.110	0.137	0.286	0.395	0.301	0.281
4.996	0.552	0.794	0.859	0.778	0.666	0.094	0.110	0.137	0.282	0.395	0.295	0.270
5.232	0.554	0.794	0.859	0.778	0.666	0.094	0.110	0.136	0.280	0.395	0.292	0.266

Table 32. Concluded

Sidewall: $z/(w/2) = 0.296$

NPR	$p/p_{t,j}$ at x/L of— 0.127	0.226	0.292	0.391
1.998	0.881	0.359	0.461	0.498
2.496	0.880	0.347	0.462	0.483
2.984	0.882	0.343	0.463	0.483
3.499	0.882	0.349	0.466	0.482
3.997	0.882	0.348	0.469	0.483
4.496	0.882	0.345	0.470	0.483
4.996	0.881	0.343	0.470	0.482
5.232	0.880	0.342	0.470	0.482

Sidewall: $z/(w/2) = 0.000$

NPR	$p/p_{t,j}$ at x/L of— 0.127	0.226	0.292	0.391	0.474	0.573	0.755	0.937
1.998	0.886	0.726	0.466	0.514	0.482	0.447	0.509	0.494
2.496	0.886	0.725	0.463	0.506	0.448	0.367	0.385	0.397
2.984	0.887	0.725	0.463	0.508	0.447	0.367	0.329	0.355
3.499	0.887	0.724	0.462	0.512	0.447	0.367	0.305	0.307
3.997	0.887	0.724	0.461	0.512	0.447	0.367	0.296	0.233
4.496	0.887	0.723	0.461	0.514	0.446	0.367	0.290	0.205
4.996	0.886	0.722	0.460	0.514	0.446	0.367	0.287	0.187
5.232	0.885	0.722	0.460	0.513	0.445	0.366	0.286	0.181

Sidewall: $z/(w/2) = -0.296$

NPR	$p/p_{t,j}$ at x/L of— 0.127	0.226	0.292	0.391
1.998	0.886	0.348	0.588	0.551
2.496	0.887	0.349	0.587	0.547
2.984	0.888	0.345	0.589	0.547
3.499	0.888	0.336	0.594	0.548
3.997	0.888	0.328	0.596	0.547
4.496	0.887	0.320	0.594	0.548
4.996	0.887	0.314	0.593	0.547
5.232	0.887	0.312	0.592	0.546

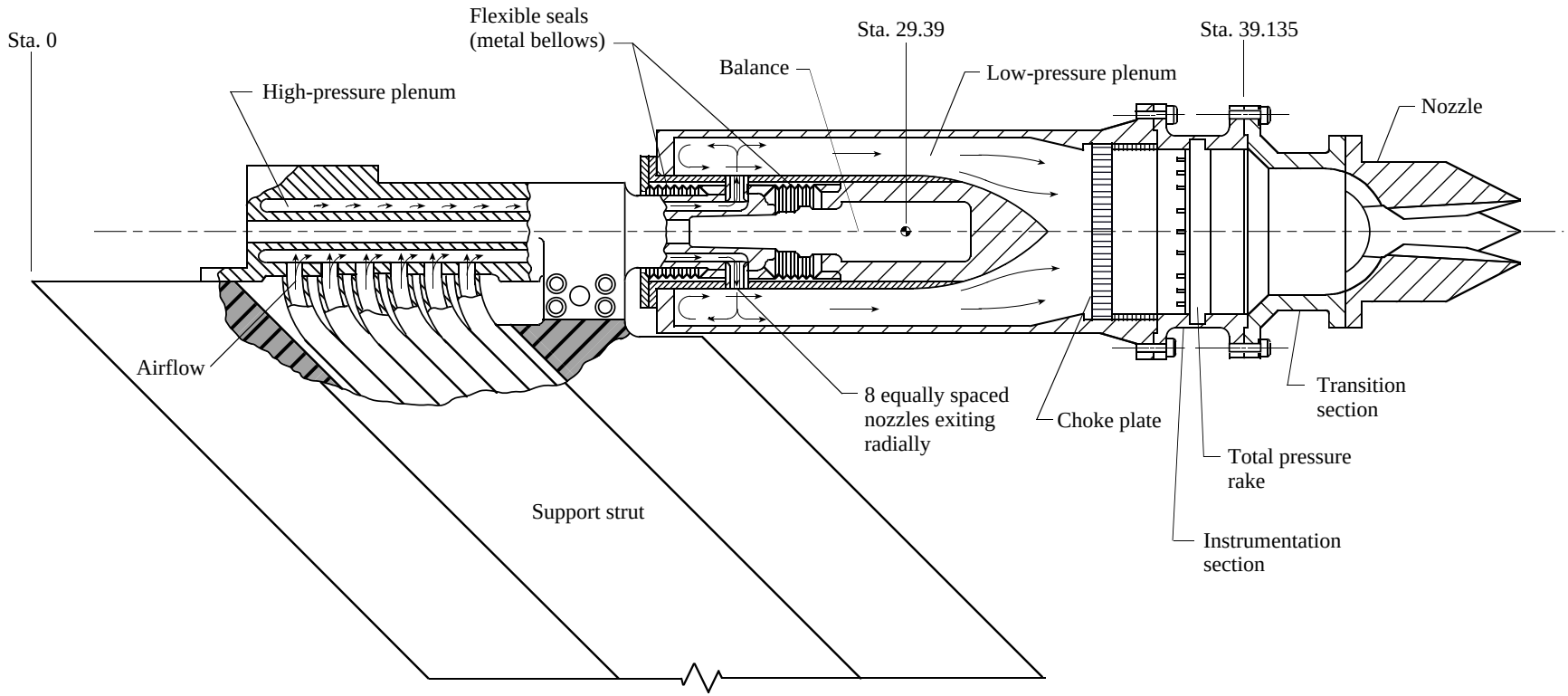

Figure 1. Propulsion simulation system with typical nozzle configuration installed. Station numbers are in inches.

(a) Upper and lower surfaces of unvectored hexagonal configuration.

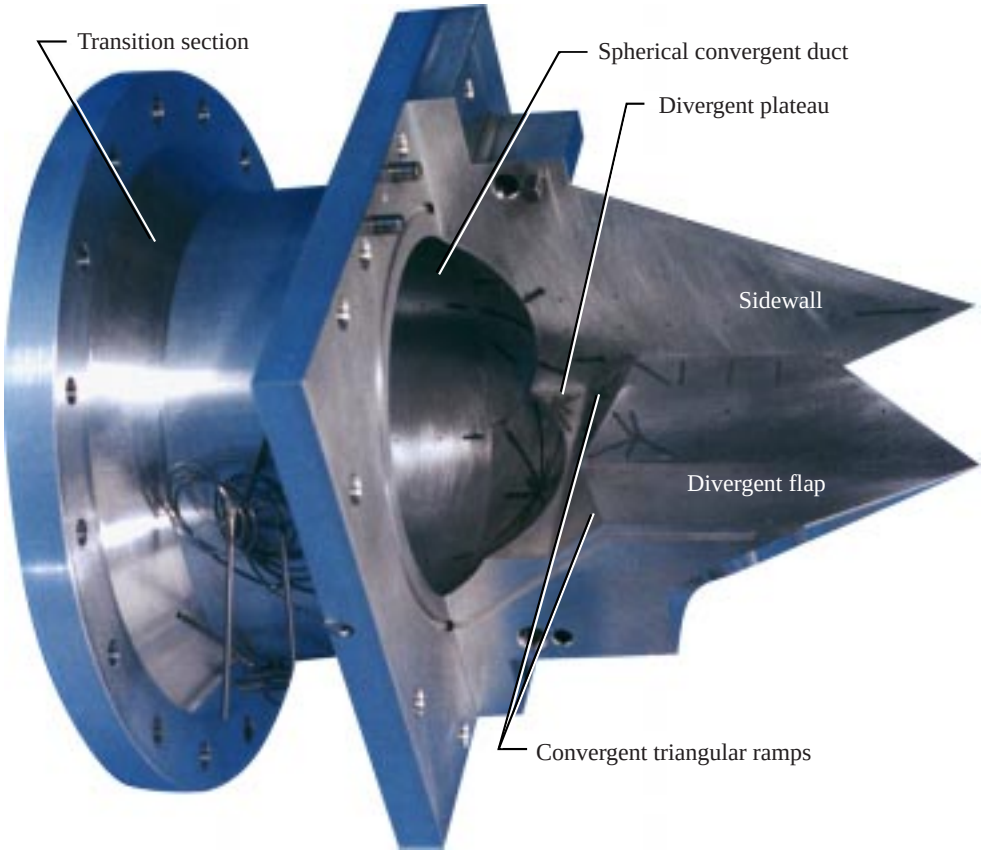

(b) Lower surface and right sidewall of unvectored hexagonal configuration installed on transition section.

Figure 2. Various model hardware components for SCF nozzle at dry power.

(c) Upper and lower surfaces of unvectored bowtie configuration.

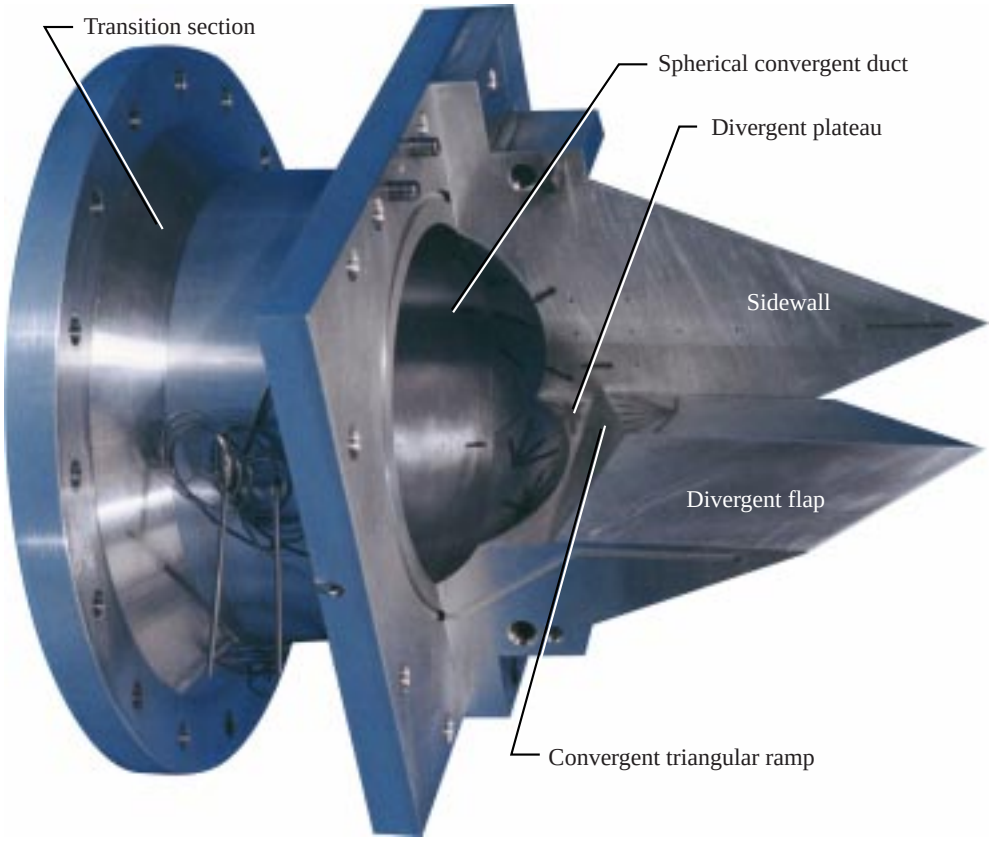

(d) Lower surface and right sidewall of unvectored bowtie configuration installed on transition section.

Figure 2. Concluded.

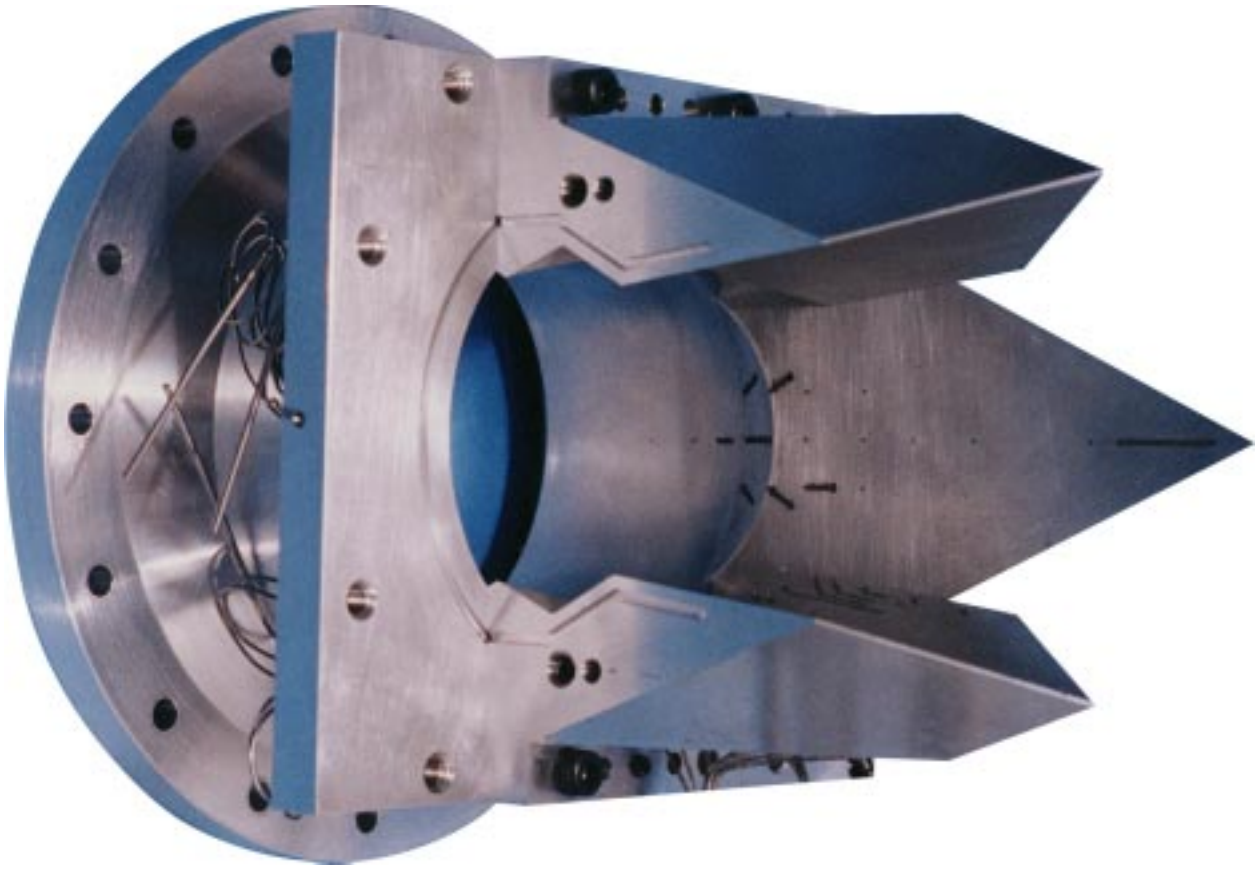

(a) Unvectored hexagonal configuration with left sidewall removed.

Figure 3. Afterburning configurations for SCF nozzle.

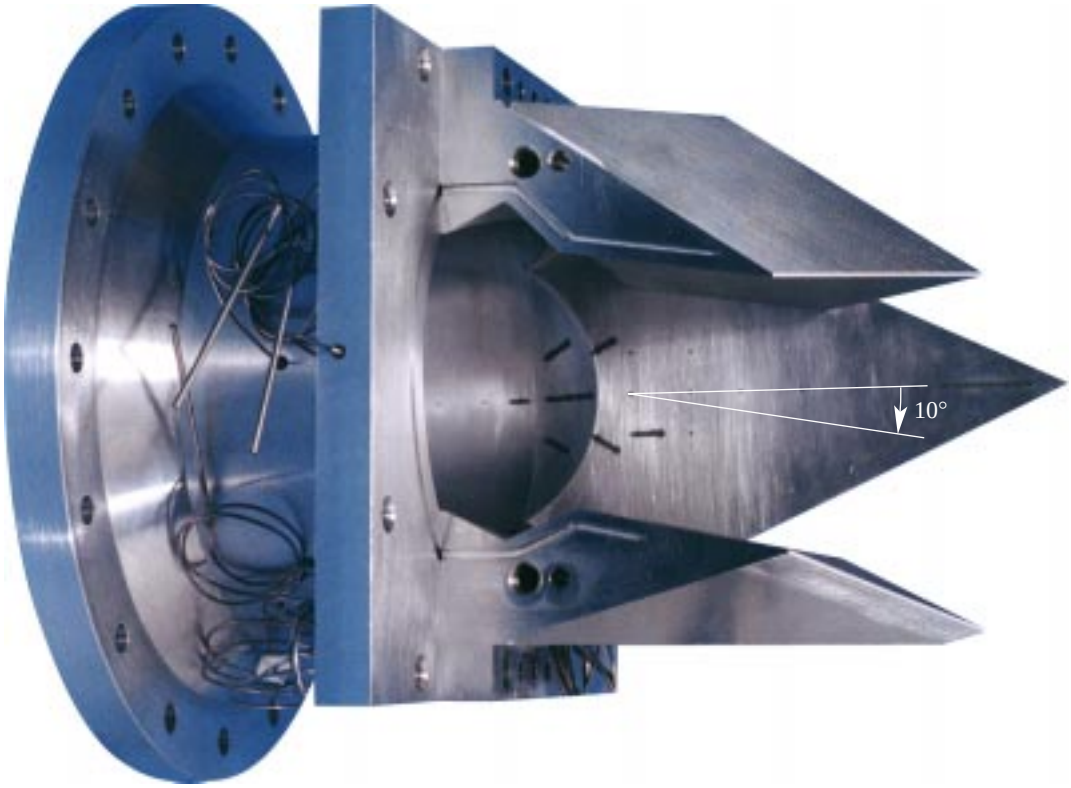

(b) Pitch thrust-vectored hexagonal configuration with left sidewall removed.

Figure 3. Concluded.

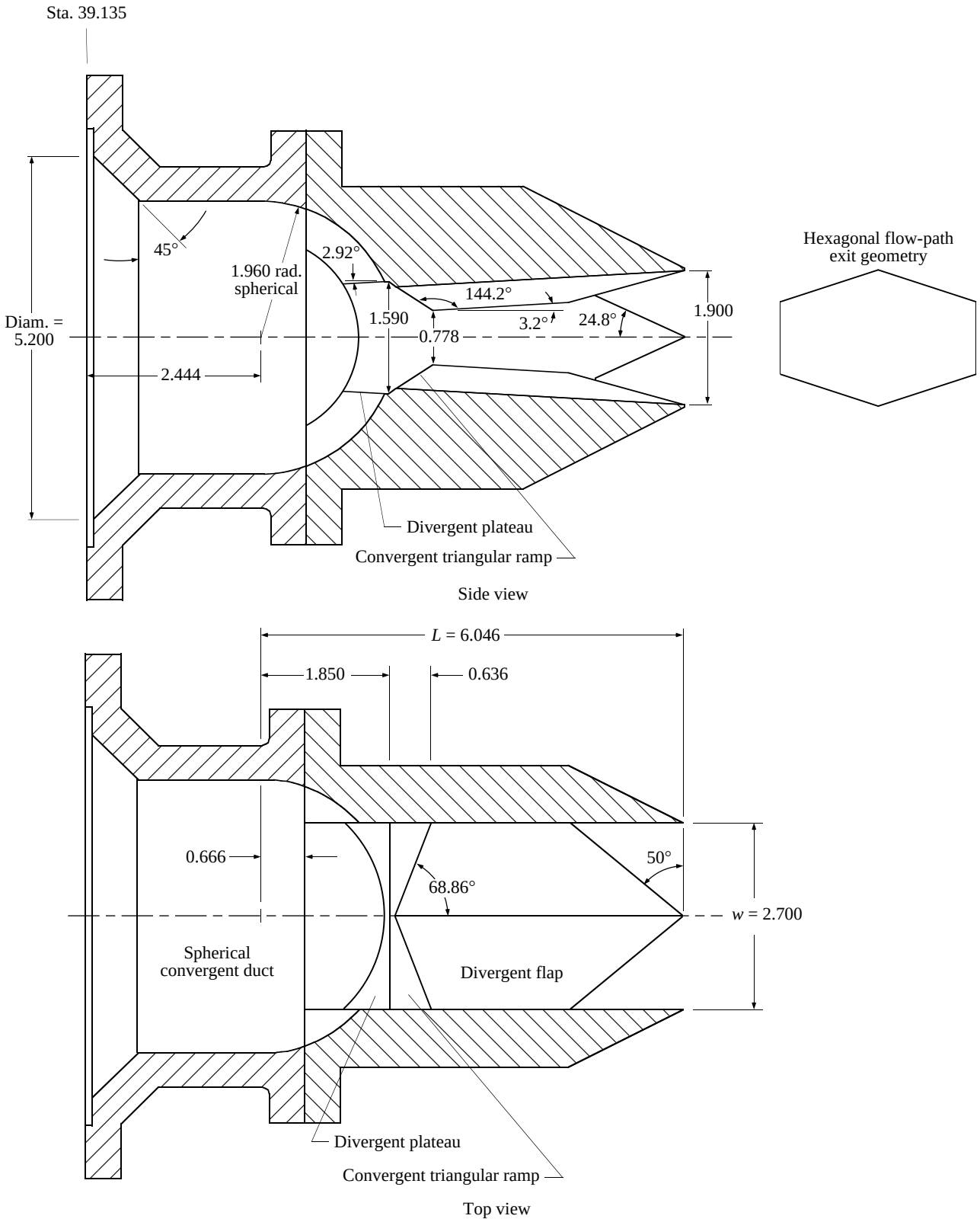

(a) Unvectored hexagonal configuration at dry power.

Figure 4. Cross sections (through nozzle axes) of SCF nozzle. Linear dimensions are in inches.

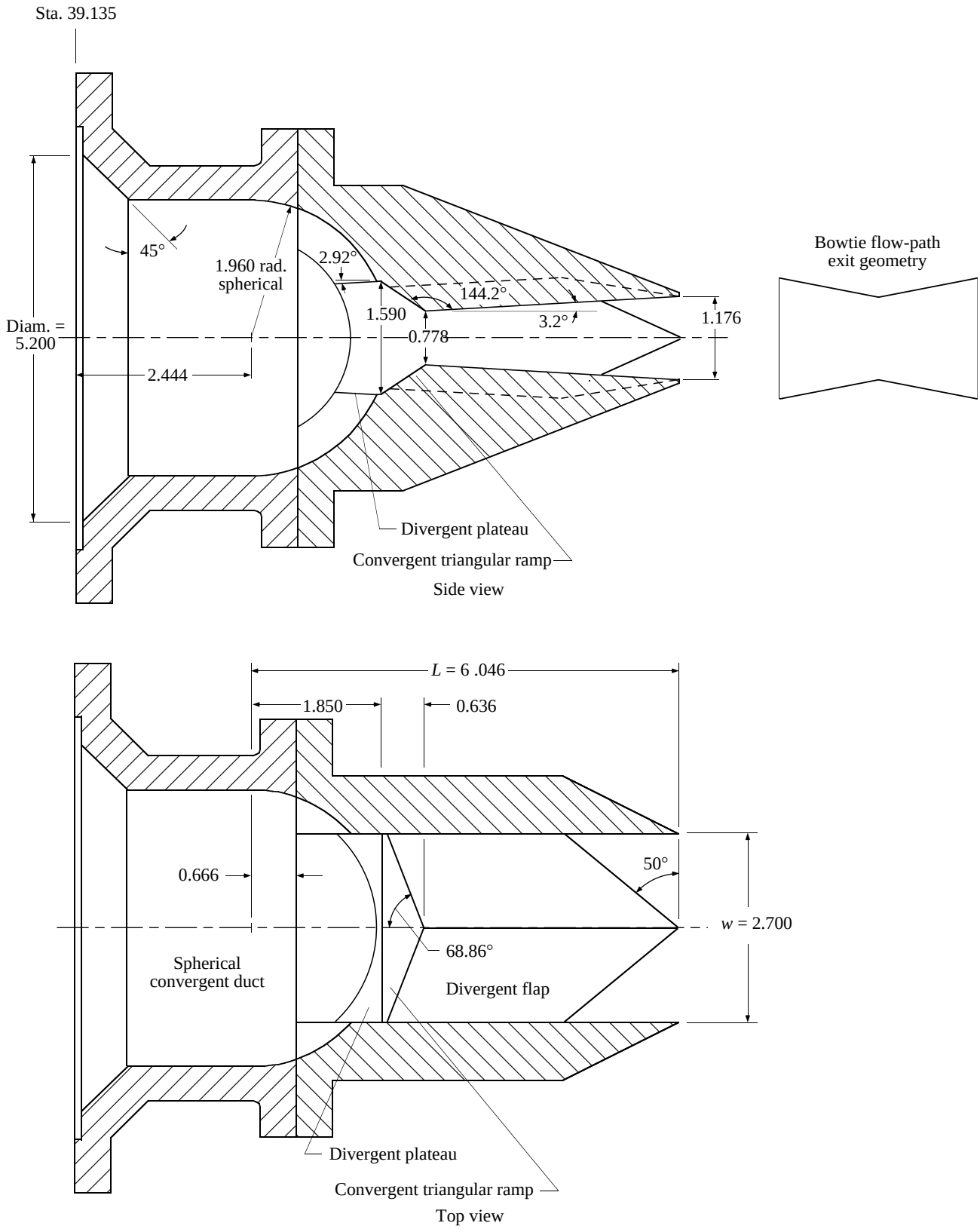

(b) Unvectored bowtie configuration.

Figure 4. Continued.

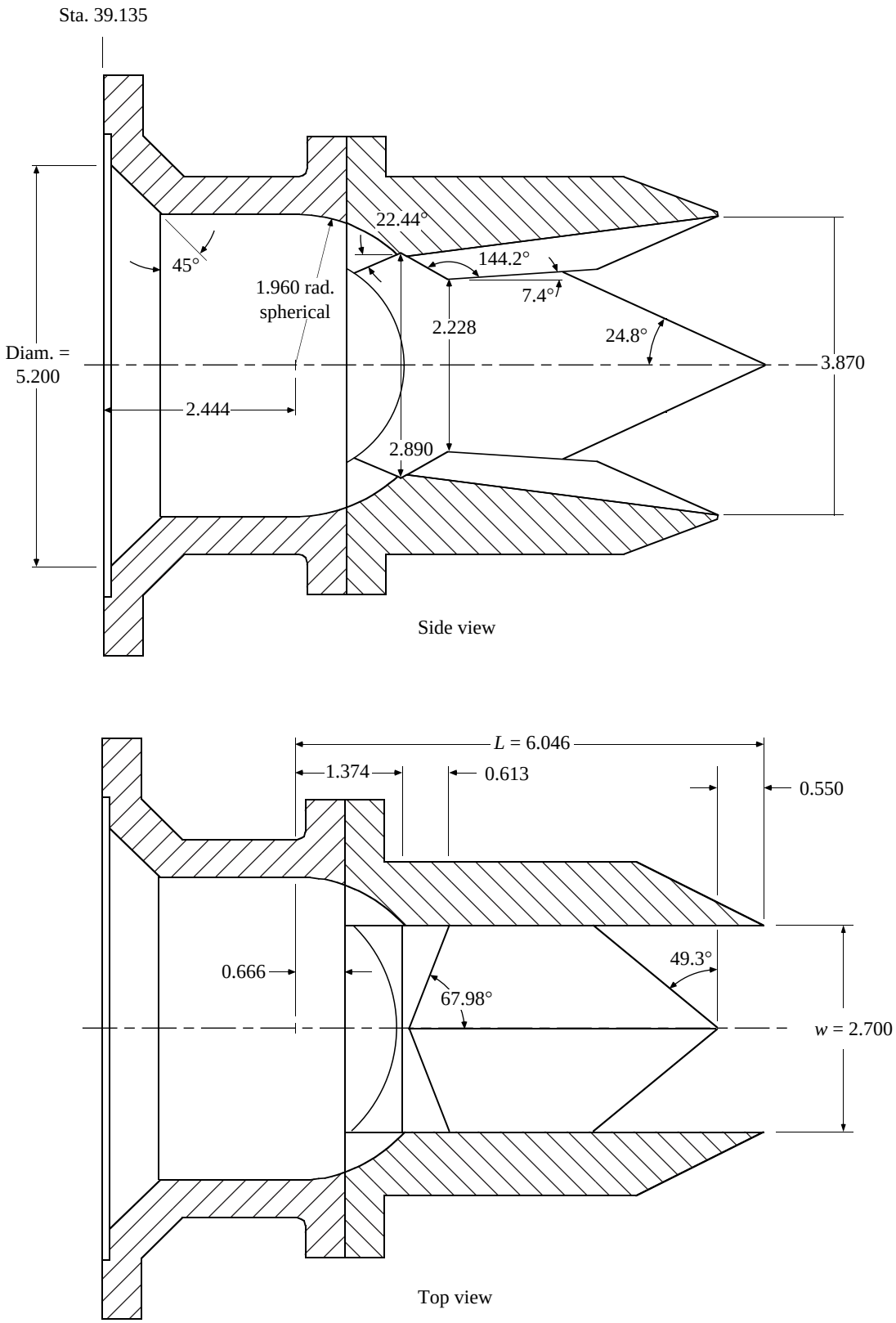

(c) Unvectored hexagonal configuration at afterburning power.

Figure 4. Continued.

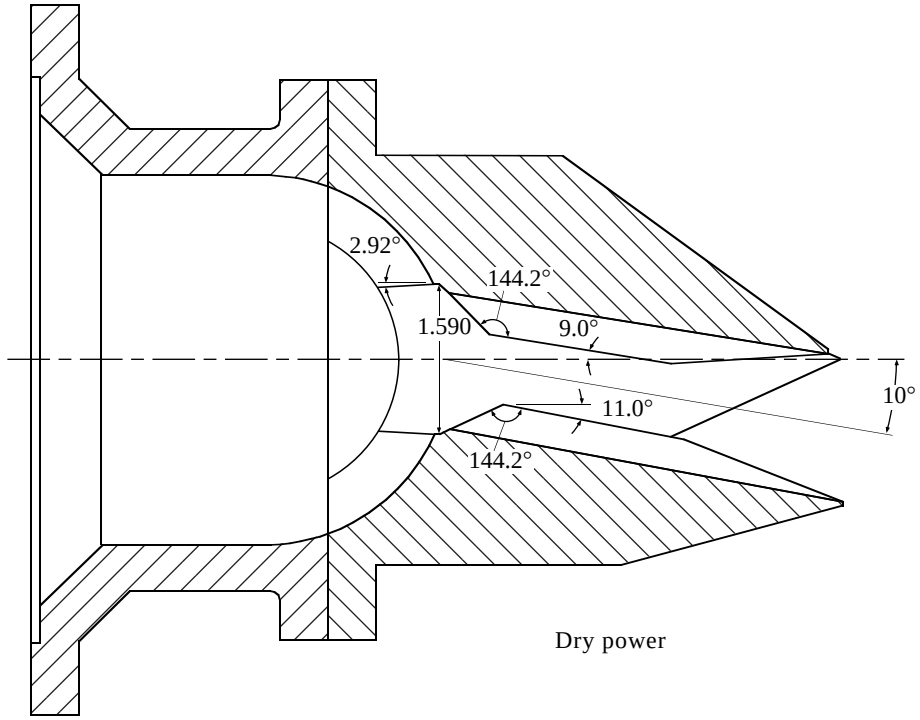

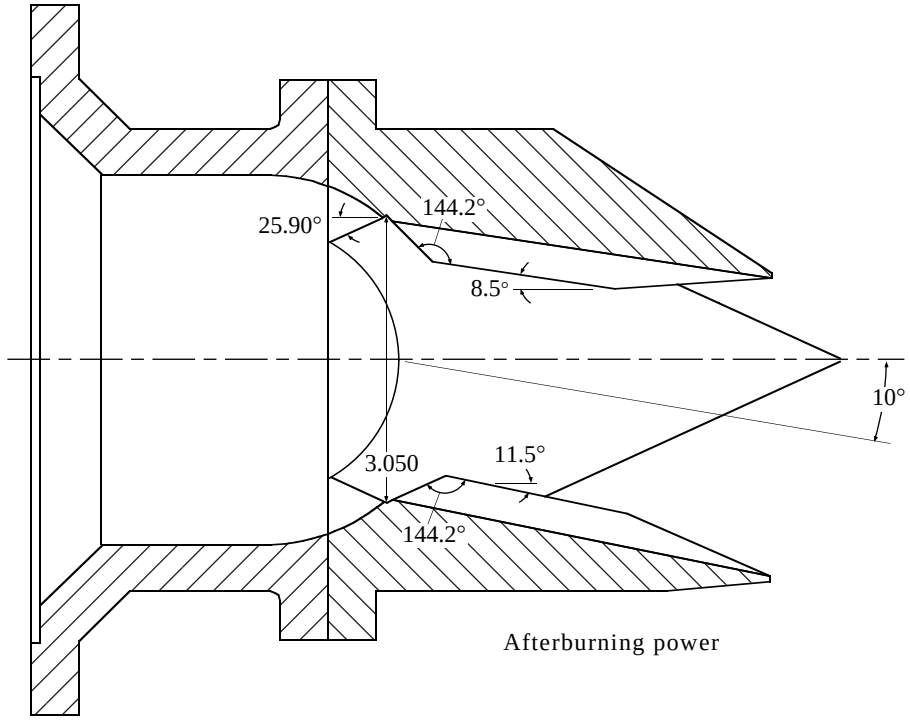

(d) Pitch thrust-vectored configurations (side view).

Figure 4. Continued.

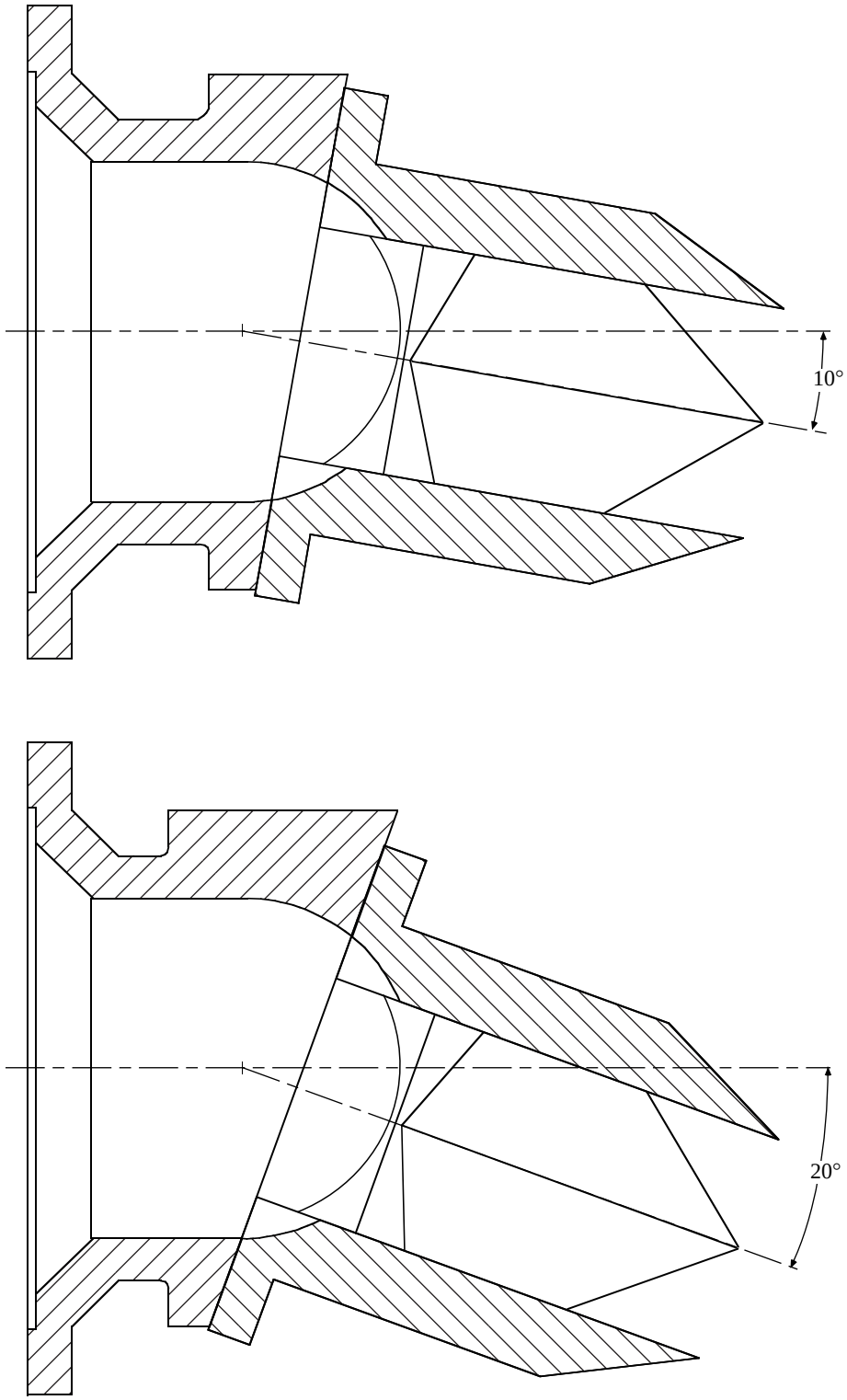

(e) Yaw thrust-vector angles obtained by gimballing (top view).

Figure 4. Concluded.

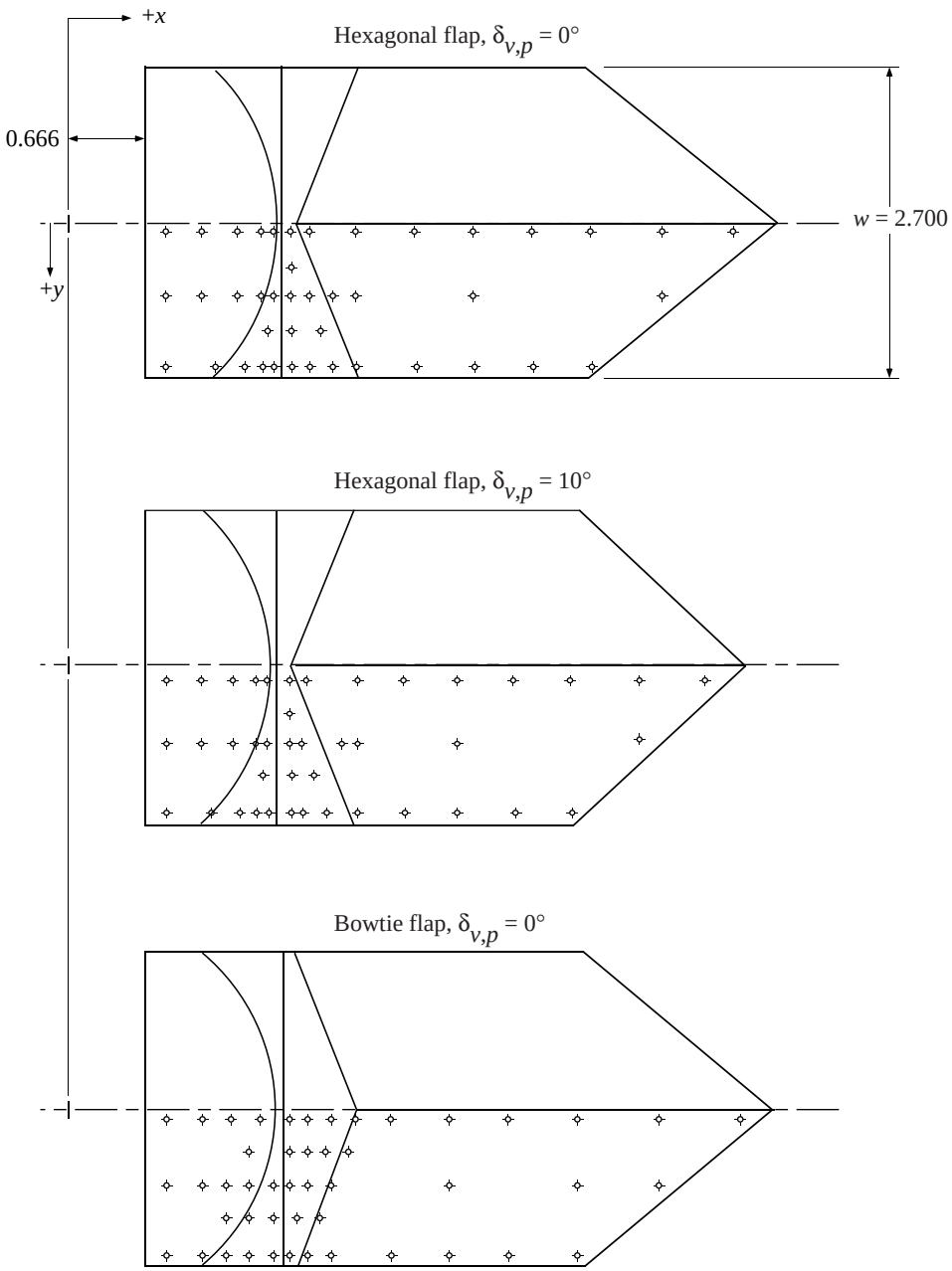

(a) Configurations at dry power.

Figure 5. Locations of pressure orifices. Coordinates are in table 2.

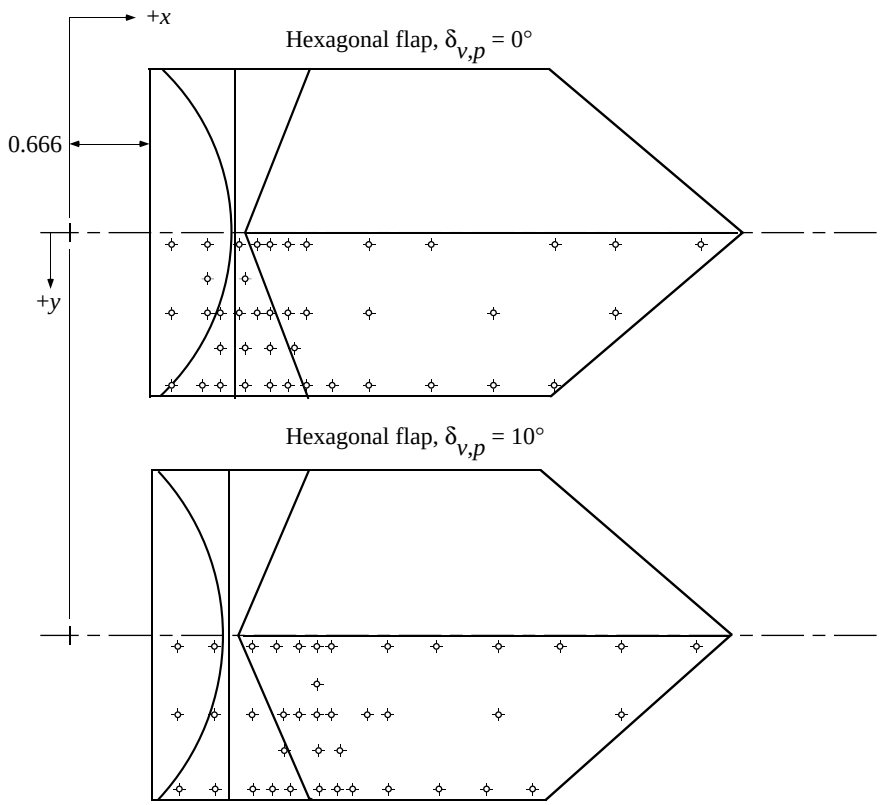

(b) Configurations at afterburning power.

Figure 5. Continued.

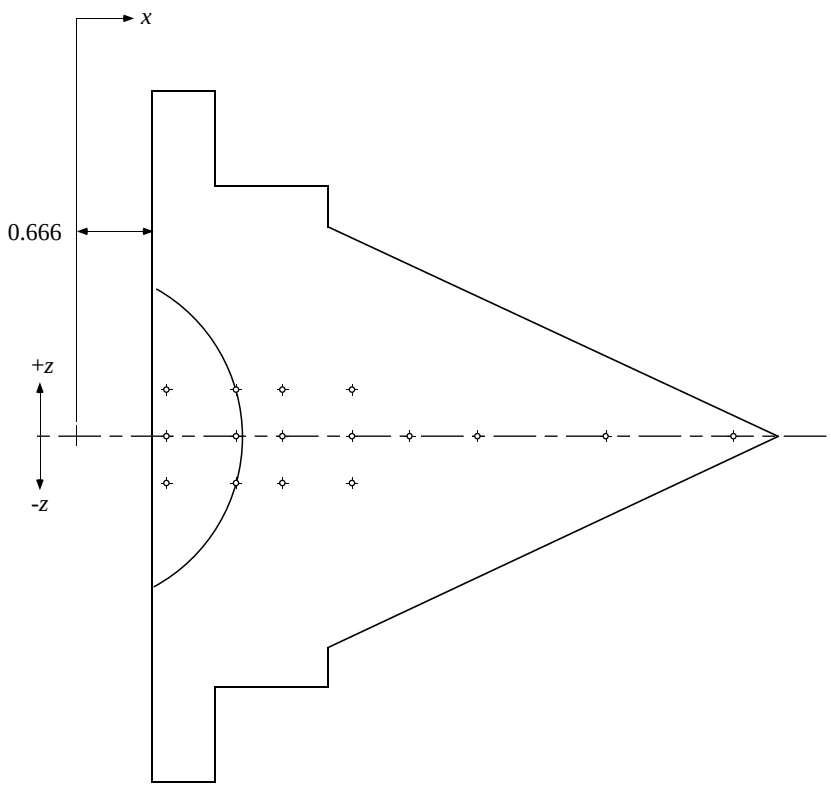

(c) Sidewall.

Figure 5. Concluded.

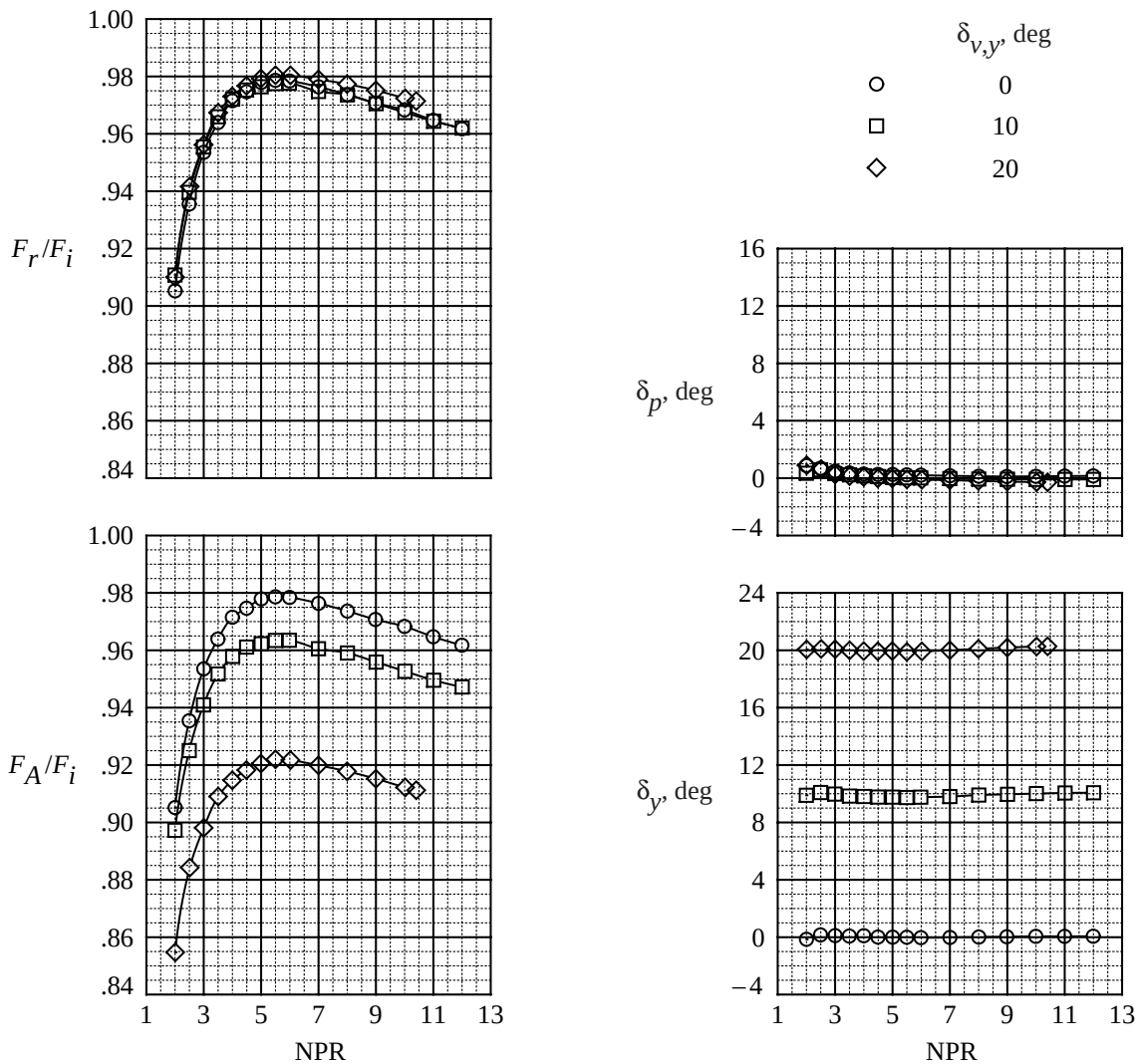

Figure 6. Internal static performance of SCF nozzle with bowtie geometry at dry power and $\delta_{v,p}$ = 0°.

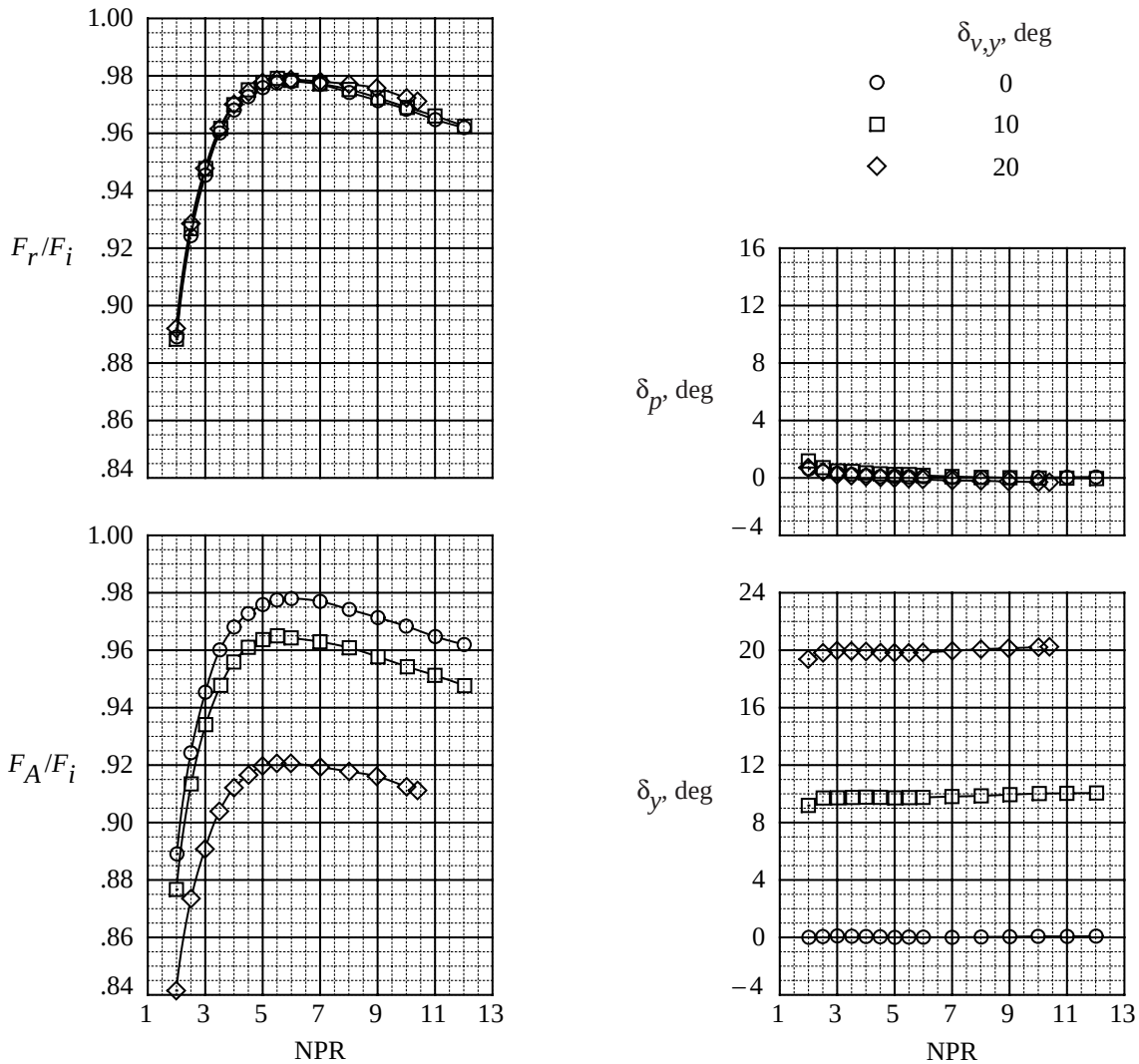

(a) $\delta_{v,p} = 0°$.

Figure 7. Internal static performance of SCF nozzle with hexagonal geometry at dry power.

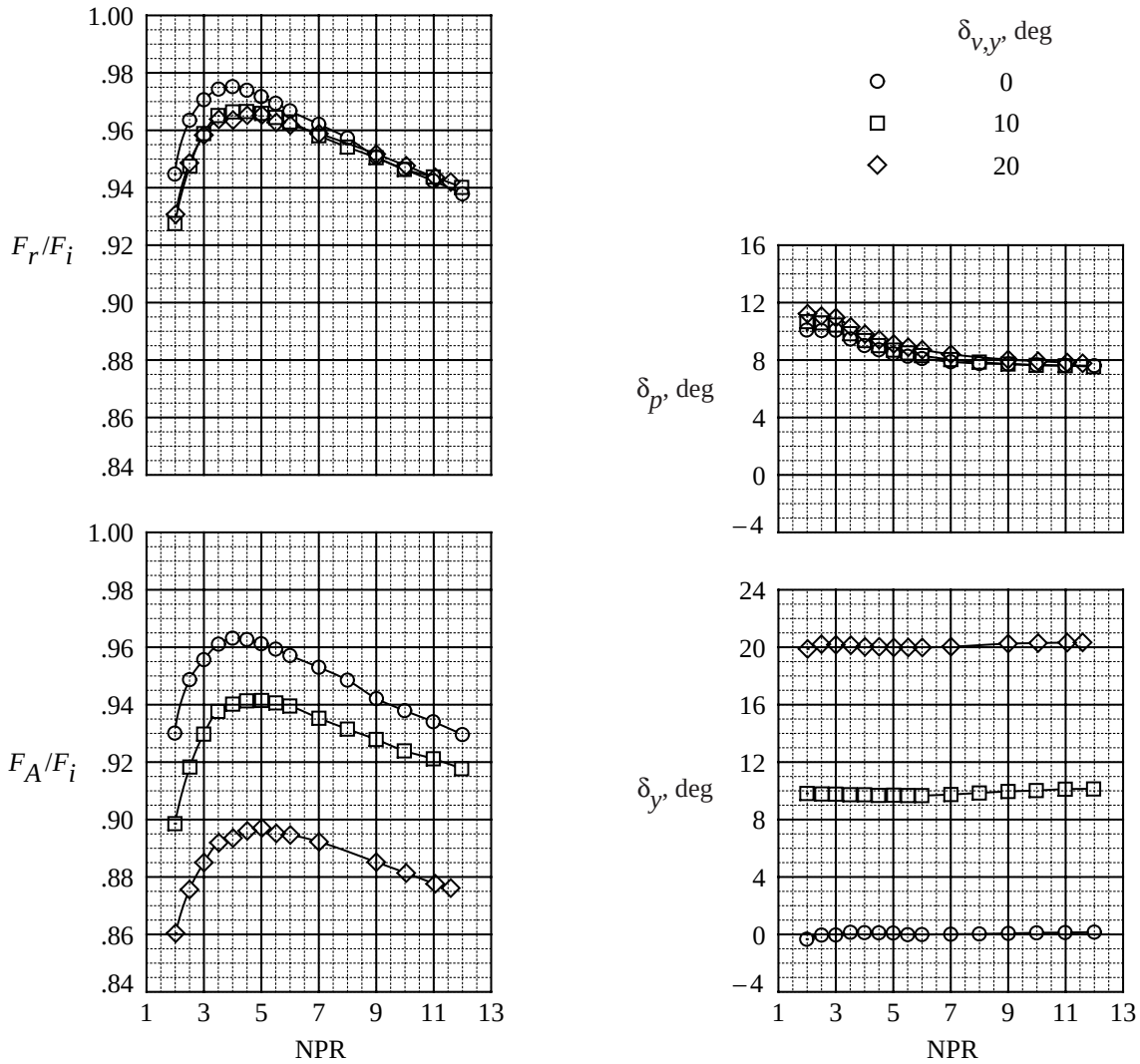

(b) $\delta_{v,p}$ = 10°.

Figure 7. Concluded.

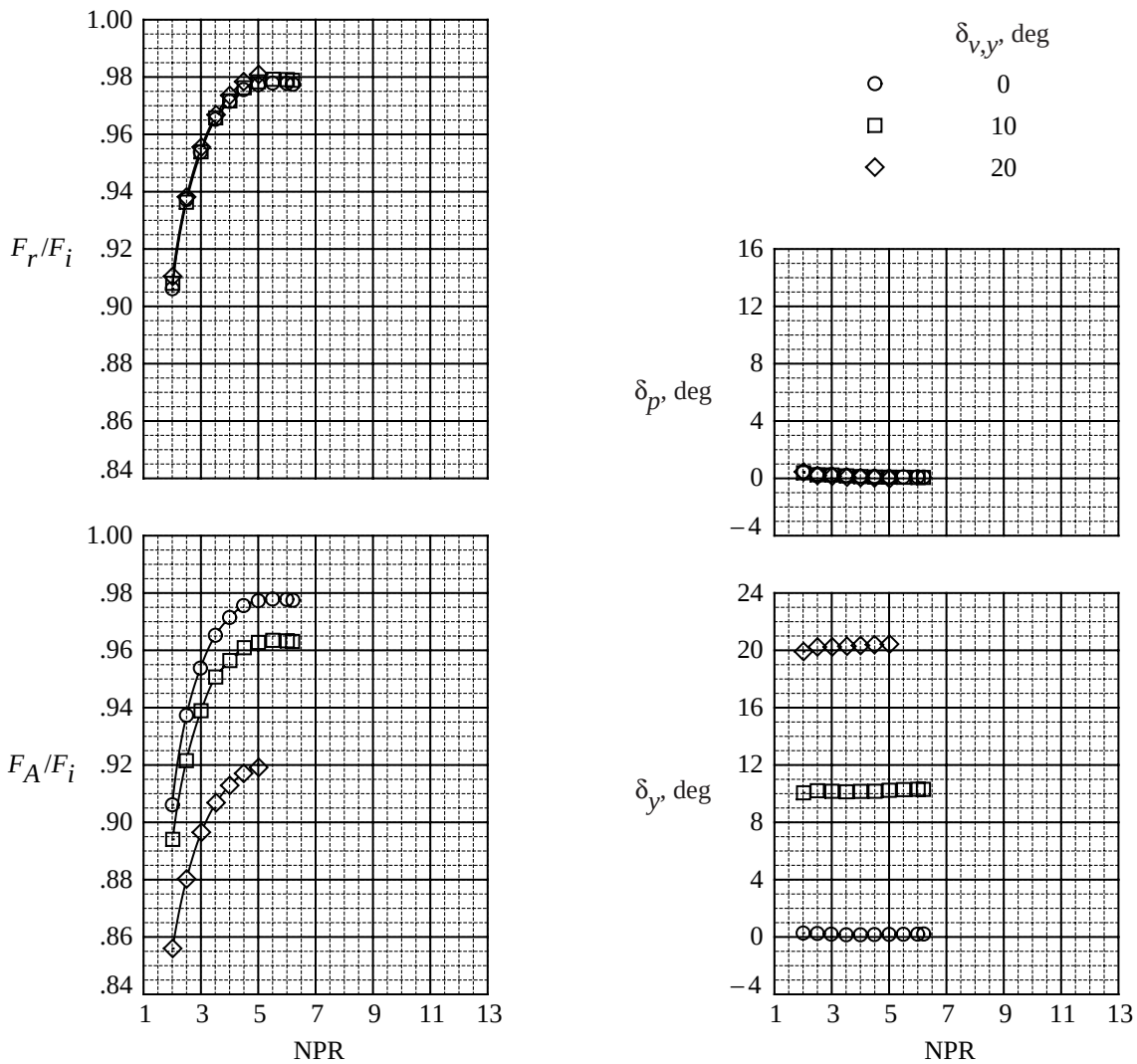

(a) $\delta_{v,p} = 0°$.

Figure 8. Internal static performance of SCF nozzle with hexagonal geometry at afterburning power.

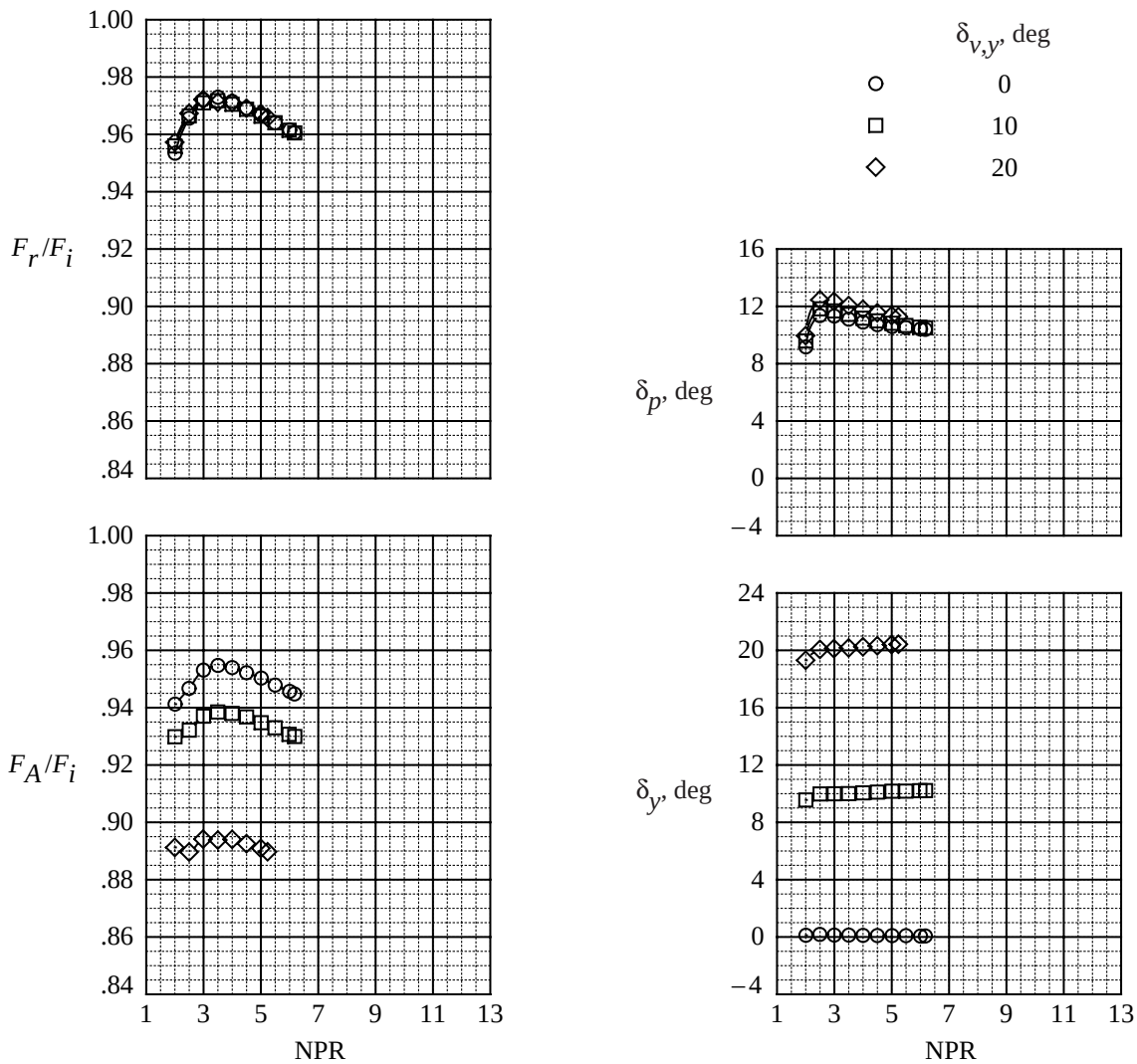

(b) $\delta_{v,p} = 10°$.

Figure 8. Concluded.

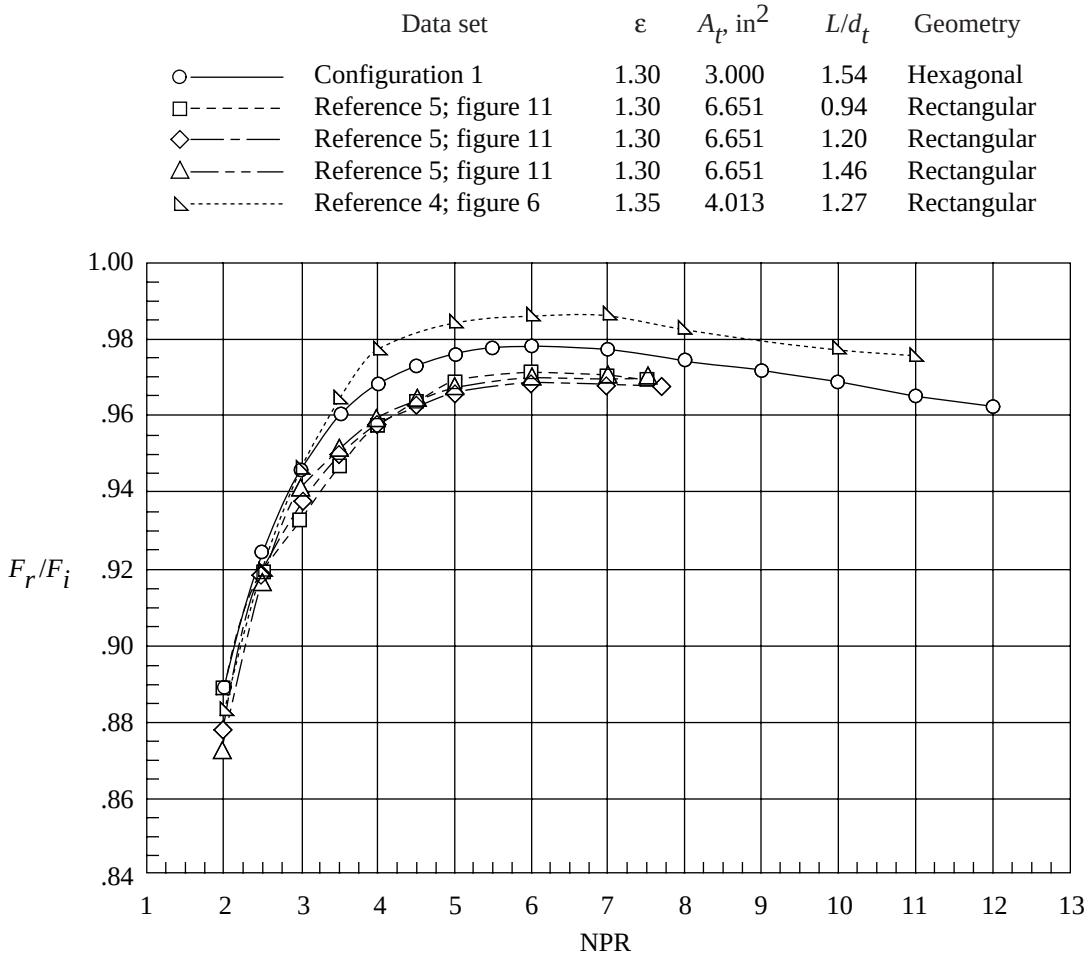

Figure 9. Thrust performance data for SCF nozzles with hexagonal and rectangular divergent-duct cross sections. $\delta_{v,p} = 0°$.

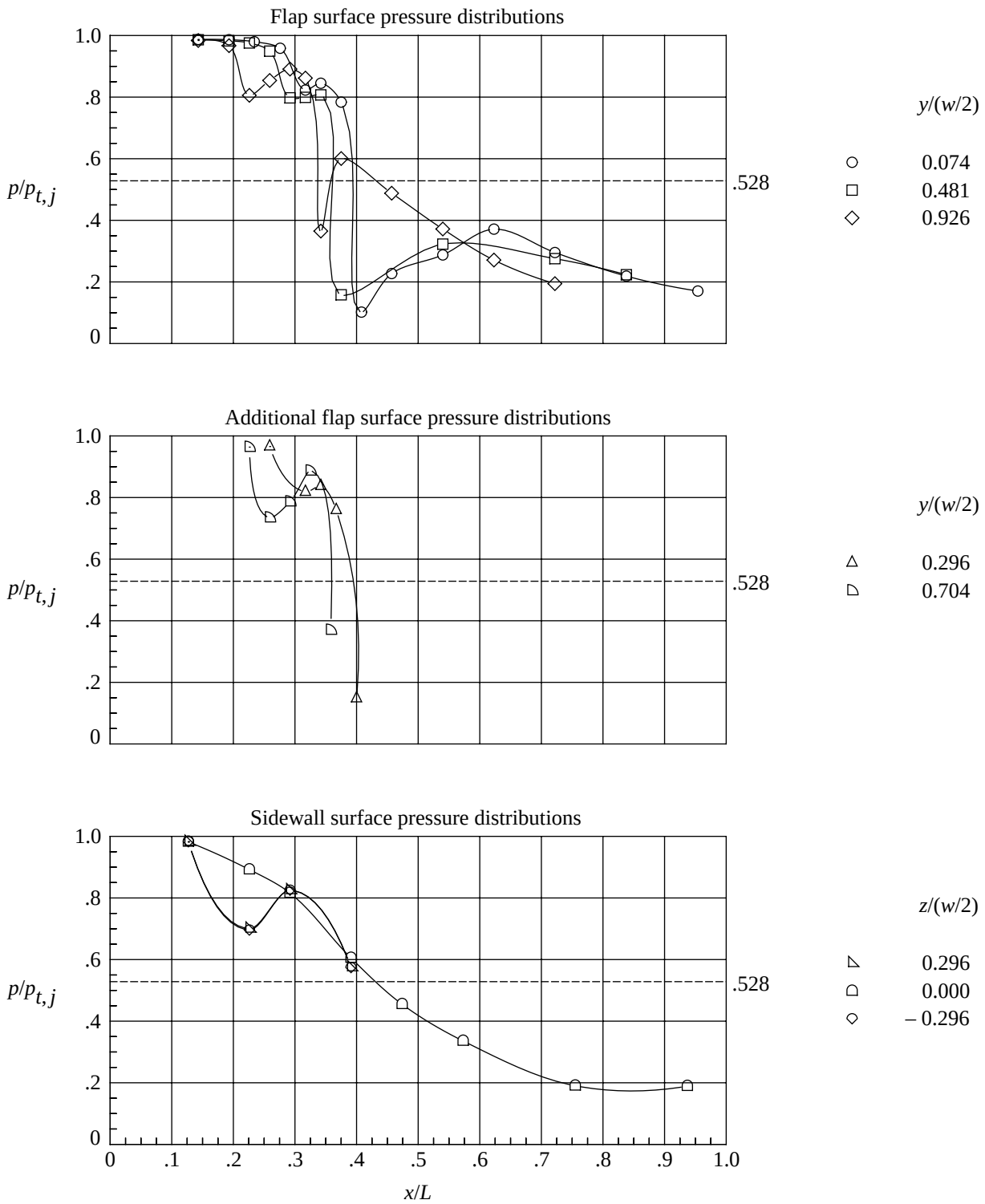

(a) $\delta_{v,y} = 0°$.

Figure 10. Internal static pressure distributions of bowtie SCF nozzle at dry power, $\delta_{v,p} = 0°$, and NPR = 5.00.

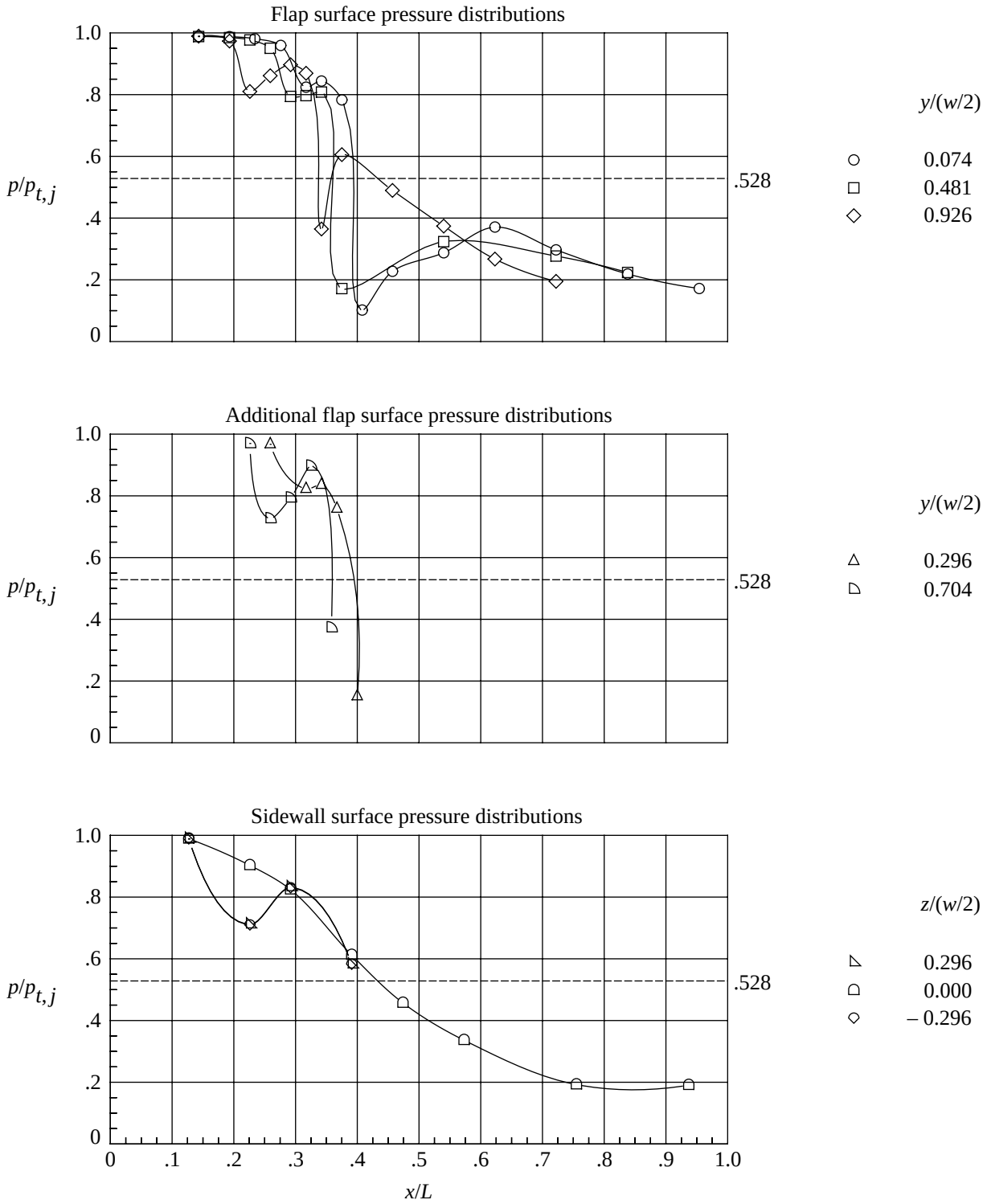

(b) $\delta_{v,y} = 10°$.

Figure 10. Continued.

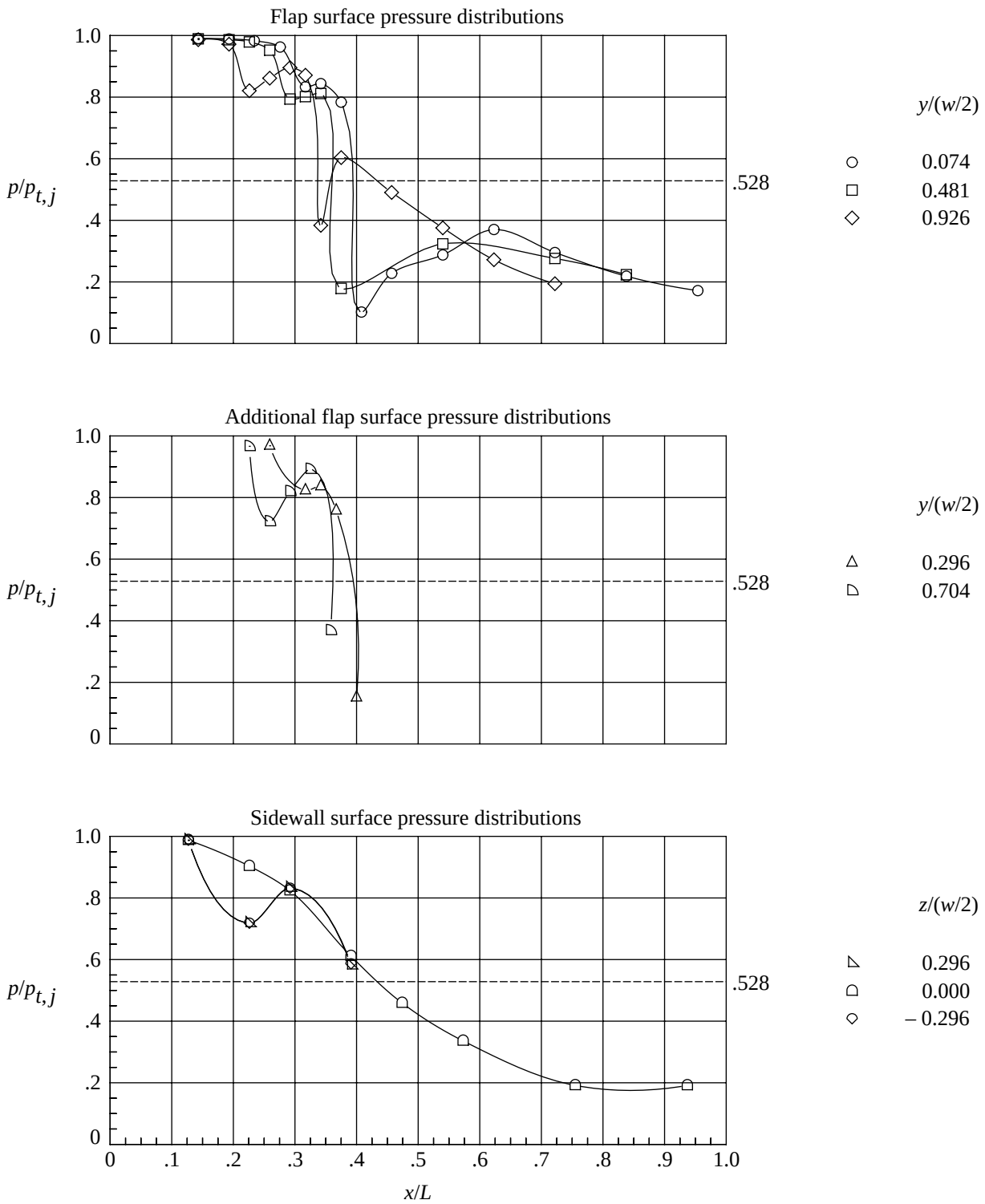

(c) $\delta_{v,y} = 20°$.

Figure 10. Concluded.

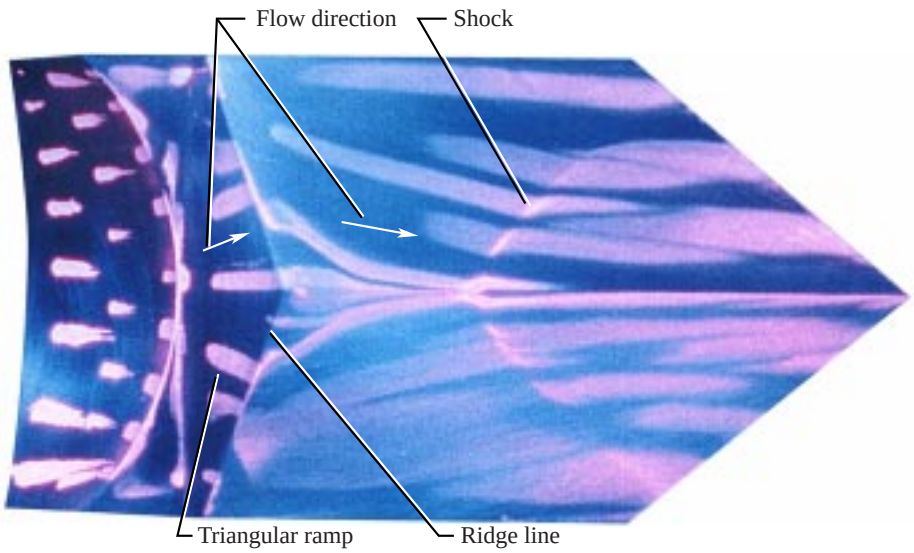

(a) Lower surface.

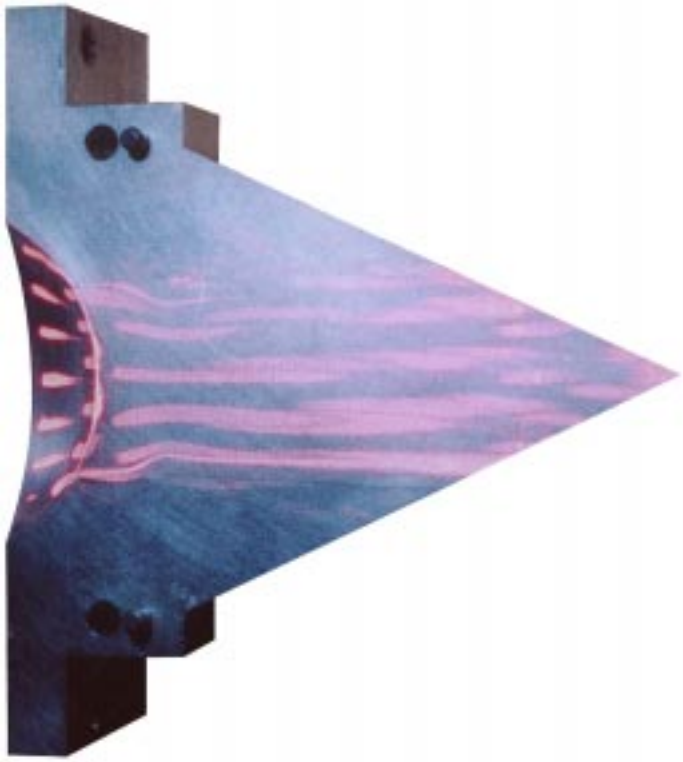

(b) Right sidewall.

Figure 11. Surface flow visualization on bowtie nozzle at dry power, $\delta_{v,p} = 0°$, $\delta_{v,y} = 0°$, and NPR = 5.00.

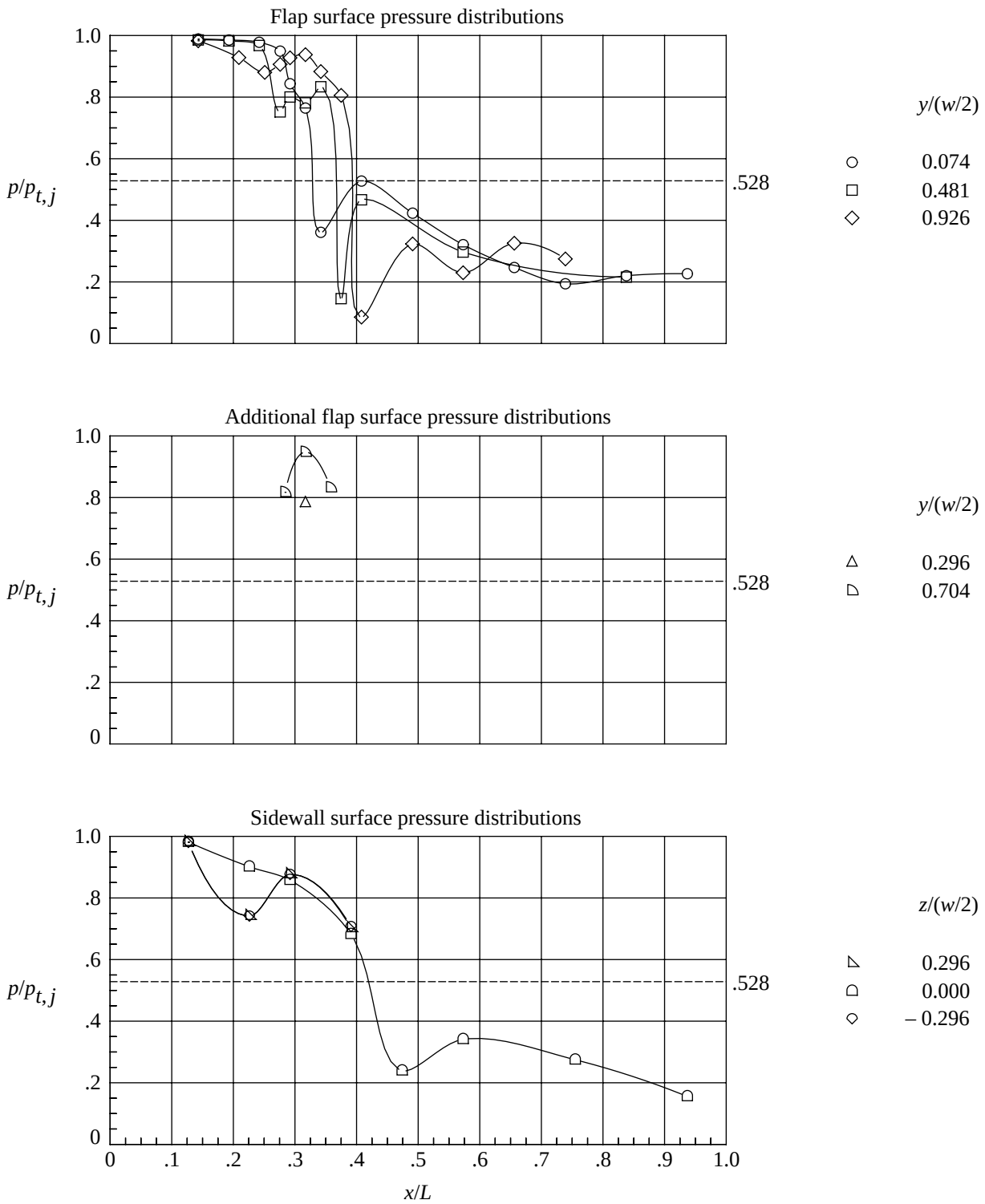

(a) $\delta_{v,y} = 0°$.

Figure 12. Internal static pressure distributions of hexagonal SCF nozzle at dry power, $\delta_{v,p} = 0°$, and NPR = 5.01.

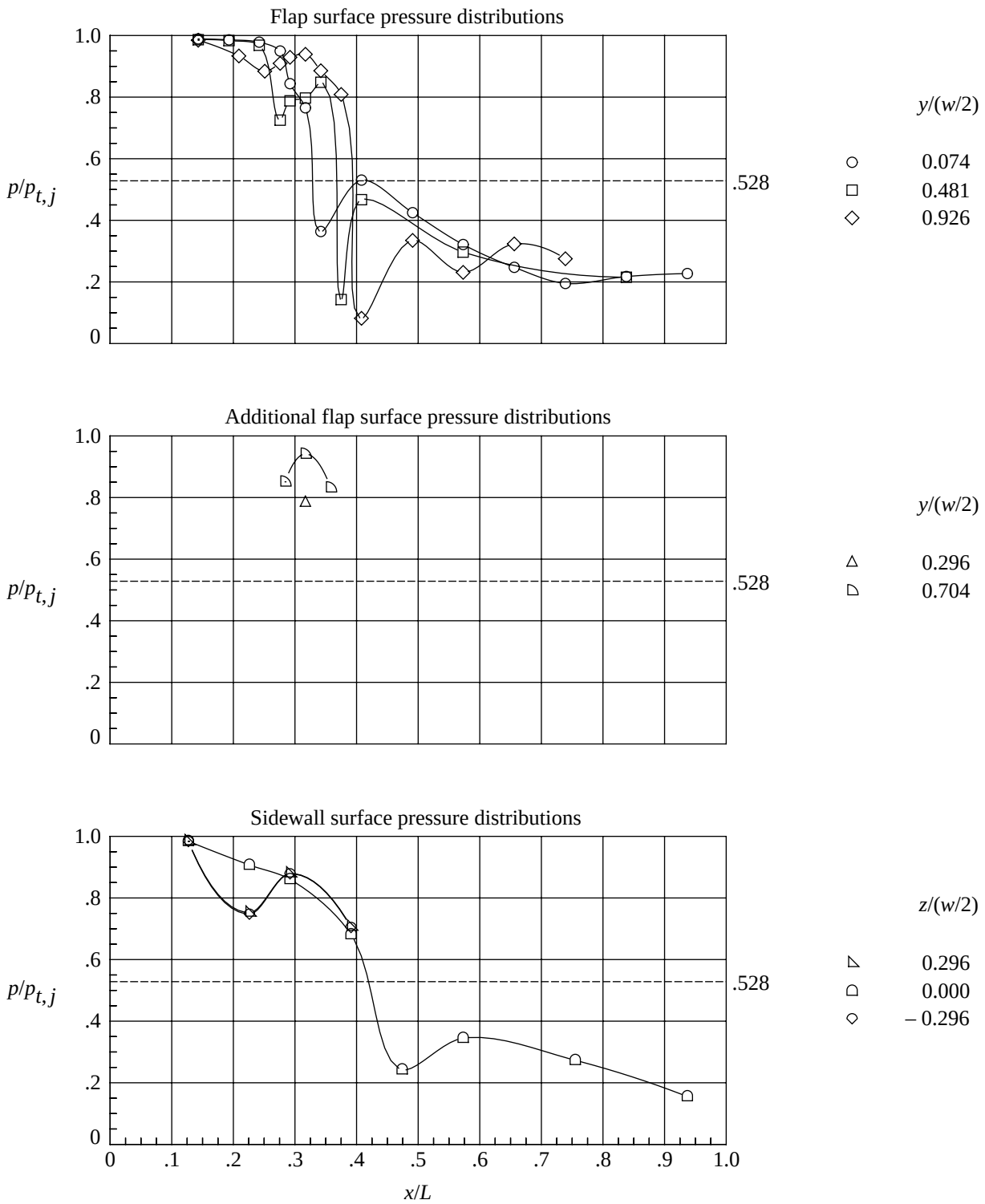

(b) $\delta_{v,y} = 10°$.

Figure 12. Continued.

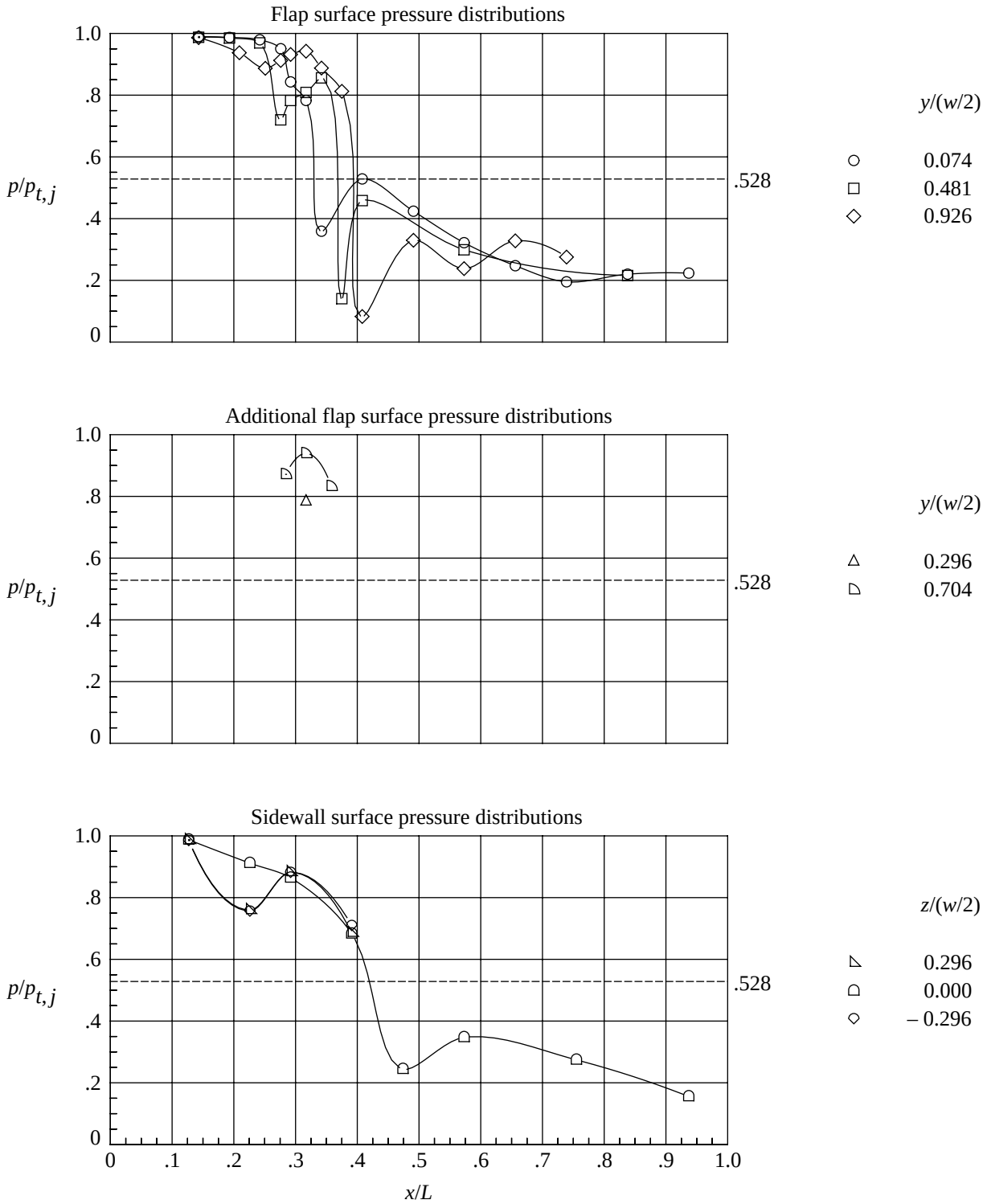

(c) $\delta_{v,y} = 20°$.

Figure 12. Concluded.

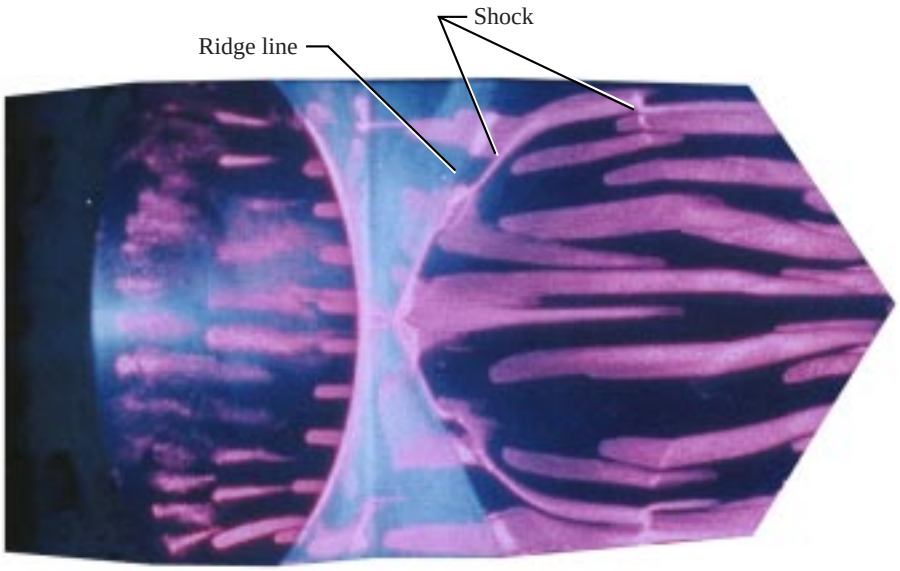

(a) Lower surface.

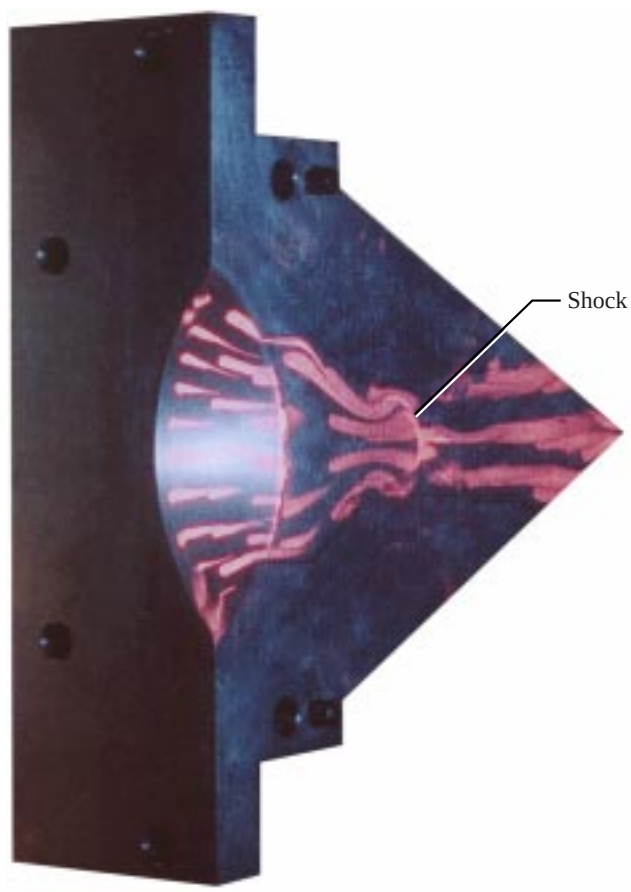

(b) Right sidewall.

Figure 13. Surface flow visualization on hexagonal nozzle at dry power, $\delta_{v,p}$ = 0°, $\delta_{v,y}$ = 0°, and NPR = 5.00.

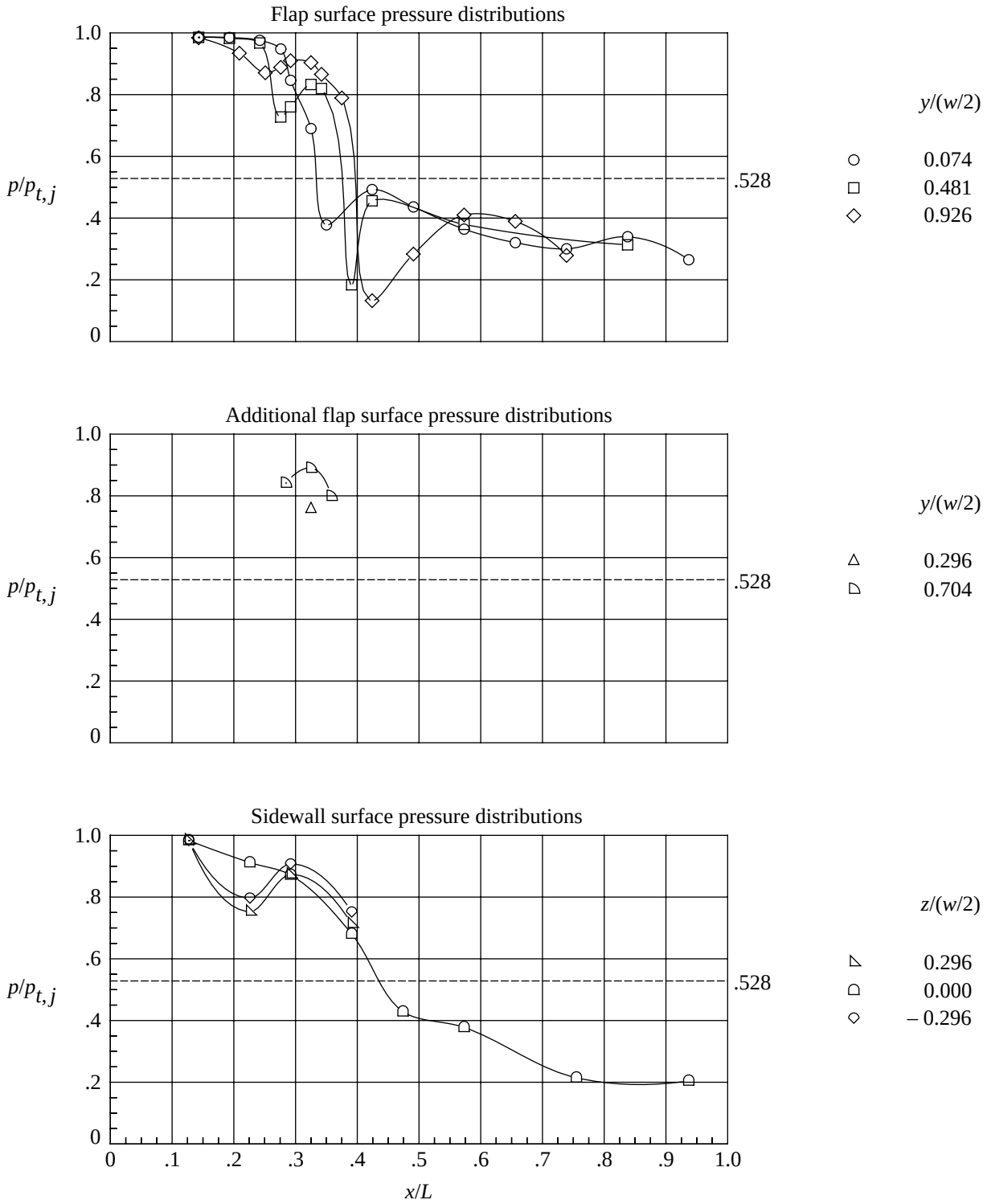

(a) $\delta_{v,y} = 0°$.

Figure 14. Internal static pressure distributions of lower (suction) flap of hexagonal SCF nozzle at dry power, $\delta_{v,p} = 10°$, and NPR = 4.99.

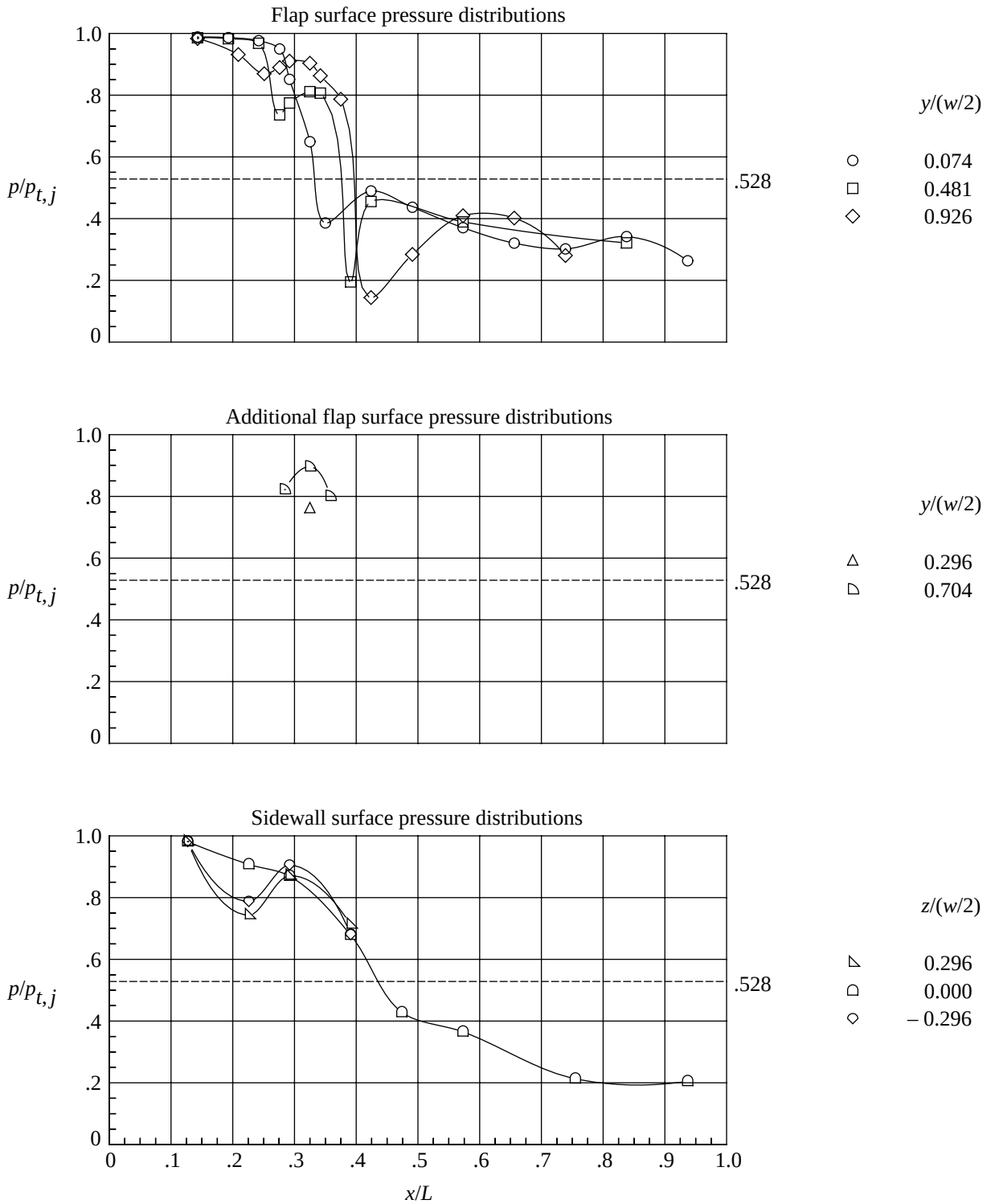

(b) $\delta_{v,y} = 10°$.

Figure 14. Continued.

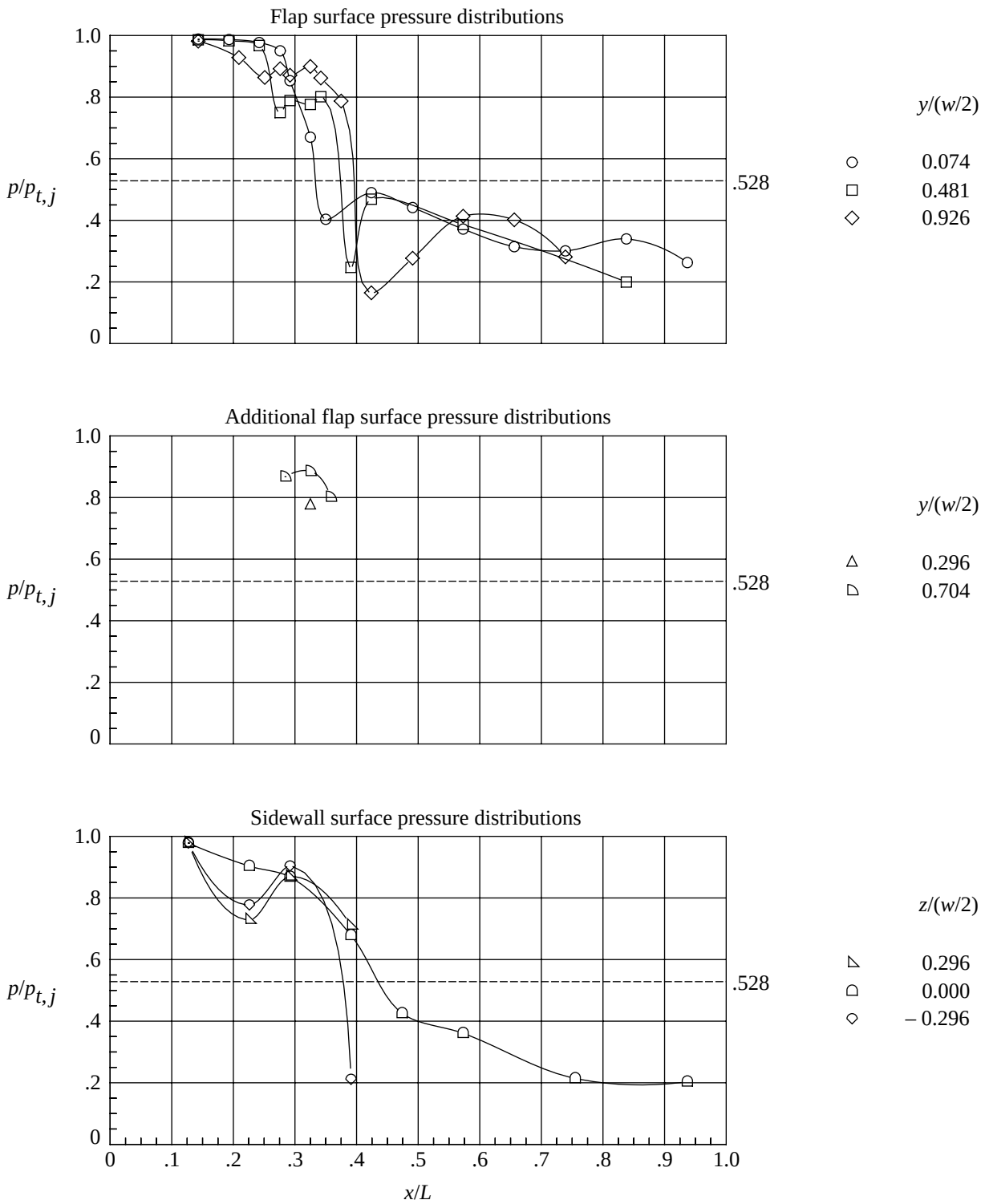

(c) $\delta_{v,y} = 20°$.

Figure 14. Concluded.

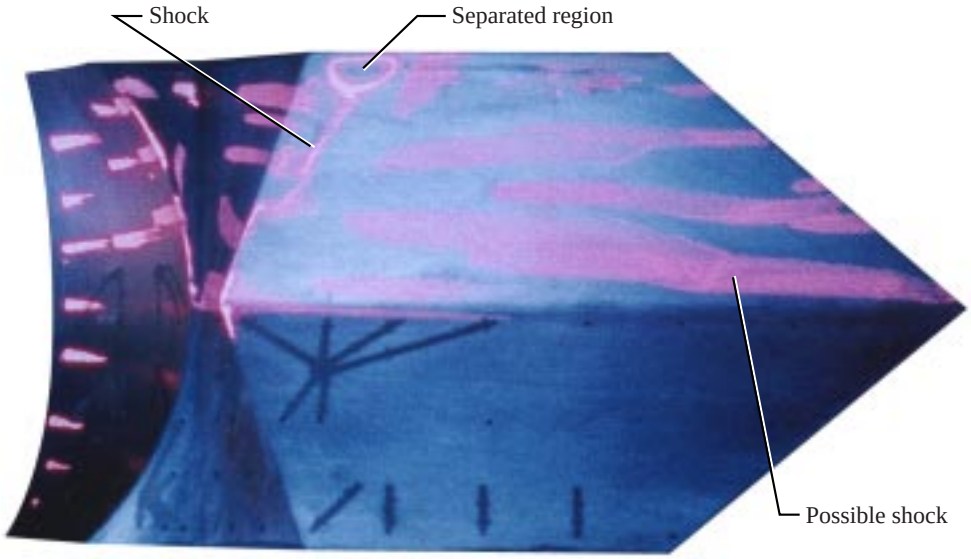

(a) Lower (suction) surface.

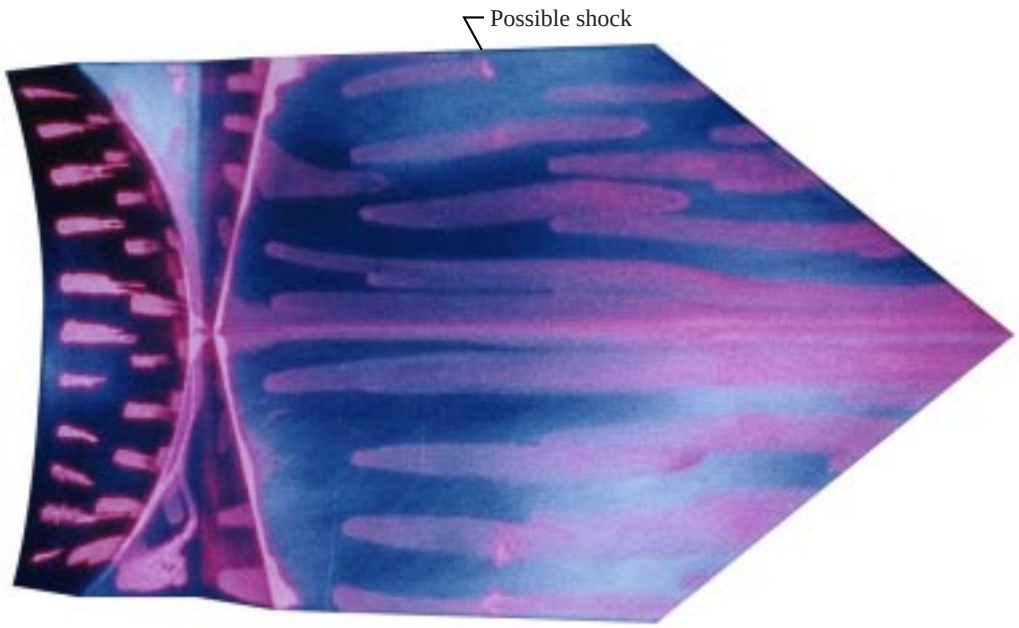

(b) Upper (pressure) surface.

Figure 15. Surface flow visualization on hexagonal nozzle at dry power, $\delta_{v,p}$ = 10°, $\delta_{v,y}$ = 0°, and NPR = 5.00.

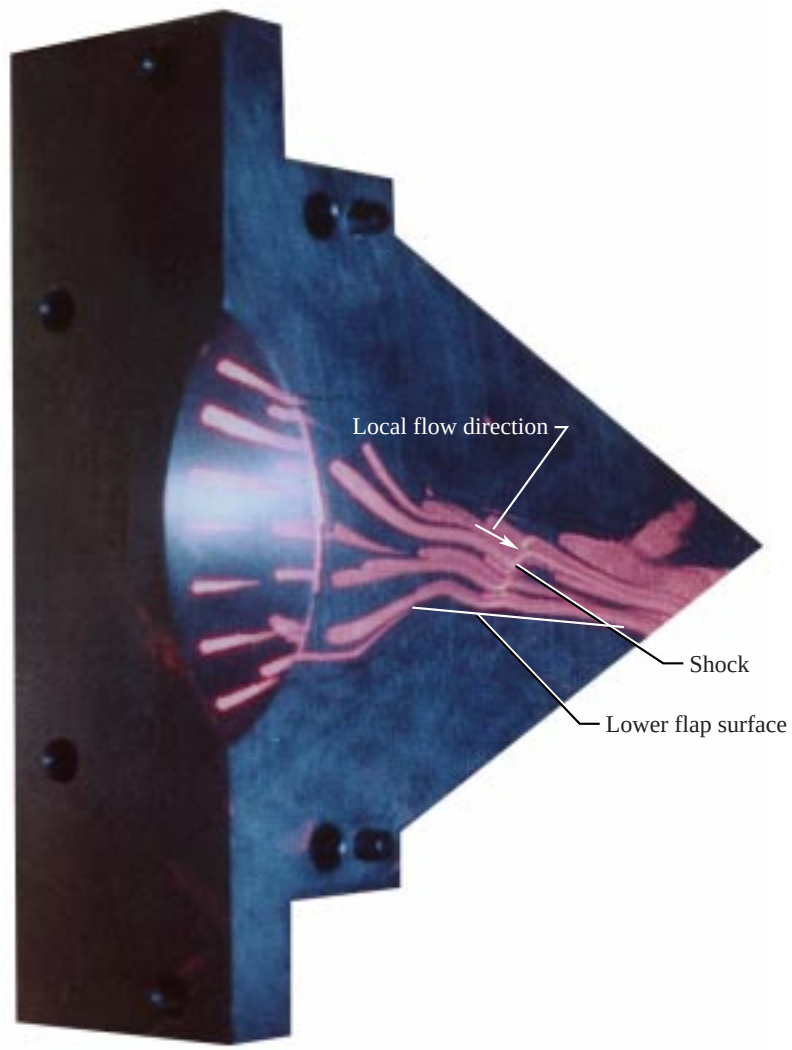

(c) Right sidewall.

Figure 15. Concluded.

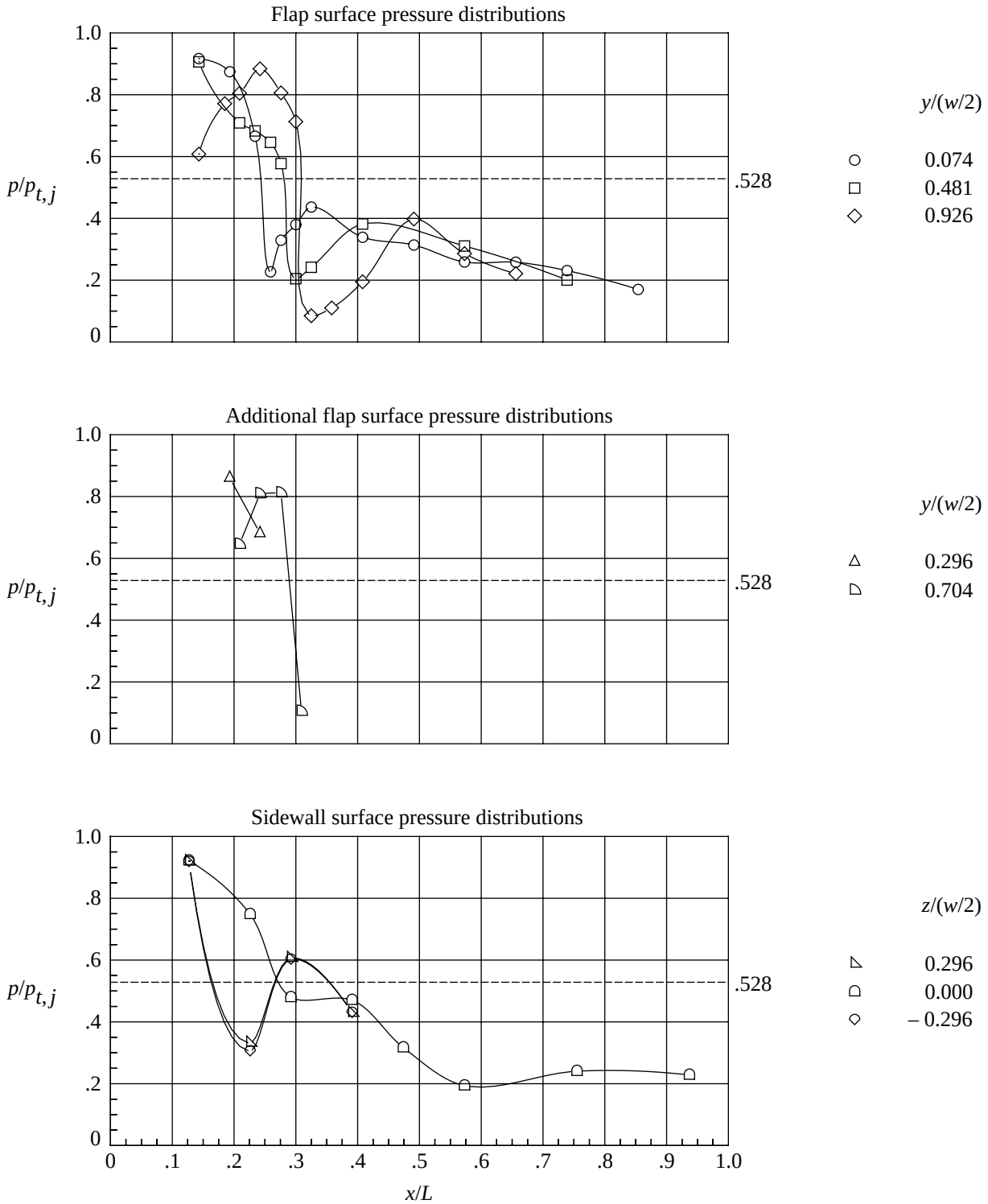

(a) $\delta_{v,y} = 0°$.

Figure 16. Internal static pressure distributions of hexagonal SCF nozzle at afterburning power, $\delta_{v,p} = 0°$, and NPR = 4.49.

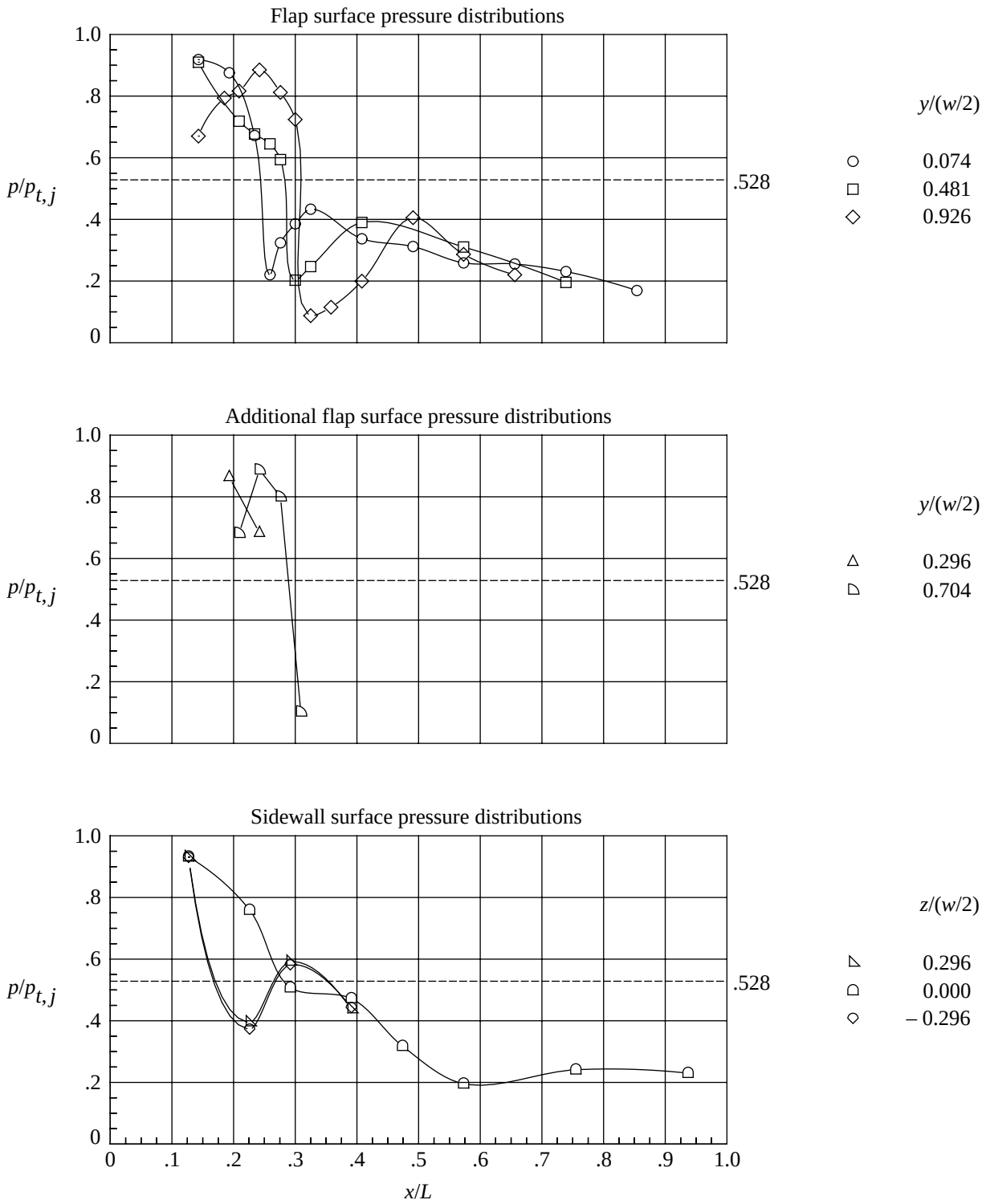

(b) $\delta_{v,y} = 10°$.

Figure 16. Continued.

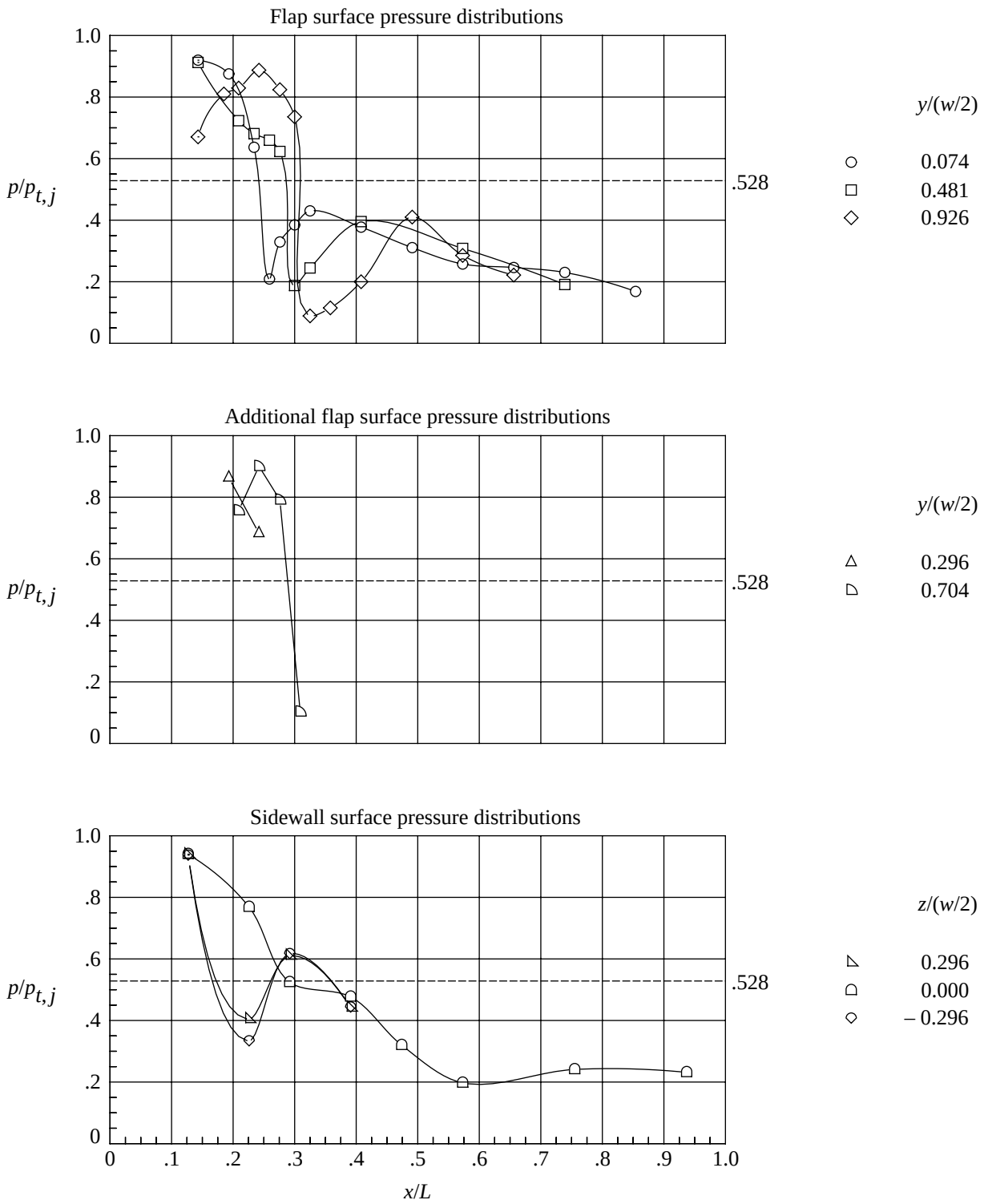

(c) $\delta_{v,y} = 20°$.

Figure 16. Concluded.

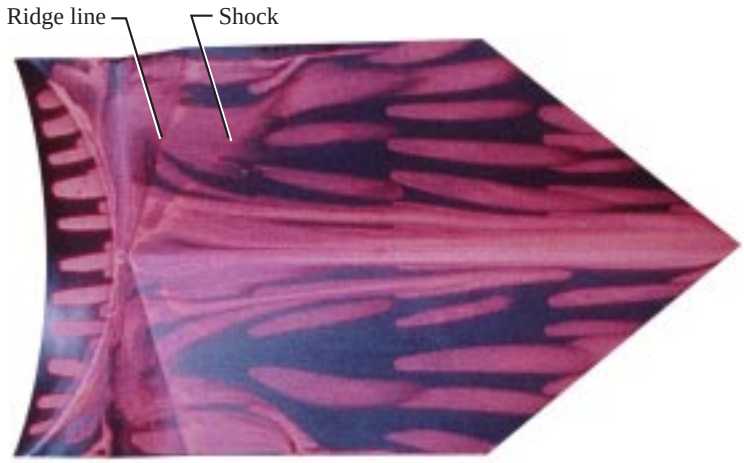

(a) Lower surface.

(b) Right sidewall.

Figure 17. Surface flow visualization on hexagonal nozzle at afterburning power, $\delta_{v,p}$ = 0°, $\delta_{v,y}$ = 0°, and NPR = 4.50.

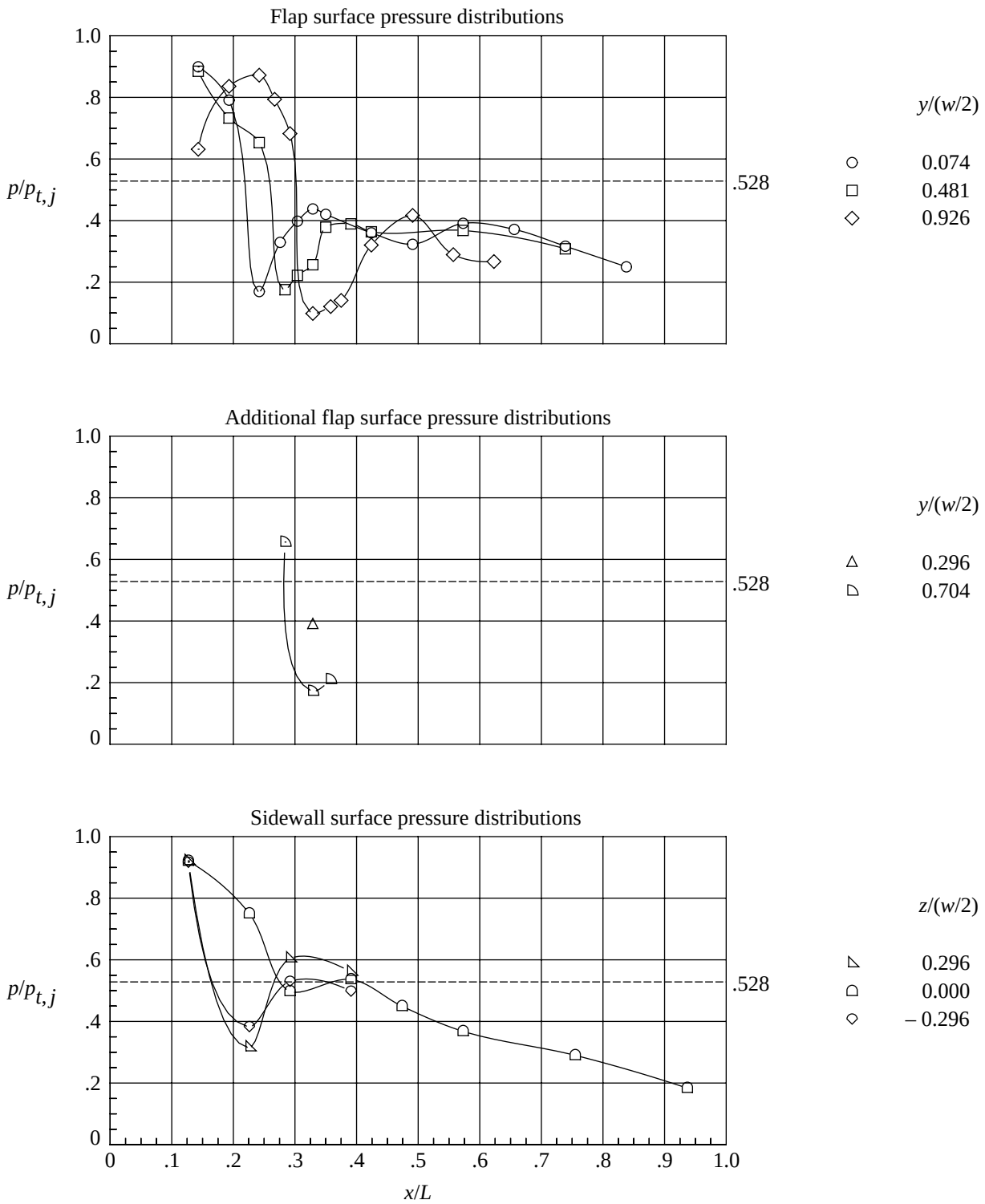

(a) $\delta_{v,y} = 0°$.

Figure 18. Internal static pressure distributions of lower (suction) flap of hexagonal SCF nozzle at afterburning power, $\delta_{v,p} = 10°$, and NPR = 5.01.

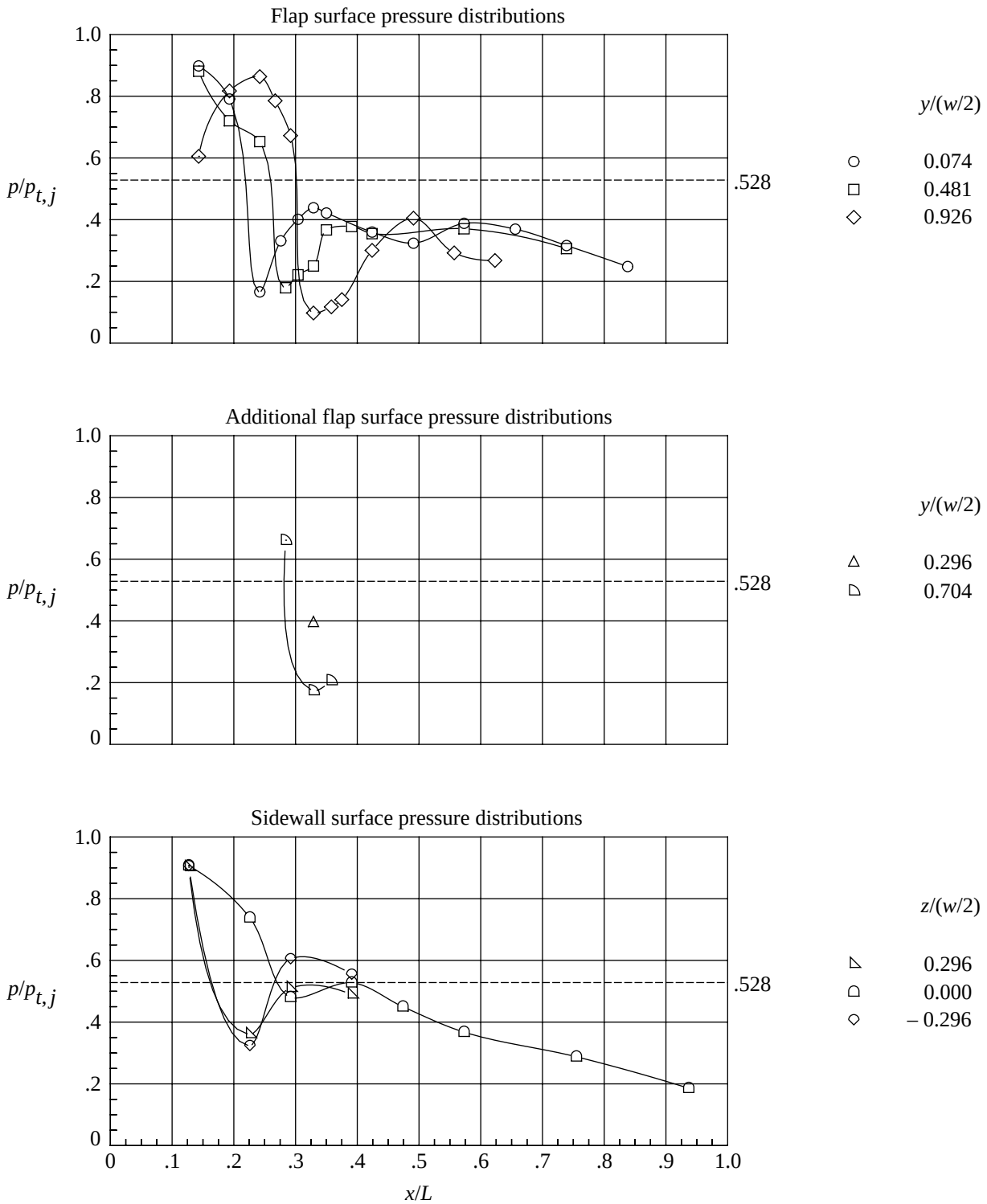

(b) $\delta_{v,y} = 10°$.

Figure 18. Continued.

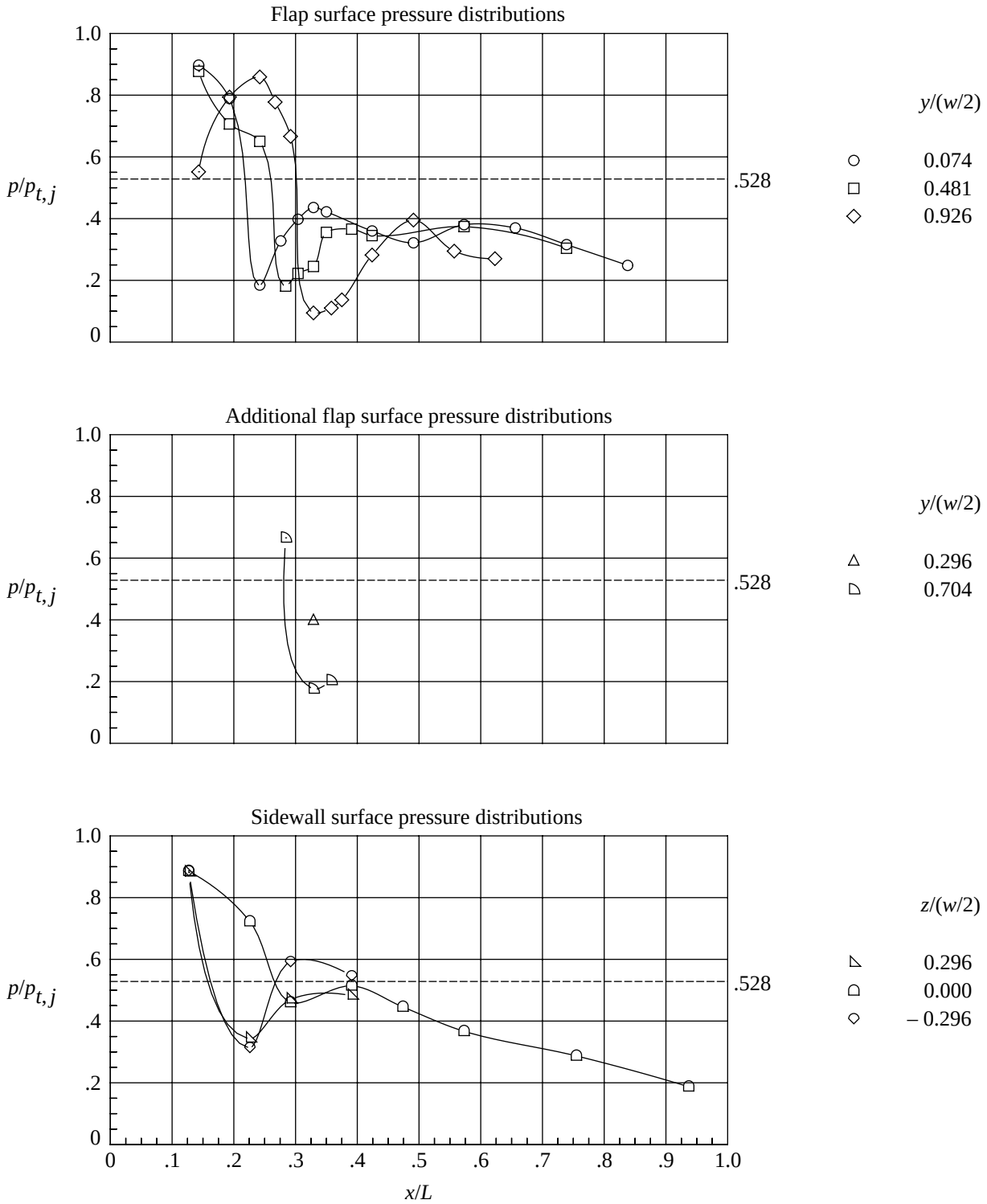

(c) $\delta_{v,y} = 20°$.

Figure 18. Concluded.

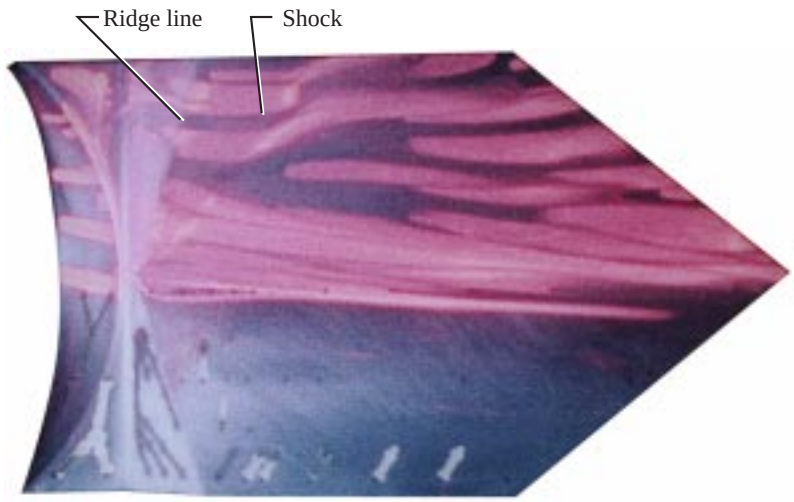

(a) Lower (suction) surface.

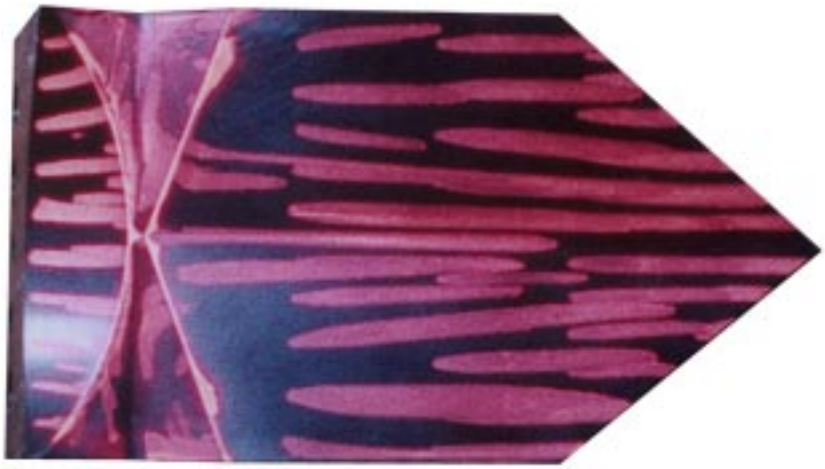

(b) Upper (pressure) surface.

Figure 19. Surface flow visualization on hexagonal nozzle at afterburning power, $\delta_{v,p}$ = 10°, $\delta_{v,y}$ = 0°, and NPR = 5.00.

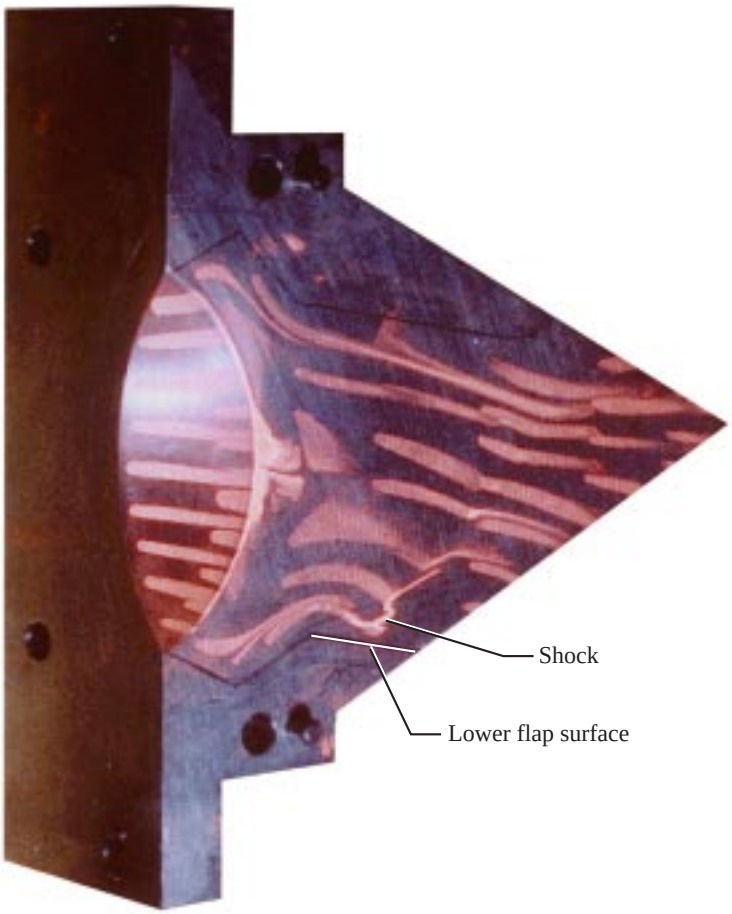

(c) Right sidewall.

Figure 19. Concluded.

REPORT DOCUMENTATION PAGE

Form Approved
OMB No. 0704-0188

1. AGENCY USE ONLY *(Leave blank)*

2. REPORT DATE
February 1998

3. REPORT TYPE AND DATES COVERED
Technical Publication

4. TITLE AND SUBTITLE
Static Thrust and Vectoring Performance of a Spherical Convergent Flap Nozzle With a Nonrectangular Divergent Duct

5. FUNDING NUMBERS
WU 522-21-11-01

6. AUTHOR(S)
David J. Wing

7. PERFORMING ORGANIZATION NAME(S) AND ADDRESS(ES)
NASA Langley Research Center
Hampton, VA 23681-2199

8. PERFORMING ORGANIZATION REPORT NUMBER
L-17635

9. SPONSORING/MONITORING AGENCY NAME(S) AND ADDRESS(ES)
National Aeronautics and Space Administration
Washington, DC 20546-0001

10. SPONSORING/MONITORING AGENCY REPORT NUMBER
NASA/TP-1998-206912

11. SUPPLEMENTARY NOTES

12a. DISTRIBUTION/AVAILABILITY STATEMENT
Unclassified–Unlimited
Subject Category 02 Distribution: Standard
Availability: NASA CASI (301) 621-0390

12b. DISTRIBUTION CODE

13. ABSTRACT *(Maximum 200 words)*
The static internal performance of a multiaxis-thrust-vectoring, spherical convergent flap (SCF) nozzle with a nonrectangular divergent duct was obtained in the model preparation area of the Langley 16-Foot Transonic Tunnel. Duct cross sections of hexagonal and bowtie shapes were tested. Additional geometric parameters included throat area (power setting), pitch flap deflection angle, and yaw gimbal angle. Nozzle pressure ratio was varied from 2 to 12 for dry power configurations and from 2 to 6 for afterburning power configurations. Approximately a 1-percent loss in thrust efficiency from SCF nozzles with a rectangular divergent duct was incurred as a result of internal oblique shocks in the flow field. The internal oblique shocks were the result of cross flow generated by the vee-shaped geometric throat. The hexagonal and bowtie nozzles had mirror-imaged flow fields and therefore similar thrust performance. Thrust vectoring was not hampered by the three-dimensional internal geometry of the nozzles. Flow visualization indicates pitch thrust-vector angles larger than 10° may be achievable with minimal adverse effect on or a possible gain in resultant thrust efficiency as compared with the performance at a pitch thrust-vector angle of 10°.

14. SUBJECT TERMS
Nozzle; Multiaxis thrust vectoring; Spherical convergent flap nozzle

15. NUMBER OF PAGES
110

16. PRICE CODE
A06

17. SECURITY CLASSIFICATION OF REPORT
Unclassified

18. SECURITY CLASSIFICATION OF THIS PAGE
Unclassified

19. SECURITY CLASSIFICATION OF ABSTRACT
Unclassified

20. LIMITATION OF ABSTRACT